"...most of the mystical outcrying which is one of the most prized and used and desired reactions of our species, is really the understanding and the attempt to say that man is related to the whole thing, related inextricably to all reality, known and unknowable. "

John Steinbeck, The Log from the Sea of Cortez

University of Alberta

Low-energy electron point source microscopy and electron holography

by

Josh Mutus

A thesis submitted to the Faculty of Graduate Studies and Research
in partial fulfillment of the requirements for the degree of

Doctor of Philosophy

Department of Physics

Spring 2012
Edmonton, Alberta

To all of my teachers;
my parents, who taught me to ask questions;
my instructors who answered some of them, but left me with more;
and to my wife Elizabeth, who has taught me the value in sharing it all.

Abstract

Low energy electron point source (LEEPS) microscopy is the simplest embodiment of an electron microscope, consisting of only a source, a sample and a detector. In a specific regime, LEEPS may also be used to create in-line holograms; special interference patterns that contain the information about the entire electron wavefront, including the structure of the sample and electromagnetic field around it. This work describes the design, construction and characterization of a microscope designed to performs LEEPS microscopy and electron holography at the nanoscale.

An overview of previous experimental apparatus are discussed. Also, the impact of spatial and energetic inhomogeneities of the electron source on the quality and resolution of the hologram, in terms of the numerical aperture of the microscope and the virtual source size of the electron emitter.

The design of the microscope itself is presented including the system for isolating the microscope from contamination, mechanical vibration and electrical noise. Using scanning tunnelling microscopy (STM) the microscope is shown to be stable within 0.1 Å. Instructions for the maintenance of the system are presented for future users of the microscope and to illustrate many of the systems described in the design of the microscope.

The source of electrons used in the LEEPS microscope is a tungsten tip sharpened so as to field-emit electrons from a single atom. The technique for crafting such tips by field-assisted etching with nitrogen is described along with a discussion of the parameters used to control the aspect-ratio of the tip.

Several samples are investigated using LEEPS: a sharp silicon nitride edge, a carbon nanotube bundle and graphene. The sample preparation techniques are discussed for each sample. Also, simple models for describing the resulting fringe patterns are proposed. There are several benefits associated with using LEEPS, including the lack of beam induced morphological changes or contamination. The samples are used to elucidate many properties about the optical system of the microscope, most importantly the expected resolution of the system.

The software designed for the microscope to acquire images with high fidelity and for post-processing and correcting data is demonstrated.

The microscope is shown to have a virtual source size of 1.6±0.6Å a figure that exceeds published results form similar instruments. Preliminary holographic reconstructions are shown. The work concludes with a discussion of the parameters to be optimized in order to reach atomic resolution.

Acknowledgements

This project has been a long road that started with an idea and an empty lab. There are many people that have helped furnish that lab with a unique experiment. Foremost, my advisor Dr. Bob Wolkow, who had the idea of taking a fresh look at electron holography, using the sources pioneered in our lab. I'd like to thank him for his insightful guidance and patient supervision over the years and for having the confidence in me to take on such a big, fun project.

I'd also like to thank Dr. Lucian Livadaru for eagerly sharing his knowledge on the theoretical underpinnings of holography and for always being willing to brainstorm new ideas. His holographic reconstruction algorithms were used in this work.

Much of the design of the vacuum system and facility for source and sample preparation and exchange is based off designs by Mark Salomons. I thank him for sharing his designs, and teaching me much of the painstaking craft associated with building the more delicate parts of this machine.

Sample preparation and characterization of samples using other microscopy techniques was done with the help of Dr. Stas Dogel. I am grateful for his help and his good humoured encouragement throughout this project.

Many thanks to the rest of the Molecular Scale Devices group, past and present. Thanks for the years of interesting and challenging discussions. I couldn't imaging a better place to do science. For that I thank: Martin Cloutier, Shoma Sinha, Jason Pitters, Radovan Urban, Cristian Vesa, Baseer Haider, Gino DiLabio, Marco Taucer, Peter Legg, Peter Ryan, Mohammed Rezeq, Paul Piva, Manuel Smeu, Bruno Martins, Mustafa Muhammad and Adam Dickie.

Table of Contents

1 Introduction **1**

1.1 History of microscopy . . . 1
1.2 Low-energy electron point source microscopy . . . 2
1.2.1 A brief introduction to electron microscopy . . . 3
1.2.2 The need for complimentary techniques . . . 4
1.3 Electron holography . . . 4
1.4 Previous experiments . . . 7
1.4.1 Coherence . . . 12
1.5 Rationale for a fresh look . . . 16
1.6 Something new . . . 17
1.6.1 Isolation . . . 17
1.6.2 Source fabrication . . . 17

2 Designing the microscope **18**

2.1 Overall design . . . 18
2.2 Ultra-high vacuum chamber . . . 20
2.2.1 The preparation chamber . . . 20
2.2.2 Handling tips and samples: UHV pliers . . . 20
2.2.3 The main chamber . . . 21
2.2.4 The scanning head . . . 22
2.3 Testing the microscope . . . 24
2.3.1 Scanning tunnelling microscopy . . . 24
2.3.2 Preparing silicon surfaces . . . 25
2.4 Mechanical isolation . . . 25
2.4.1 Transmission of mechanical noise . . . 25
2.4.2 Stages of vibration isolation . . . 28
2.4.3 First stage of isolation: active isolation legs . . . 29
2.4.4 Second stage of isolation: hanging the scanning head . . . 30
2.4.5 Working principle of the Attocube movers . . . 34
2.5 Wiring and avoiding electrical noise . . . 36
2.5.1 The scanning head wiring . . . 36

2.5.2 Crosstalk . . . 38
2.5.3 Managing miscellaneous noise . . . 40
2.6 Maintenance . . . 41
2.6.1 Maintenance of the scanning head . . . 41
2.6.2 Maintenance of the wiring . . . 44
2.6.3 Bakeout . . . 47

3 Low-energy electron point source microscopy 50
3.1 Tip preparation . . . 50
3.1.1 Field ion microscopy . . . 51
3.1.2 Electrochemical etch . . . 55
3.1.3 In-vacuum preparation . . . 56
3.2 Sample subtrate . . . 58
3.3 Acquiring images in LEEPS . . . 60
3.4 Effect of tip shape on LEEPS imaging . . . 66
3.5 Case study: LEEPS studies of an opaque edge . . . 66
3.6 Coherence properties of the beam . . . 72

4 LEEPS study of carbon nanotubes 76
4.1 Sample preparation . . . 76
4.2 Carbon nanotubes bundle as a double slit . . . 78
4.3 Carbon nanotubes as a bi-prism . . . 78
4.4 Fringe patterns . . . 81
4.5 Fitting the data . . . 84
4.6 Coherence properties of the beam . . . 87

5 LEEPS study of Graphene 91
5.1 Graphene . . . 91
5.2 Growth and transfer . . . 93
5.3 Loading and cleaning samples . . . 96
5.4 Domain structure of graphene and dark-field microscopy of graphene . . . 96
5.5 Corrugation of graphene sheets . . . 97
5.6 Interaction thickness of graphene . . . 97
5.7 Contamination of graphene sheets . . . 101
5.8 STM of suspended graphene . . . 101
5.9 Scattering off graphene edge . . . 104

6 Image acquisition and processing 109
6.1 Alignment and averaging software . . . 114
6.1.1 Block averaging . . . 117
6.1.2 Background division . . . 118

7 Conclusions and future work **119**
7.1 Exploring experimental parameters 119
7.1.1 Scanner geometry 119
7.1.2 Tip shape and emission current 123
7.2 Nanoscale samples deposited on graphene 125
7.3 Helium-ion holography 126
7.4 Outlook 127

Bibliography **129**

List of Tables

7.1 Comparing experimental results for LEEPS microscopes. 121

List of Figures

1.1 A schematic of a LEEPS experiment. 3
1.2 Excerpt from Dennis Gabor's 1949 patent describing electron holography. . 5
1.3 A schematic of the formation of a hologram. 6
1.4 Gabor's first published holograms. 8
1.5 The holography work of Michael Haine. 8
1.6 Holograms obtained in the literature. 10
1.7 Work by Stevens demonstrating the relationship between coherence angle and hologram resolution. 11
1.8 A ray diagram of a edge scattering experiment. 12
1.9 The interference pattern generated by scattering off a sharp edge by a perfectly coherent beam. 14
1.10 The interference patterns generated by the electron energy being varied by 50 meV in 1 meV steps and the total composite pattern generated. 15
1.11 The interference patterns generated by tip-sample distance being varied by 1Å in 1/10Å steps. 15
1.12 Holographic reconstruction of the point scatterer. 16

2.1 Drawings of the UHV system. 19
2.2 The UHV Pliers. 21
2.3 A cut-away view of the scanning head. 23
2.4 Scanning tunnelling microscopy. 24
2.5 A schematic of transmission of vibration from the environment to a mass m. 26
2.6 The effect on the gain of the isolation stage by varying k. 27
2.7 The effect on the gain of the isolation stage for varying ζ. 28
2.8 The effect of combining 2 stages of isolation. 29
2.9 A 1/3 octave plot of the vibration on the floor of the lab and on the STACIS supported platform 30
2.10 Suspending the scanning head from damped springs. 31
2.11 A comparison of STM imaging with the scanner suspended from TiAlV springs and from Viton cord. 32
2.12 Comparing the tunnelling current signal of the scanner hanging from the springs and from the Viton cord. 33

2.13 A diagram of the Viton cord vibration isolation and damping for the scanning head. . . . 34
2.14 The working principle of the Attocube movers. . . . 35
2.15 A diagram of the quartered electrode tube scanner. . . . 36
2.16 A complete wiring diagram of the scanning head. . . . 37
2.17 Pinout for the male end of a MIL-C 19 connector. . . . 39
2.18 The connectors fixed to the bracket at the end of the guide rod. . . . 39
2.19 The current induced in the tunnelling signal a comparison of the scanning head to the Omicron STM1. . . . 41
2.20 Removing the scanner from the spring-loaded hooks. . . . 42
2.21 The scanning head loaded into the maintenance base. . . . 43
2.22 Removing the wiring and guide from the top of the chamber. . . . 45
2.23 Repairing and adding connections to the guide rod cables. . . . 46
2.24 Reinstalling the guide rod cables. . . . 47

3.1 A schematic of the LEEPS experiment. . . . 51
3.2 Field ion microscopy. . . . 52
3.3 The FIM setup and gas manifold. . . . 53
3.4 The field-assisted etch process. . . . 54
3.5 Crafting tips with different aspect ratios by tailoring the etch process. . . . 55
3.6 A schematic of the station used for electrochemical etch. . . . 56
3.7 FIM images of a tungsten tip being etched to a single atom. . . . 58
3.8 A diagram of the construction of a SiN grid as well as and SEM image. . . . 59
3.9 The SiN window in a tantalum sample holder. . . . 60
3.10 Initial electron emission from tip. . . . 62
3.11 Increasing the magnification of the image as the tip approaches the sample. 63
3.12 The effect of emission current on imaging. . . . 64
3.13 The effect of the tip structure of the LEEPS image. . . . 65
3.14 Diffraction by an aperture in the near field (Fresnel) and far field (Fraunhofer) limits. . . . 66
3.15 Fringes seen from scattering off an opaque edge. . . . 68
3.16 Comparison of Fresnel fringes to simulation. . . . 69
3.17 Filtering and fitting fringe data 69
3.18 Scattering from an off-axis edge. . . . 71
3.19 Fitting fringes using equation 3.8. . . . 73
3.20 Fringe patterns from scattering off the edge 74

4.1 Sorting SWNTs according to their electronic characteristics. . . . 77
4.2 SEM images of bundled SWNTs. . . . 77

4.3 A simple model to describe the fringe patterns from imaging a nanotube bundle in LEEPS. 79
4.4 The working principle of an electron bi-prism along with a typical interference pattern. 80
4.5 The field around the nanotube bundle and how it can be compared to that of a bi-prism. 81
4.6 Change in interference pattern while approaching the SWNT bundle 82
4.7 Filtering the data to reveal the different sets of fringes 83
4.8 Change in interference pattern while approaching the SWNT bundle. 85
4.9 Determining the parameters of the bi-prism from fitting. 86
4.10 The relationship between beam current and D. 87
4.11 The angular width of the SWNT bundle fringe patterns. 89
4.12 FIM images of the nano-tips used in the edge and SWNT bundle experiments 90

5.1 Comparison of electrostatic potentials due to grounded nanoscale objects . 92
5.2 Transfer of graphene with and without an adhesive 94
5.3 The characterization graphene-coated perforated SiN windows. 95
5.4 LEEPS images of graphene 98
5.5 Bragg diffraction for low magnifications in LEEPS microscopy 99
5.6 Comparison of bright-field and dark-field images of the same graphene sheet 99
5.7 A further zoomed-in portion of the partially covered hole. 100
5.8 The effects of contamination on PPM of graphene 102
5.9 STEM images of graphene 103
5.10 STM images of suspended graphene 104
5.11 Graphene edge images 106
5.12 Graphene edge images continued 107
5.13 Comparison of visibility of graphene edge and carbon nanotube bundle . . . 108
5.14 Angular width of fringe pattern from scattering off graphene edge 108

6.1 A schematic of the optical system of the LEEPS microscope. 110
6.2 A screenshot of the application for controlling the camera and acquiring images. 111
6.3 The effect voltage gain on the amount of drift present in images. 112
6.4 A flowchart of the image acquisition software. 114
6.5 A comparison of the normal accumulation imaging mode and the differential mode. 115
6.6 A screenshot of the application for aligning and averaging data. 115
6.7 A flowchart of the imaging alignment and averaging software. 116
6.8 The effect of background subtraction on the image. 117

7.1 Fringe pattern presented in this work have a wider coherence angle and a greater number of overall fringes than previous work. 120

7.2 The interplay between the position of the scanning head and the width of the pattern on the detector 123
7.3 The dependence of resolution and the effect on the fringe pattern of changing tip-screen distance. 124
7.4 Effect of the shape of the apex of a tip on emission angle. 124
7.5 A preliminary holographic reconstruction of the edge. 126
7.6 A preliminary holographic reconstruction of defects in a graphene sheet. . . 127

Chapter 1

Introduction

1.1 History of microscopy

The story of modern microscopy arguably starts with Antonie van Leeuwenhoek. van Leeuwenhoek was not a scientist, in fact he was a draper by trade. Although he lived in Delft, Holland until his death in 1723, he was known throughout the scientific world through his reports to the Royal Society. Practically speaking, van Leeuwenhoek's contribution to modern microscopy, and his advantage over his peers, was his ability to make very small spheres of glass. He did so by heating a thin rod of glass and pulling it into a fine whisker, then carefully inserting the whisker into a flame. The glass fibre would melt and contract into a nearly perfect sphere which made a terrific lens: the smaller the sphere, the higher the magnification of the lens.

Holland was at the forefront of optics at the time, the compound microscope was invented there, some 30 years before van Leeuwenhoek was even born. Despite the fact that some of the finest ground glass lenses in the world were crafted in Holland, van Leeuwenhoek used his tiny glass spheres [1]. His microscopes were remarkably simple, consisting of a single spherical lens fixed to a specimen on a copper or silver frame. The specimen was brought into focus by adjusting the position of the lens relative to the specimen using a fine screw. To use the microscope it had to be brought incredibly close to the eye of the user, and the images had to be painstakingly recorded by pen on paper.

The microscope was able to attain surprisingly high magnifications; surviving microscopes provide magnification levels of up to 275 times [1]. It is thought that van Leeuwenhoek made microscopes capable of nearly 500x magnifications. van Leeuwenhoek's microscope had three huge advantages over the tools of his contemporaries: it was simple and had high magnification, with low aberrations. The simplicity of the microscope is obvious, it consisted of only the lens and the sample. The entire microscope could easily fit into the palm of your hand. Its simplicity allowed van Leeuwenhoek to make hundreds of microscopes, tailor-made for each of his samples. Due to its small size, the microscope was also very mechanically stable, and immune to vibration and noise. Lastly, because van Leeuwenhoek's lenses relied on an elegant self-limiting process (essentially, surface tension) they were

virtually free of aberration. In contrast, the compound microscopes of the day relied on imperfect lenses, with relatively low magnifications. To achieve higher magnifications, lenses has to be combined, exacerbating those aberrations.

Among other things, van Leeuwenhoek's simple microscopes recorded the first observations of single celled organisms. His observations challenged the very definition of life and make up the foundation of modern microbiology. They shifted and deepened our understanding of everything from disease to the nature of humanity. Before van Leeuwenhoek, a droplet of water from a pond was an inert object, but van Leeuwenhoek showed us it was a zoo, teeming with micro-organisms. van Leeuwenhoek taught us that we ourselves are a zoo made of up of millions of cells [1]. Since then, led originally by craftsmen and artisans like van Leeuwenhoek, the field of microscopy has pushed the limits of resolution and expanded the horizons of our understanding.

More recently, microscopy has been pushed to the atomic scale allowing researchers to see such wonders as the electronic orbitals in a single molecule, confirming structure that had been predicted decades before ever being visualized [2]. However, there is no one perfect microscope, and still today many basic samples lack structural definition. Moreover, different imaging modalities are always needed to gain insights about the structure and function of different samples. New microscopes are always needed in hopes of further expanding those horizons.

1.2 Low-energy electron point source microscopy

Low-energy electron point source (LEEPS) microscopy (illustrated schematically in Figure 1.1) is the simplest implementation of electron microscopy (EM), and consists of only an electron source, a conductive sample and a detector. The electron source, typically a sharp metal tip, is brought incredibly close to the sample, and a bias is placed between source and sample. The bias induces field emission from the tip and electrons are accelerated through the sample towards the detector, some centimetres away. In this technique the sample serves also as anode. An image of the sample is projected on the detector, magnified by the ratio:

$$M = \frac{D}{d}, \tag{1.1}$$

where D is the distance between the tip and the detector and d is the distance between the tip and the sample.

To achieve large magnifications above 10^6, for a detector centimetres away, the tip must be fewer than a hundred nanometres from the sample. Because of these minute separations, and for a sufficiently sharp tip, only modest voltages are required for field emission. Electrons are typically accelerated to energies less than 200 eV. These energies are many orders of magnitude lower than those used in typical high-resolution EM techniques. This is one of many benefits of LEEPS, since the samples that can be studied using conventional

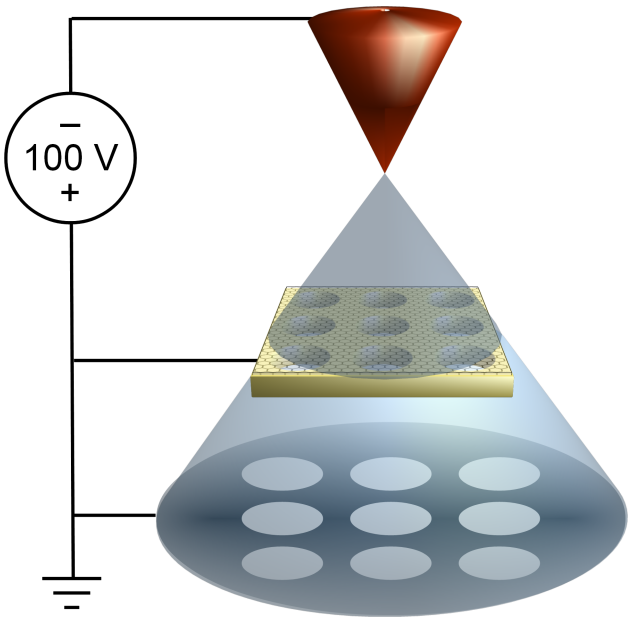

Figure 1.1: A schematic of a LEEPS experiment, reproduced with permission from [3]. In this experiment, a biased metal tip is brought near a grounded sample. Electrons are field-emitted through the sample. The result is a magnified image on the distant screen.

techniques must be sufficiently robust to withstand electrons with energies in excess of 80 keV. This means that LEEPS may be used to image many biologically relevant molecules that are too fragile for use in standard techniques.

1.2.1 A brief introduction to electron microscopy

From van Leeuwenhoek on, scientists pursued higher and higher resolution, soon butting up against the diffraction limit; the inability to craft conventional lenses that focus light to a point smaller than half the wavelength of that light, or resolve a point smaller than that size. In order to circumvent that limit, microscopists turned to electrons, which have a characteristic wavelength orders of magnitude shorter than visible light.

An early practitioner, Dennis Gabor, considered using electrons to probe nature at the finest scale, but quickly dismissed the idea because he thought "Everything under electron beam would burn to a cinder " [1]. However, the idea was pursued in the 1930s by German scientists Knoll and Ruska. Electrons were relatively easy to produce at the time, and sources were readily available in the form of cathode ray tubes. What was needed were lenses of sufficient quality to build a suitable microscope. The problem shifted then to the problem faced by van Leeuwenhoek and his peers: how to make good enough lenses. In 1931, Knoll and Ruska reported experiments on magnetic lenses, and a 2 lens microscope was demonstrated later in the same year [1].

From then on, electron microscopes have evolved along two paths, the transmission electron microscope (TEM) and the scanning electron microscope (SEM). The principle

components of both machines are the same. As an electron source, a metal filament is heated to high temperature in order to emit a shower of electrons. The beam of electrons is narrowed to a fine beam using an aperture. This beam is then accelerated to high energies using a series of plates. The accelerated beam is conditioned using a series of electromagnetic lenses before being focused into a tight point at the sample. In TEM, the focused beam is incident on a sample and is projected through the sample towards a detector. The result is a magnified image of the sample on the detector. In SEM, the focused beam is rastered across the sample, ejecting secondary electrons from the sample. These secondary electrons are collected and an image is produced of a map of secondary electron yield as a function of position of the electron beam on the sample. Both these techniques can be used to visualize samples at the nanoscale, but neither technique is perfect.

It is incredibly difficult to create an electromagnetic lens of comparable quality to the finest optical lens. The resulting aberrations limit the resolution of the instruments. Were the resolution dictated by the energy of the electrons, a TEM would be capable of resolving features well below an Angstrom.

The remaining challenges are sample specific, due to the high-energy electrons involved, there is significant potential to induce morphological changes [4]. Because of this potential, imaging of soft matter, viruses or proteins, is limited to sophisticated techniques that involve taking many short exposures of identical samples in many orientations and using that immense dataset and computational techniques to resolve a structure [5].

1.2.2 The need for complimentary techniques

Despite the vast array of microscopy tools developed in the intervening centuries, there is no one general purpose microscopy technique for ascertaining structure at the nanoscale, and below. Unfortunately, there are relatively few tools for ascertaining the three-dimensional (3D) structure of nanoscale objects. For samples that can be crystallized into periodic arrays, the structure of that array can be determined with great accuracy, using X-ray diffraction. But, for samples that exist as discrete entities, and whose function is dependent on their discrete nature (nano-particles or viruses), there very few ways to directly ascertain their structure in three dimensions. Although there are many tricks to use TEM [5] or X-Ray scattering [6] to gain 3D information, most of those techniques involve some sort of iterative computation that requires some initial assumption about the nature of the sample.

1.3 Electron holography

In 1948, Dennis Gabor, having already conceived of, and having prematurely dismissed the electron microscope, tried again to make an impact on this nascent field. By this time, electron microscopy was an established tool, but one with many difficulties. The chief difficulty was the lack of quality electron lenses. Inspired while waiting for a tennis court in 1947 Gabor asked himself a question:

> When we take a photograph, the image appears in the plane of the plate. But by Huygens' Principle the information which goes into the image must be there in **every** plane before the plate, also in the plane before the lens. How can it be there in that uniform whiteness? Why can we not extract it? ...could we not do it at least with monochromatic light [7]?

In essence, Gabor was wondering: could microscopy be done without lenses? All the information about the structure of the sample is present in the wavefront, so how could that information be retrieved without resorting to lenses that distort the image of the sample?

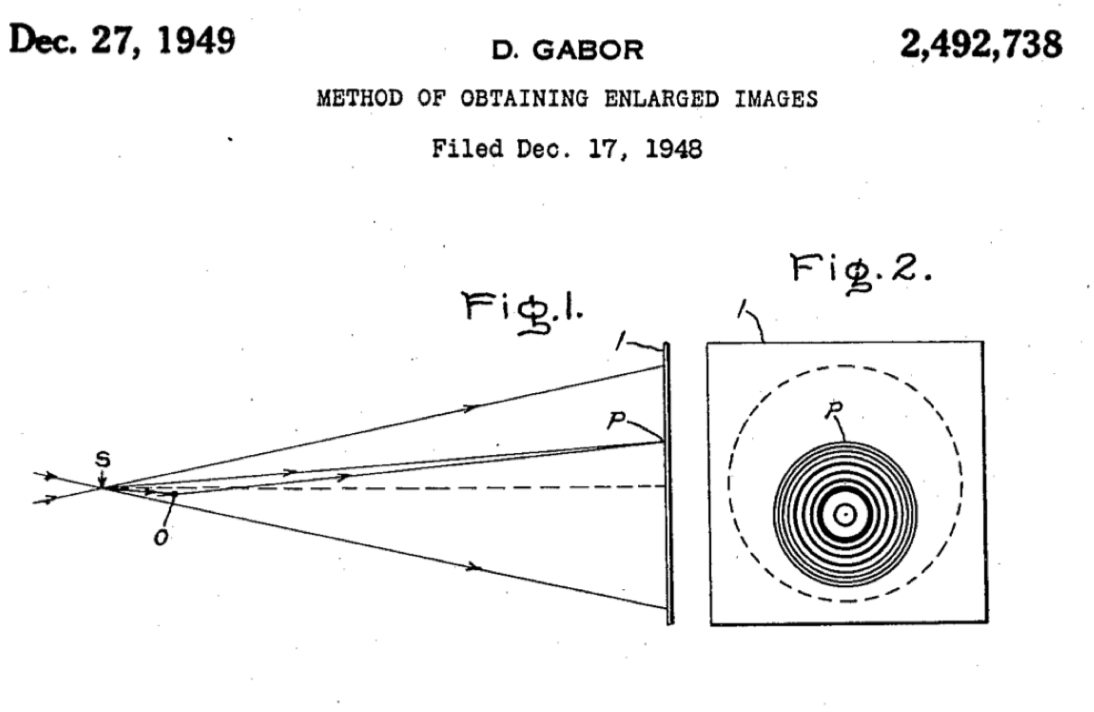

Figure 1.2: Excerpt from Dennis Gabor's 1949 patent describing electron holography.

What Gabor proposed [8] was a scheme for recording the an image of the wavefront in every plane between the source and the detector. His original patent for the proposal is shown in Figure 1.2. He called the image a hologram, a word derived from Greek to mean 'whole picture.' The hologram is in essence a special type of interference pattern. In the original scheme proposed by Gabor, a coherent source of electrons emits radiation through a sample towards a position sensitive detector, some distance away. In this in-line technique, the source, sample and detector share the same optical axis. An interference pattern, or hologram, is generated at the detector because part of the coherent wave emitted from the source passes by the sample without scattering; this is called the reference wave Ψ_r. Another portion of the wave is scattered off the sample; this is called the scattered wave Ψ_s. As shown in Figure 1.3, these two partial waves interfere at the detector producing a fringe pattern. Contained in this pattern is a map of the entire wavefront from source to

detector. Mathematically, the intensity of the pattern in the plane of the detector is:

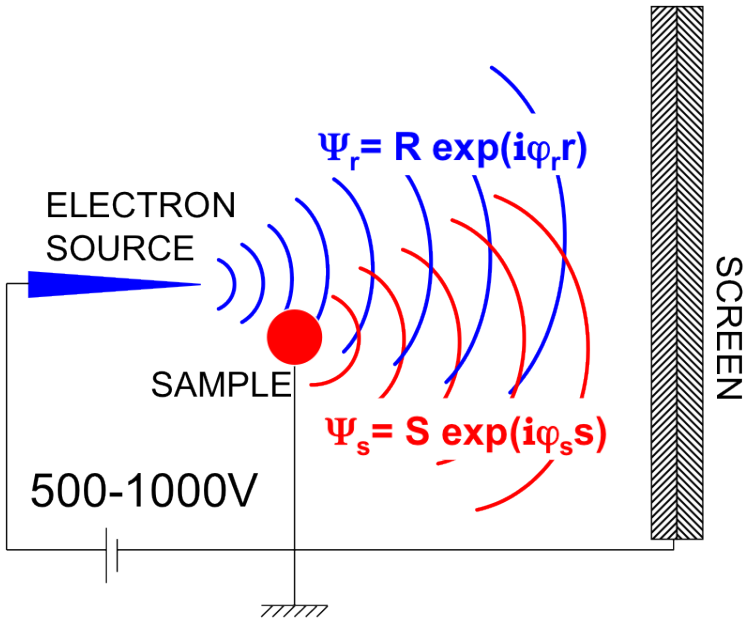

Figure 1.3: A schematic of the formation of a hologram. The reference wave (in blue) and scattered wave (in red) interfere at the detector to produce a hologram.

$$I_{holo}(x,y) = R^2 + S^2 + 2RS\cos((\phi_r - \phi_s)r), \tag{1.2}$$

where ϕ_r and ϕ_s are the phase factors of the reference and scattered waves and R and S are their amplitudes.

Holography is a two step process, and in order to retrieve meaningful structure of the sample, the hologram has to be reconstructed. Optically, this is possible by illuminating the hologram with the same wavefront used to generate the hologram. If the hologram were recorded on a transparent photographic plate, and the same beam of light used to generate the hologram illuminates that photographic plate; the manner in which the light interacts with the hologram produces the same wavefront to emanate from the plate as would emanate from the original sample. The observer would perceive a virtual image of the sample inside the photographic plate, whose orientation would shift with the observer.

The same reconstruction process can be accomplished digitally, if the reference wave is sufficiently well known. An image of the sample can be reconstructed in any plane along the optical axis resulting in a truly three-dimensional tomographic image of the sample. To glean structural information from the hologram, the first two terms must be removed. The R^2 term is simply the background - the signal from the electron beam without the sample in-between. This part can be easily subtracted from the hologram. In the appropriate regime, S^2 will be small and can be neglected. It is important that only samples that are small and only scatter a small portion of the beam can be studied, in order to ensure

interference patterns in this holographic regime. The remainign term in equation 1.2 is called the contrast hologram and is used as the input for our reconstruction algorithms [9, 10, 11].

Despite being proposed in 1948, the technique of electron holography has yet to live up to its promise. Ironically, the incremental evolution of electron lenses has far outstripped the revolutionary promise of electron holography. Today, with the advent of aberration correction in TEM, truly amazing images with atomic resolution and elemental contrast are available in the best labs around the world.

1.4 Previous experiments

Almost immediately after proposing the idea of holography, Gabor demonstrated it experimentally. To simplify the experiment, he conducted a proof-of-principle using coherent visible light instead of electrons. As his sample, he used a mask with the names "Huygens, Young and Fresnel" inscribed upon it. He illuminated the sample with the only source of coherent radiation available at the time: a gas discharge lamp - specifically a single emission line of mercury. The resulting interference patterns were recorded on a photographic plate which was then reconstructed by illuminating it with the same frequency of light used to create the pattern. The reconstruction could be projected onto an arbitrary medium and recorded. The results of these initial experiments are shown in Figure 1.4.

Although promising, these initial results were difficult experiments. The only coherent light sources available were dim, and holograms took a long time to record. As a result the photographic emulsions had to be particularly sensitive and exposure times had to be long - any instability would ruin the hologram. Moreover, any defect in the optical system would appear in the hologram: microscopic air bubbles in the lenses would appear as ripples in the hologram and were impossible to remove.

Inspired by Gabor's work, several groups around the world attempted electron holography. The group of Michael Haine [12] managed to produce insightful holograms, reconstructed to obtain a resolution of a few nanometers. These results are shown in Figure 1.5. Again, this was a two step process; the hologram was recorded using electrons, and the reconstruction was carried out using optical means. To perform the reconstruction, the hologram was illuminated with visible light, again a spectral line in an arc-discharge lamp.

That said, efforts were hamstrung by the lack of coherent electron sources for generating holograms, and by the lack of bright, coherent light sources for reconstructing the holograms. Unfortunately, enthusiasm faded in the late 1950s and pursuit of electron holography went dormant for a few decades [7].

The early 1960s heralded the invention of the laser, a bright, highly coherent source of light. Using the laser, Emmet Leith and Juris Upatneiks, produced the first three-dimensional optical holograms. This drove a great deal of enthusiasm and investment into the field and the term hologram was vaulted into popular culture.

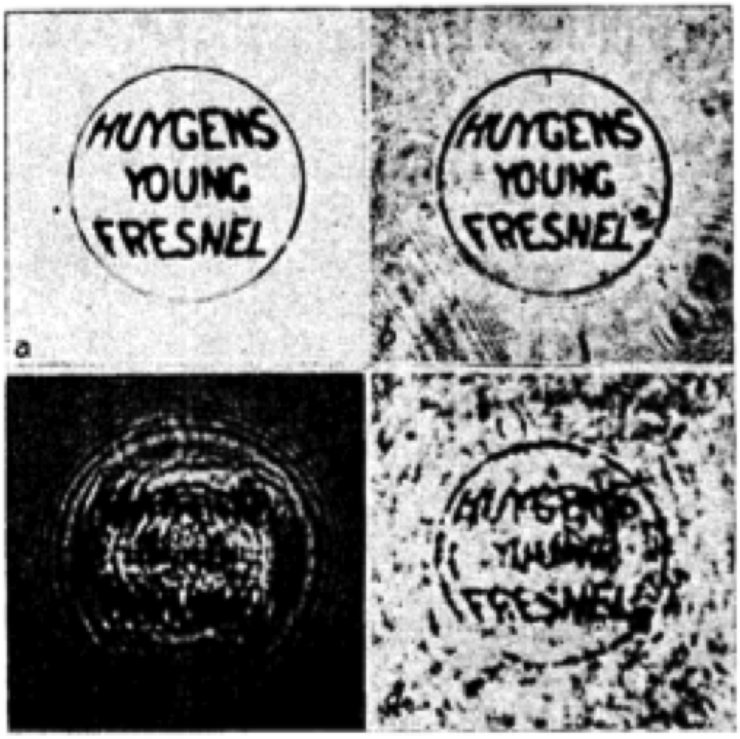

Figure 1.4: Gabor's first published holograms reproduced with permission from [8]. These holograms were formed by illuminating the transparent mask shown in (a) with a spectral line from an arc-discharge lamp. The resulting hologram in (c) was optically reconstructed in (d).

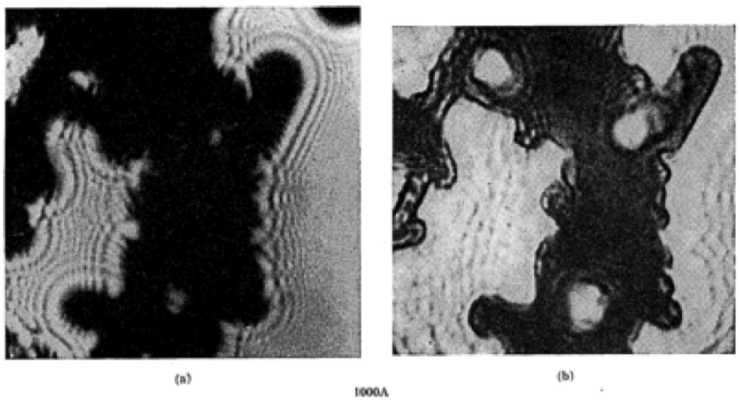

Figure 1.5: The holography work of Michael Haine, reproduced with permission from [12]. A hologram of a zinc oxide particle (a) along with an optical reconstruction (b).

Inspired by this enthusiasm, computer generated holograms, or digital holography, was pursued. First pursued at IBM in the early 1960s, proof-of-principle digital holograms were generated, printed on transparency and reconstructed using optical means. Work continued over the subsequent decades on the generation of digital holograms, and on the digital reconstruction of holograms, at IBM and increasingly in the Soviet Union [7].

The imagination of the public was captured by the promise of three dimensional movies and recordings, which unfortunately failed to materialize. Once again, interest in holography faded [7].

The main reasons early efforts in electron holography failed were (*i*) the lack of coherent electron sources for creating the holograms, and (*ii*) the lack of sufficiently stable systems for reconstruction. As computers grew more and more complex and powerful, the prospect of reconstruction using digital holography became feasible [7]. In 1986, at IBM in Zurich, H.W. Fink crafted the first single-atom electron source. Because of increased spatial coherence of the source, interest returned to electron holography. Several groups designed microscopes over the next few decades to pursue electron holography. The development of the microscopes evolved hand in hand with the development and refinement of the electron sources and the understanding of their coherence properties.

A summary of results in electron holography is presented in Figure 1.6. Despite advances in the electron sources, electron holograms have failed to provide insight beyond traditional EM techniques. But why?

The precise reason why experiments in electron holography have struggled to reach resolutions less than 10 Åwas well illustrated by Stevens in 2009 [15]: the divergence of electron sources is too narrow to obtain higher resolution images. Stevens simulated holograms of a segment of DNA by using electron beams with different divergences. What he noticed was that sub-nanometer resolution images could only be obtained for beams with large divergences. Moreover, the holograms obtained using beams with divergences typically measured in the literature resulted in holograms with a resolution of 1-2 nm, and were qualitatively similar to contemporary electron holograms. These results are shown in Figure 1.7.

The work by Stevens illustrates the concept of numerical aperture (NA): the wider the divergence angle, α, of the beam, the higher resolution image can be obtained:

$$NA = \sin\alpha. \tag{1.3}$$

It is well known that the limit for the smallest feature resolved by a given optical system, R, is related to its numerical aperture by:

$$R \geq \frac{\lambda}{2\mathrm{NA}} = \frac{\lambda}{2\sin\alpha}. \tag{1.4}$$

In fact, this very resolution limit is discussed in Gabor's 1948 paper [8]. In other words, it is not enough to have a coherent source that emits electrons from a single atom. That source must generate a beam wide enough to create a pattern on the detector with enough

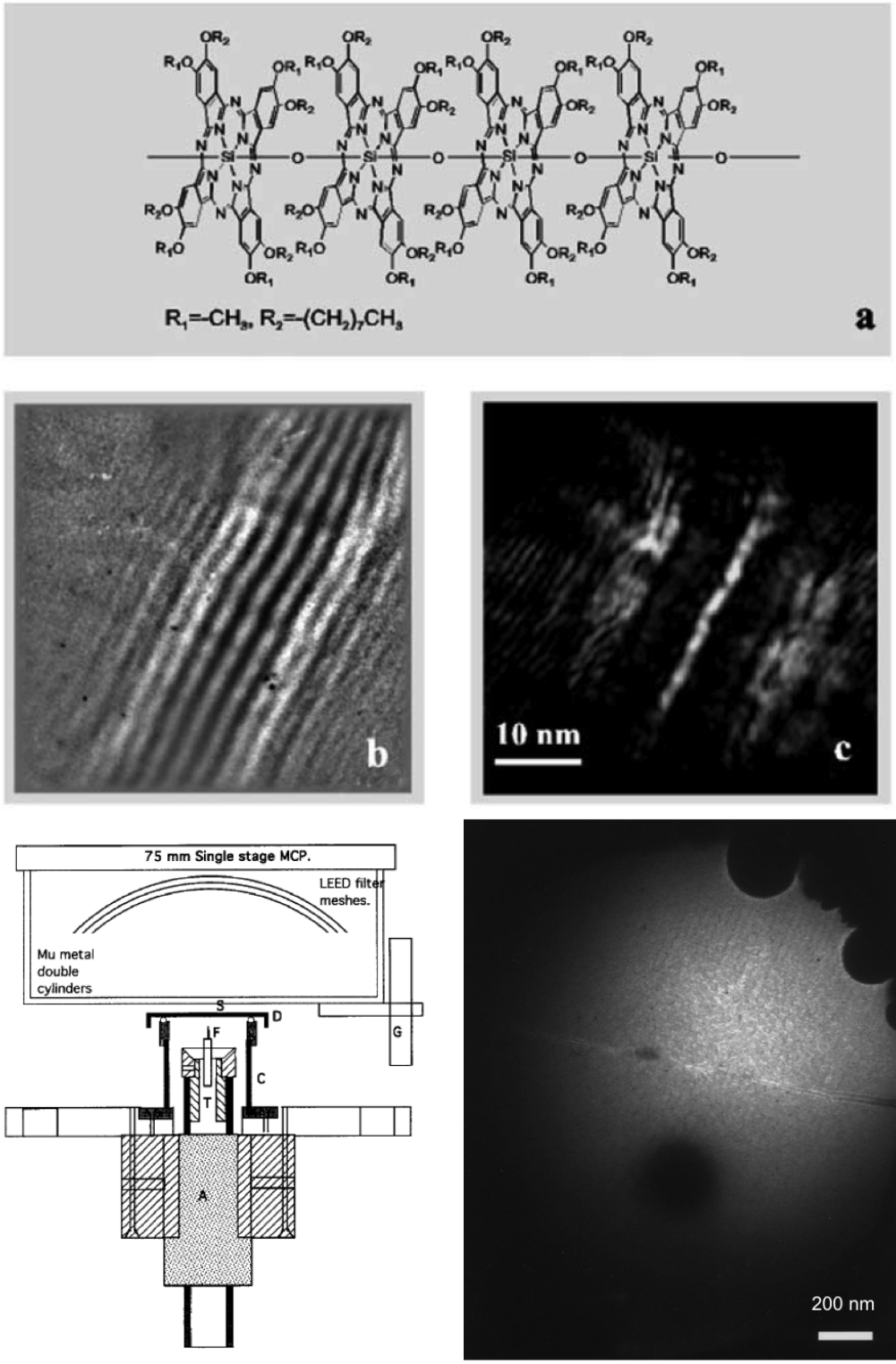

Figure 1.6: Hologram (b) and reconstruction (c) of a large molecule shown in (a) reproduced with permission from [13]. Rough structural trends are present in the reconstruction. Apparatus from the group of JCH Spence et al (bottom left), and an image of a tobacco mosaic virus suspended across a pore (bottom right). Reproduced with permission from [14].

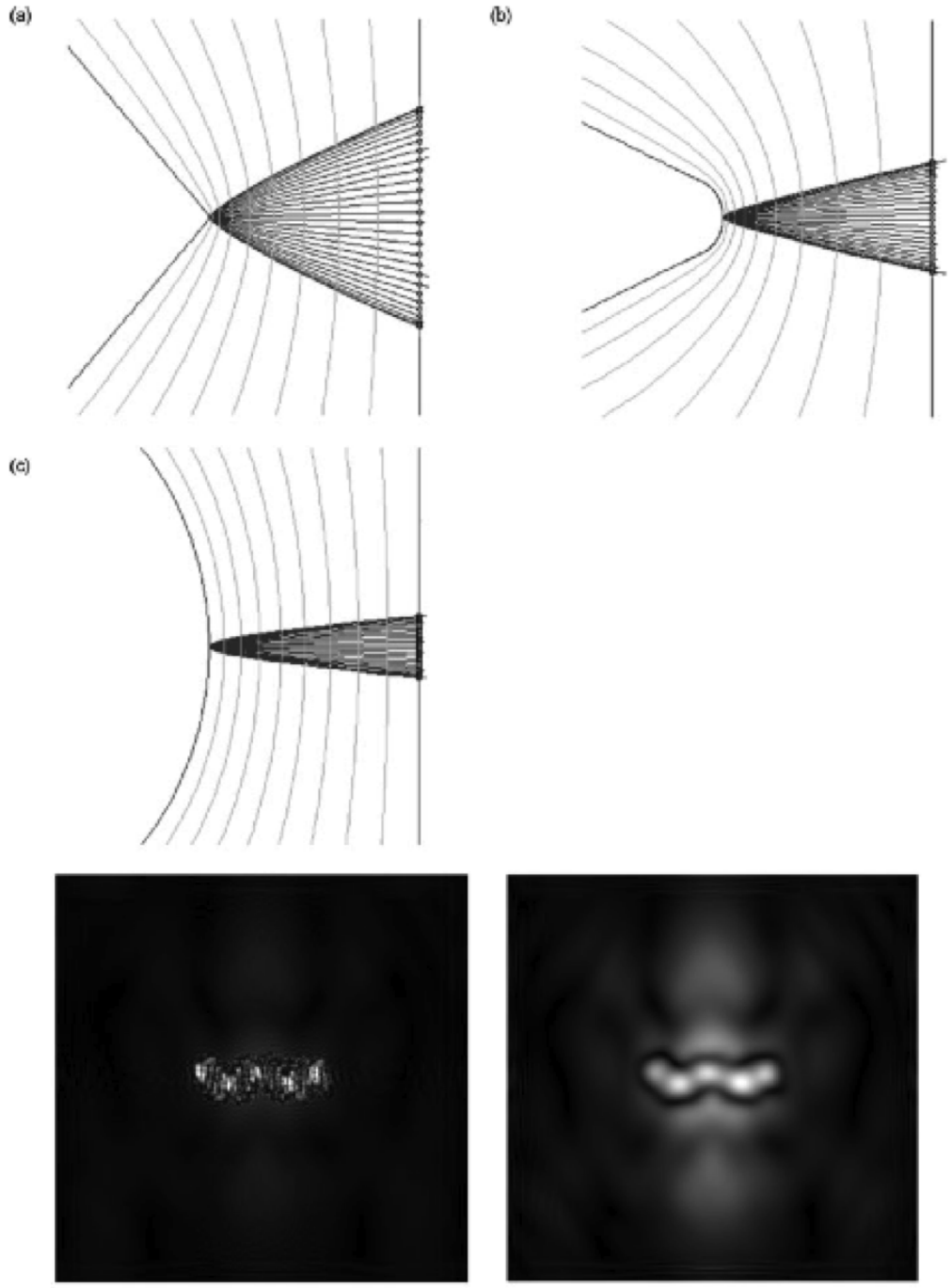

Figure 1.7: Work by Stevens [15]. Top three frames show the effect of tip shape on the emission angle of an electron beam. Bottom two frames show the effect of the emission angle of the resolution of the reconstructed hologram. Left is for a beam with a 45° divergence angle, right is for a beam with a 2.1° divergence angle. The narrower beam results in a holographic reconstruction with far lower resolution. The result is qualitatively similar to the work by Golzhauser shown in Figure 1.6

information to obtain a high-resolution image. In essence, a narrow pattern does not contain enough fringes to generate an image with sufficient detail.

1.4.1 Coherence

The coherence of the source is critical to holography. Without a coherent source, the interference pattern would be completely washed out. The manufacture of electron sources that emit from a singe-atom will be described in Chapter 3. As previously mentioned, it is not enough to have a single-atom emitter, but an emitter with a broad beam divergence. The impact of the shape of the apex of the tip on the emission angle will be discussed as well as techniques to craft such an electron emitter.

To best understand the impact of coherence on the resolution of the experiment it is useful to examine a simple experiment: scattering the electron beam off a sharp edge [16]. In this experiment, the tip is a distance d from a sharp edge. A bias is applied between the edge and the tip, causing electrons to be field-emitted from the tip. The edge itself acts as a point scatterer, and can be treated as another point source of electrons. The geometry of this experiment is shown in Figure 1.8.

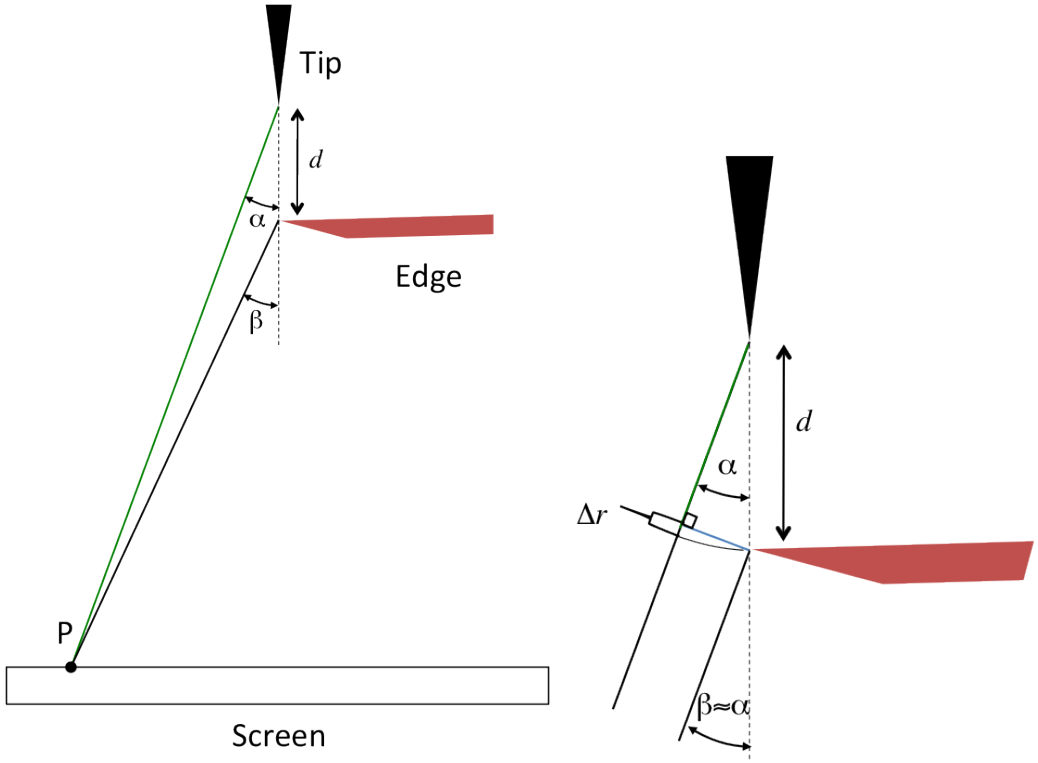

Figure 1.8: A ray diagram of a edge scattering experiment. In the far field approximation, the phase difference between the two beams can be expressed as $\Delta r = d/2\alpha^2$

At the screen, the wave originating at the tip, and the other from the edge will interfere. The probability of detecting an electron at a point P on the screen is:

$$
\begin{aligned}
\Psi_{tot}(\mathrm{P}) &= \Psi_{tip}(\mathrm{P}) + \Psi_{edge}(\mathrm{P}) \\
&= A\exp\left(i(kr_1 - wt)\right) + A\exp\left(i(kr_2 - wt)\right) \\
&= A\exp\left(i(kr_1 - wt)\right)(1 + \exp\left(ik\Delta r\right)) \\
&= A\exp\left(i(kr_1 - wt)\right)\exp\left(ik\Delta r/2\right)(\exp\left(-ik\Delta r/2\right) + \exp\left(-ik\Delta r/2\right) \\
&= A\exp\left(i(kr_1 - wt)\right)\exp\left(ik\Delta r/2\right)2\cos(k\Delta r/2) \qquad (1.5)
\end{aligned}
$$

where $r_1 = |\vec{r_1}|, r_2 = |\vec{r_2}|$, $\Delta r = r_2 - r_1$ and $k = 2\pi/\lambda$. From the geometry of the experiment [16] and for small angles:

$$\Delta r = \frac{d}{2}\alpha^2, \qquad (1.6)$$

when the distance from the tip to the detector is large compared to d.

Finally, the angular distribution of the intensity of the pattern is:

$$I(\alpha) = |\Psi_{tot}|^2 = I_o\cos^2(k\Delta r/2) = I_o\cos^2\left(\frac{\pi d\alpha^2}{2\lambda}\right) \qquad (1.7)$$

It is worth mentioning that equation 1.7 is similar to the result for the angular intensity due to the interference from a double slit. This is unsurprising, since the geometry is nearly the same: two coherent sources interfering at a detector. The main difference is that the centre of the optical axis is along a straight line between source and edge, instead of equidistant between the two slits. Consequently, the pattern depends on α^2 instead of α.

Now that we have the expression for the interference pattern from an edge scattering experiment, we can examine the effect of the coherence properties of the source on that pattern, and ultimately on the resolution of the instrument. For a pattern generated by a totally coherent beam (as shown in Figure 1.9), the fringes extend to arbitrarily wide angles - beyond where the small angle approximation is valid. Remember that the resolution of the instrument is related to the width of that pattern according the equation 1.4. Therefore, the wider the divergence of the beam, the higher the resolution.

For a perfectly coherent beam, the fringe pattern due to the scattering off the edge would extend over the full visible width of the beam. However, there are two parameters that effect the frequency pattern, d and λ, and the variability in those parameters will affect the width of the pattern.

In this experiment, the wavelength of the incident electrons is controlled by the bias between the edge and the tip. The electron wavelength depends on the bias by the DeBroglie equation:

$$\lambda = \frac{h}{\sqrt{2m_e eV}}. \qquad (1.8)$$

Where m_e is the mass of the electron, e is the charge of the electron and V is the potential difference between tip and edge. For this work, electron energies anywhere from 50-120 eV are used, which give a range of wavelengths from 1.1 to 1.7 Å.

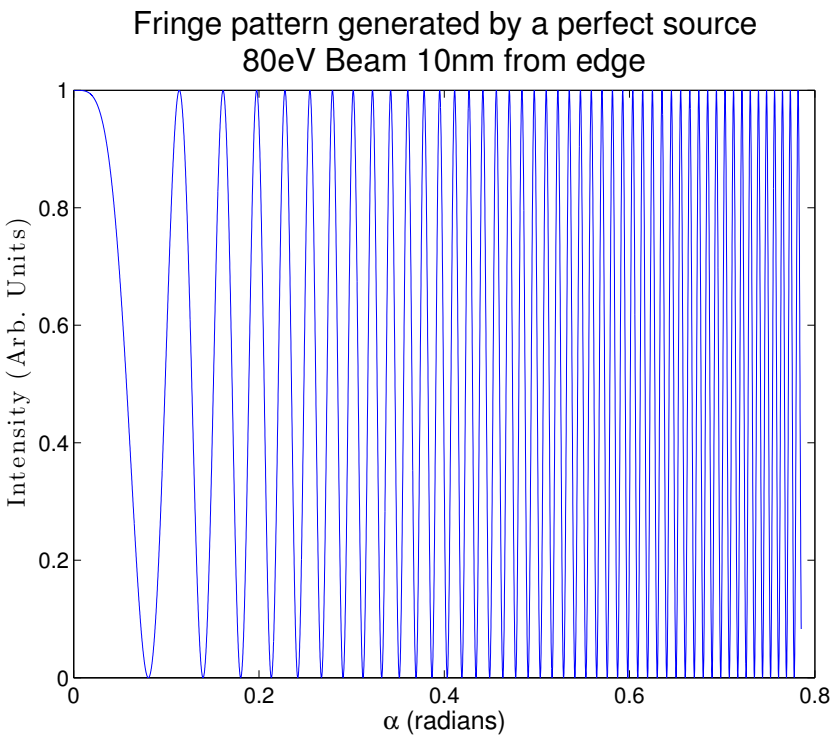

Figure 1.9: The interference pattern generated by scattering off a sharp edge by a perfectly coherent beam.

Any inhomogeneity in the kinetic energy of incident electrons in this experiment will results in a corresponding inhomogeneity in the wavelength of the incident electrons. All field-emission tips have some energy dispersion, ΔE, associated with their emission, which corresponds directly to a $\Delta\lambda$ from equation 1.8. It's easy to see how this $\Delta\lambda$ impacts the pattern: an independent interference pattern according to equation 1.7 is generated for each wavelength in that $\Delta\lambda$. Experimentally, what is seen at the detector is the composite of all the patterns for each $\Delta\lambda$, which results in lower visibility for higher order fringes. This is shown in Figure 1.10. Any variance in the incident wavelength will limit the numerical aperture, and ultimately the resolution, of the microscope.

The attenuation of higher order fringes can be seen by having a finite source size, or by any motion of the source relative to the edge. This causes a distribution in the value d in equation 1.7. Again, this can be thought of as a discrete interference pattern for each value d. The pattern read out at the detector is a sum of these patterns, which attenuates the visibility of the pattern, especially for higher-order fringes. This attenuation is shown for a variance in d of 5 Å in Figure 1.11.

Another way to think of this treatment is to notice the hologram of an ideal point scatterer (in this case, the edge), is a Fresnel zone plate. The Fresnel zone plate is a lens [17] and like any lens, the resolution is limited by its numerical aperture. To reconstruct the hologram it must irradiated with the same wavefront used to generate the hologram.

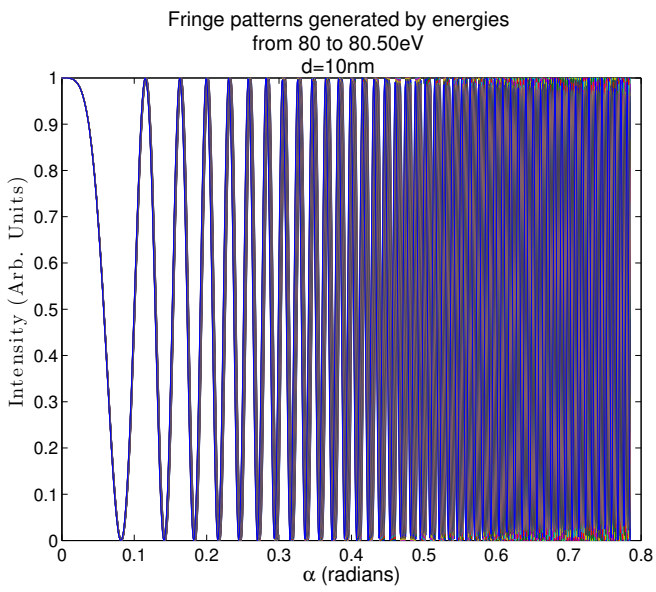

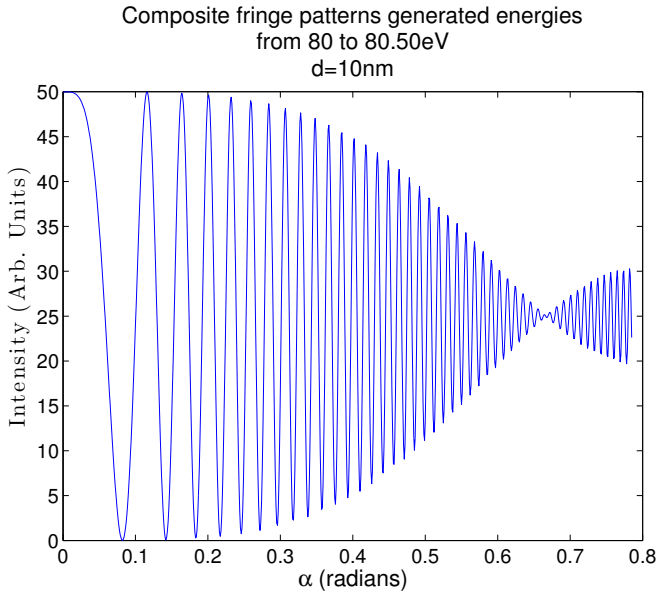

Figure 1.10: The interference patterns generated by the electron energy being varied by 50 meV in 1 meV steps and the total composite pattern generated. Figure at left shows each fringe pattern overlaid. At right is the sum of the fringe patterns showing attenuation of the higher order fringes.

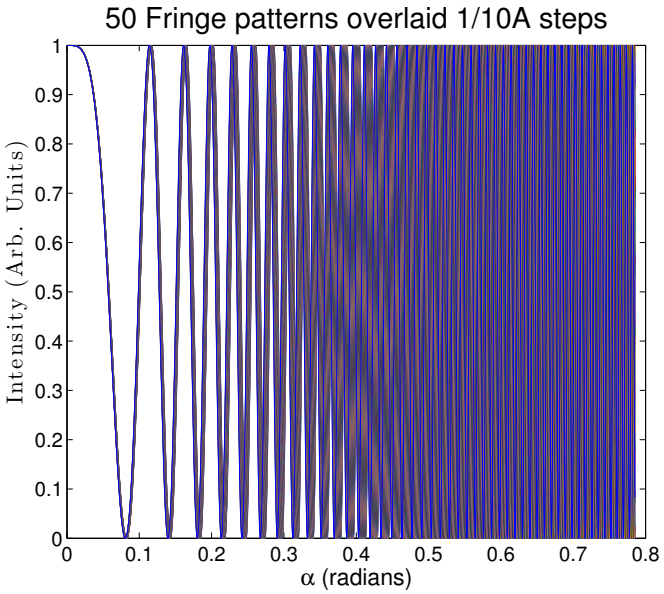

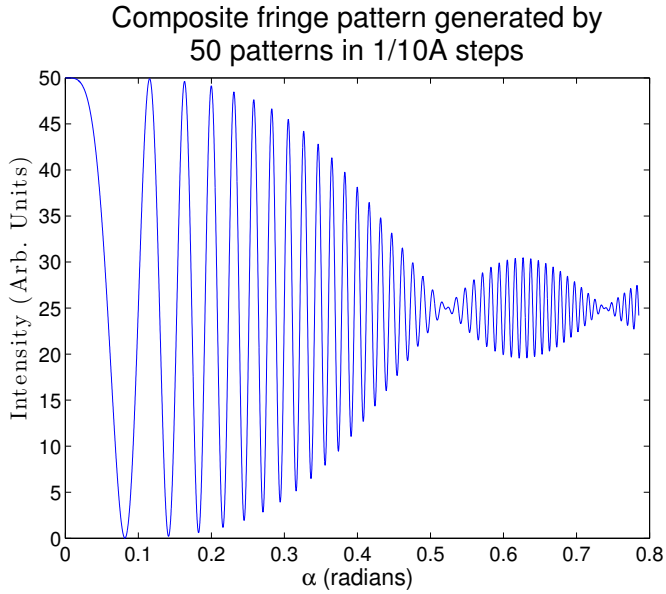

Figure 1.11: The interference patterns generated by tip-sample distance being varied by 1Å in 1/10Å steps. Left, each pattern is overlaid. Right, is the sum of the patterns, demonstrating the attenuation of higher order fringes.

Shown in Figure 1.12, irradiating the zone plate with this wave will focus it to a point, which is a conjugate image of the original point scatterer. The size of that focal point is the resolution of the hologram. During the formation of the hologram, incoherence of the wave limits the width of the hologram, which in turn limits the numerical aperture of the resulting Fresnel zone plate. This is how the coherence of the source is ultimately related to the resolution of the hologram.

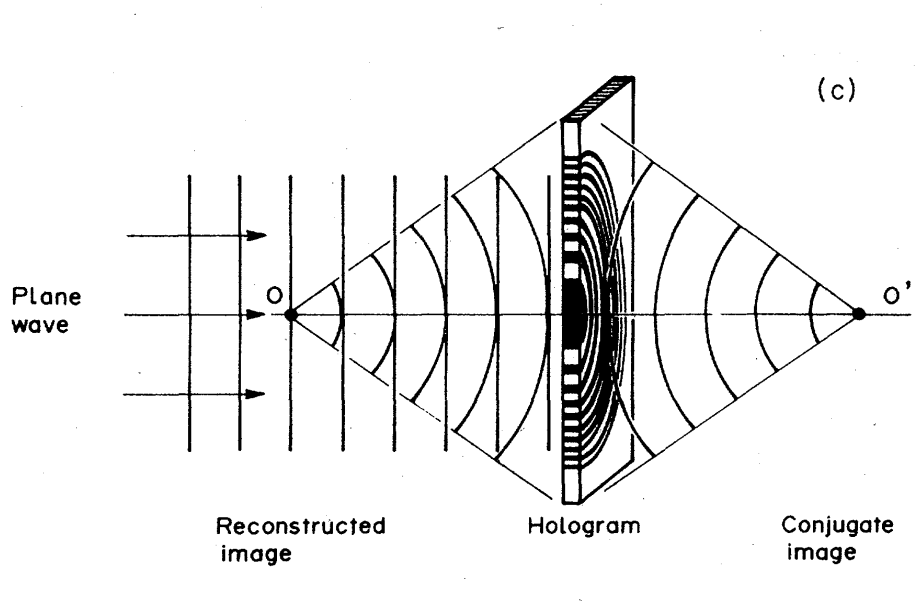

Figure 1.12: Holographic reconstruction of the point scatterer, reproduced with permission from [17]. By illuminating this pattern, a single point scatterer is reconstructed. The size of the point is inversely proportional to the size of the pattern as dictated by the numerical aperture.

1.5 Rationale for a fresh look

Because of its simplicity, electron holography can be realized naturally in a LEEPS microscope. There are several inherent advantages to this technique, along with recent technical developments, that warrant giving it an fresh look.

A hologram provides more than an image of the sample, it provides a map of the electron wave from source to detector. Because of this, the hologram is influenced by more than just simple scattering off the sample. Other processes, such as electric and magnetic fields, can be inferred from the hologram,

As previously mentioned, the potentials required to field emit electrons in a typical LEEPS setup require, at most, electrons of only a few hundred eV. As a result, LEEPS constitutes a much more gentle probe than traditional EM techniques. This reduces damage due to sputtering by incident electrons, and widens the class of material that can be easily imaged to softer materials. Hopefully, using proper preparation techniques, soft samples

with biological relevance that have escaped structural definition, such as proteins, may be imaged more easily using LEEPS and holography.

1.6 Something new

Electron holography has long promised, but never completely delivered. For the development of the technique, three areas of improvement were identified: the isolation of the system, the coherence of the source, and the reconstruction algorithms.

1.6.1 Isolation

Chapter 2 will discuss the design and construction of a microscope sufficiently isolated from the environment to visualize samples at the nanoscale. The microscope must be isolated from the environment in many ways; from particles that would contaminate the sample, from vibration that would shake the system, blurring signal, and finally from electromagnetic fields that might scramble the signal. Fortunately, the LEEPS setup contains the same ingredients as a scanning tunnelling microscope (STM). The microscope can be used in STM mode to get a direct measurement of the stability of the microscope - a measure that is absent from previous attempts in the literature.

It is also important to isolate the microscope from stray magnetic fields. Since the hologram is a measure of the entire electron wave, any unwanted fields that can distort that wave will complicate the reconstruction and interpretation of the images [9].

1.6.2 Source fabrication

Although LEEPS is a lensless technique, the source functions as a lens for many practical purposes. The divergence of the source limits the numerical aperture of the system, and structure of the tip dictates the spatial and energetic coherence. New techniques for crafting electron sources on the atomic scale are demonstrated in Chapter 3 along with a discussion of the impact of the source shape on the coherence of the instrument.

A microscope has been built with sufficient mechanical stability and coherence to bring promise to the technique of electron holography. By applying these many refinements, this work will demonstrate that LEEPS holography can be taken to the Angstrom scale.

Chapter 2

Designing the microscope

2.1 Overall design

When building a microscope to study matter at the nanoscale, there are many important considerations. The primary goal is to isolate the system under study to avoid contamination and noise from the environment. The secondary goal is to make a practical machine, in which samples can be changed with a high throughput and the system can be serviced with minimal interruption. Unfortunately, these two goals are often contradictory, which can be challenging to manage.

Most importantly, it is essential that the sample be completely free of contamination. This can only be accomplished by working in ultra-high vacuum (UHV) conditions, at a pressure less than $1x10^{-9}$ Torr. The challenge of UHV is primarily the restricted set of materials that can be used: metals and glasses and a few plastics that must be used sparingly. Because of this limited set of materials, it is very difficult and expensive to bring things from the outside environment into the UHV chamber, namely electrical signals, motion manipulation and new material such as electron sources and samples. The design of the chamber will be discussed in detail in a subsequent section.

The system also must be isolated from a host of other environmental influences, including mechanical vibration and electrical noise. Any unwanted motion of the tip relative to the sample must be significantly below the length scales being probed, or any signal will be washed out. This means that unwanted relative motions of the source and the sample must be well below the Angstrom level.

Because of the sensitive instrumentation required, great care must also be taken to avoid electrical noise. Ground loops, crosstalk and radiative pick-up must be painstakingly removed from the system by judiciously routing the wiring and electrically shielding critical parts, without compromising the vibration isolation. A further consideration is sheltering the system from stray magnetic fields, which scramble the relative phase of the electrons in holography, complicating reconstruction.

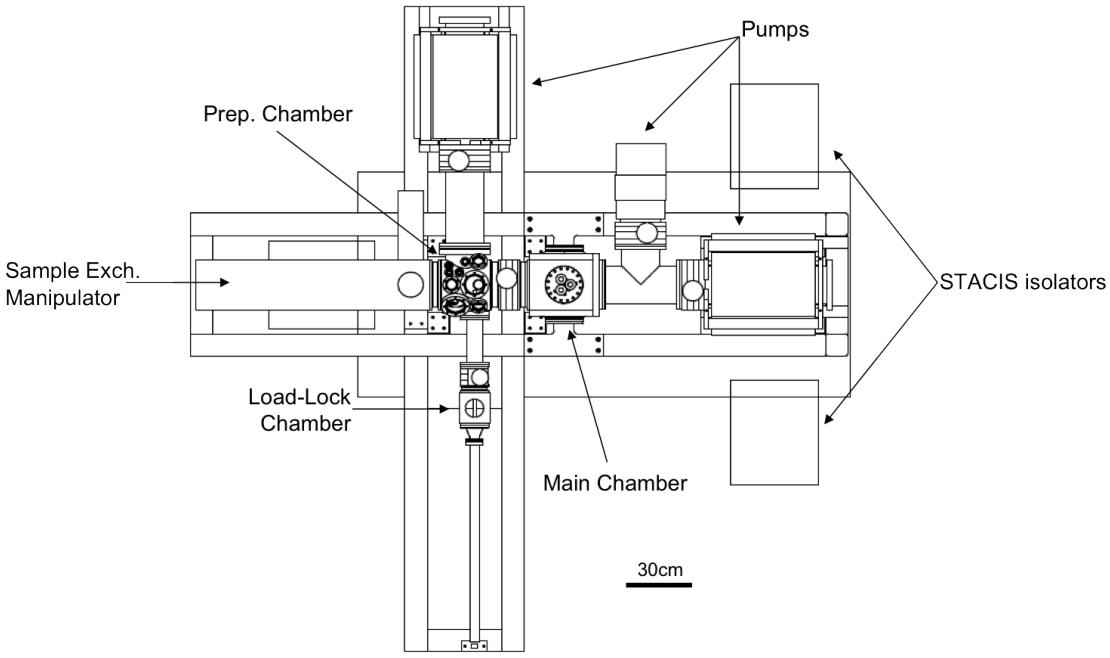

(a) Top view.

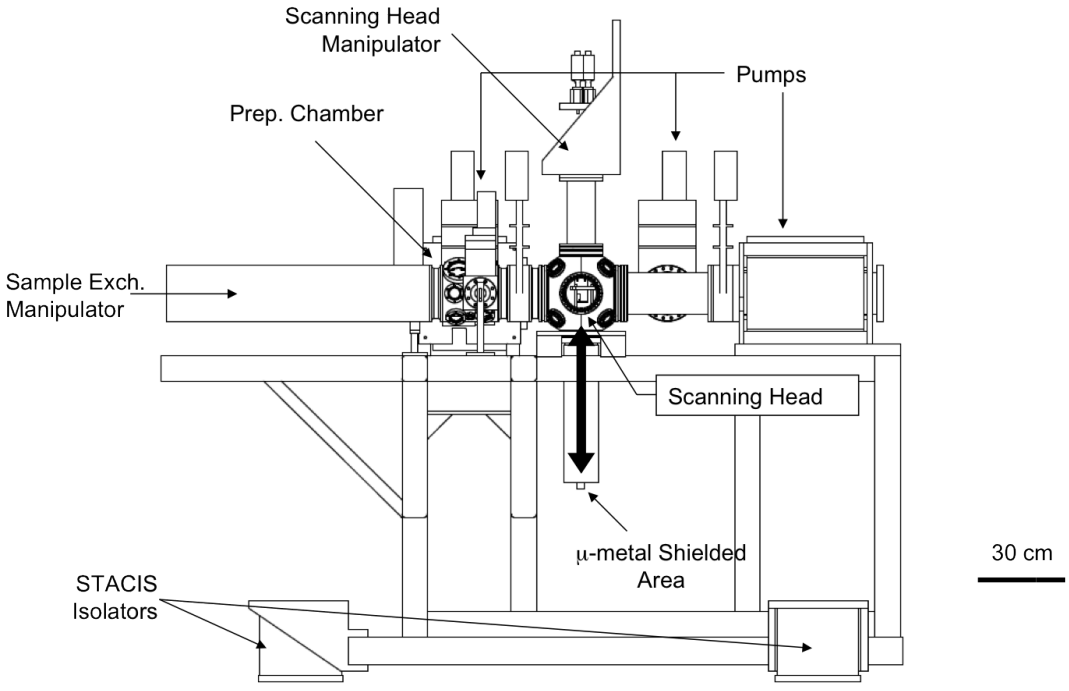

(b) Side view.

Figure 2.1: Drawings of the UHV system. Highlighted are crucial parts of the system. The pumps, the transfer system and three major areas; the load-lock, the preparation chamber and the main chamber.

2.2 Ultra-high vacuum chamber

In order to avoid contaminating the microscope, the entire optical system; tip, sample and detector, must be housed in a UHV system. This presents a number of challenges, most of which can be met with off the shelf technology, however intricate and specialized.

Although we are hardly ever aware of it, every surface we encounter in every-day life is covered with a film of oxide, water, and grease. On the scale which we usually interact with matter, it hardly matters, and the film is unresolvable in the most powerful optical microscopes. However, when examining samples at higher magnifications, the sample will be inundated with this layer, rendering it impossible to examine.

Removing this film can be done easily enough by many techniques: by heating the sample, or electron bombardment. However, if the sample is cleaned in our native environment, the film would return, instantly contaminating the sample. In order to make it take longer for this contamination to return to a pristine sample, the sample must be prepared in a high vacuum - the better the vacuum, the longer it takes for the contamination to return.

The system that houses the LEEPS microscope consists of three independently pumped chambers separated by gate valves: the load-lock, the preparation (prep) chamber and the main chamber. The system is pictured in schematic in Figure 2.1. The load-lock is a chamber containing only a tray designed to hold tips and samples, fixed to a magnetically actuated guide rod. Once samples are placed into the load-lock, it is pumped out using a turbo-molecular pump. Once the load-lock reaches a sufficiently low pressure (typically below $5\text{x}10^{-9}$ Torr), the load-lock can be opened to the prep chamber, where samples and tips can be cleaned or further prepared.

2.2.1 The preparation chamber

The prep chamber is the first UHV chamber to which samples and tips are exposed. It is mainly for cleaning samples by annealing and etching tips from >20 nm down to a single atom. It is meant to have a good enough vacuum to keep samples clean, but to isolate the main chamber from the processes that involve raising the pressure above UHV conditions. The prep chamber is pumped by 1 large 800L/s [18] ion pump and two titanium sublimation pumps. Most importantly, the prep chamber houses two important parts, the UHV pliers and the field ion microscope (FIM) setup. The FIM is used to obtain an atomic scale image of the electron source and to sharpen it to a single atom. It will be discussed in detail in Section 3.1.3. Besides the microscope itself, the pliers are the most critical component of the entire system.

2.2.2 Handling tips and samples: UHV pliers

In order to bring samples from the load-lock into the prep and ultimately into the scanning head, a set of UHV compatible pliers (pictured in Figure 2.2) was designed and built by

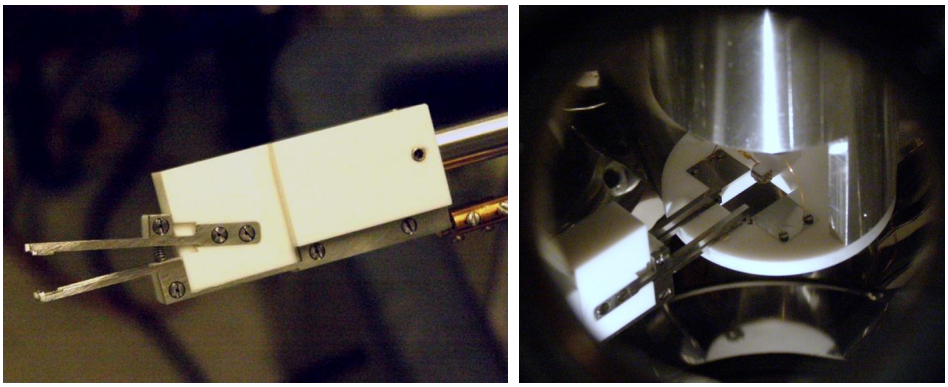

(a) Side view.

(b) The pliers in sample loading position on the scanning head.

Figure 2.2: The UHV pliers are used to move tips and samples between the load-lock, the prep chamber and the main chamber. Samples and tips are loaded in the jaws, which can be actuated open or closed.

engineer Mark Salomons. The pliers consist of two electrically isolated tantalum jaws, spaced 7 mm apart. The jaws can be used to pick up anything from tungsten wire (tips) to sheets of material with a maximum size of 3x14x0.5 mm. Once held by the jaws, current can be run through the tip or sample, resistively heating it for cleaning.

The pliers are mounted to a 5-axis manipulator with motorized motion in up-down, left-right, in-out and continuous rotation. The manipulator has a range of 2 inches in the up-down and right-left directions, and range of 18 inches in and out. To accommodate this large travel, the manipulator is housed in a large collapsable bellows. Continuous rotation is accomplished by using a differentially-pumped seal with 2 stages of pumping. In order to obtain a good base pressure, the high-vacuum stage is pumped by a mini-ion pump and the low-vacuum side is pumped by a small turbo. The fifth axis is a push-rod mounted to a smaller bellows that is used to open and close the pliers - this push-rod is actuated by hand.

2.2.3 The main chamber

Once samples and tips are prepared, they are brought into the main chamber where they are loaded into the scanning head. The main chamber houses the microscope itself, which consists of the scanning head and detector, a multi-channel plate (MCP): a spatially resolved electron detector. The scanning head is the device that holds a tip and sample, as well as all the machinery for moving the tip precisely relative the the sample. Once a tip and sample are loaded into the scanning head, it is lowered into a μmetal tube, near the MCP. μmetal is a material with a very low permeability which can be used to isolate the area within the μmetal from magnetic fields. The tip is biased negatively relative to the grounded sample, and electrons are emitted through the sample, towards the detector, resulting in a magnified image on the detector. The scanning head is discussed in detail in Section 2.2.4.

The main chamber itself consists of two major areas: the loading area and the shielded area. As previously mentioned holography is very sensitive to magnetic fields and the experiment must be carried out in an environment with less the 0.1mG magnetic field impinging laterally on the optical path [9]. To accomplish this, the scanner is lowered into a μmetal tube to generate a hologram and raised into the loading area, where it can be reached by the pliers, when exchanging tips and samples.

To raise and lower the scanning head, it hangs from the top flange of a bellows linear translator by a long spring. All the wiring for the scanning head is fixed to an aluminum rod mounted coaxially with the bellows. As a result the scanning head, the spring and all the wiring move up and down as a unit, to avoid parts coming into conflict with flexing wires or springs.

The main chamber is pumped by another 800L/s ion pump [18] with two titanium sublimation pumps. Also attached to the main chamber is a large 550L/s [19] turbo-molecular pump - which is only used to provide extra pumping during bakeout.

2.2.4 The scanning head

The core of the microscope consists of three main components: tip, sample and detector. The tip and sample are housed in what is called the scanning head. The magnification and area of interest are controlled by the relative position of the tip and sample; the closer the tip, the higher the magnification. The area on the sample within the electron beam is imaged on the detector some distance away. To achieve magnifications of the order 10^6 the tip has to be within a hundred nanometers of the sample. To this end, a scanning head, not unlike as (STM), was designed. A diagram showing the scanning head is shown in Figure 2.3. The tip is held by three coarse motors, one for movement in each direction [20], and a piezoelectric tube-scanner for fine positioning above the sample. The coarse motors are used to move the tip within a millimetre of the sample. The coarse and fine scanner are used in concert to approach the tip closer to the sample. This combination of coarse and fine scanners allows the microscope to image fields of views ranging from nanometers to several hundreds microns.

The wiring for the scanning head is a cable fixed to an aluminum rod. The electrical feedthroughs are installed at the top of the bellows and the scanning head and all its wiring move up and down in unison. To isolate the scanning head from vibrations carried by the wires, a mechanical break consisting of a wiring harness made from thin, 38-gauge wire, connects the end of the cable to the scanning head itself. The wires themselves are twisted-pair for the fine scanner and coarse movers, single conductor for the sample bias and a coaxial wire for the tip. The coaxial tip wire uses its own feedthrough with an isolated shield to reduce inductive pickup and crosstalk and ground loops.

Because of the sensitivity to magnetic fields [9], no eddy-current damping can be placed near the scanner. In order to hang in a sufficiently shielded area and have the travel to be

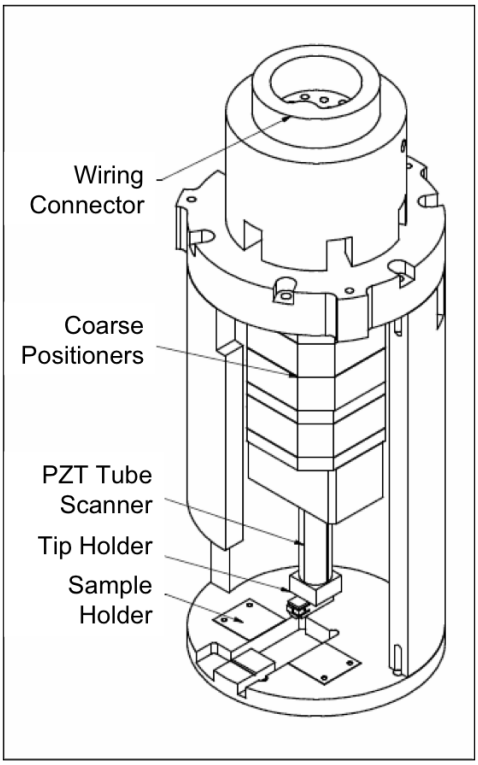

Figure 2.3: A cut-away view of the scanning head. Inside the aluminum body are three coarse-motors for positioning the the within a hundred nanometers of the sample. The tip is attached to a fine piezoelectric tube scanner, with sub-nanometre precision. The sample is held below the tip over a gap, so electrons can be projected through the sample towards an MCP.

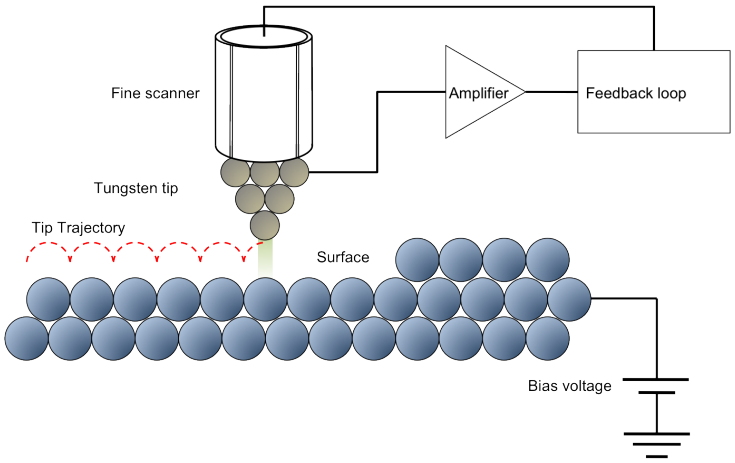

(a) How STM works.

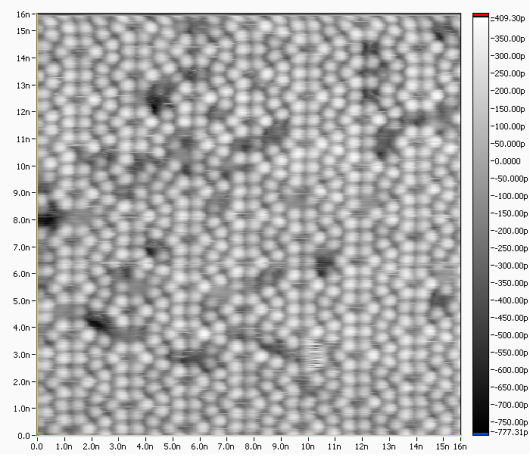

(b) An atomic resolution STM image of a Si(111) surface obtained with the microscope.

Figure 2.4: Scanning tunnelling microscopy.

lifted into the exchange area, the scanner must hang 1.1 m below the top of the bellows - a long distance compared to a typical STM. This long distance, along with the lack of damping at the scanner required us to explore an innovative solution to achieve sufficient mechanical isolation and damping.

2.3 Testing the microscope

2.3.1 Scanning tunnelling microscopy

As mentioned above, the scanning head is essentially an STM. In an STM, a sharp tip is approached to a biased sample until electrons start tunnelling between the tip and sample. The tip is connected to a very sensitive current amplifier which detects the minute *tunnelling current* between tip and sample. Depending on the sample and the applied voltage, a current on the order of hundreds of pA will tunnel between tip and sample when the tip is a few Angstroms from touching the sample. This tunnelling current depends exponentially on the separation between tip and sample, which makes it an excellent probe of topography on the Angstrom scale. Usually, the tip is held at a constant current set-point by a feedback loop, this keeps the tip from being damaged by crashing into the sample. To generate an image, the tip is scanned in a line over the sample, while the feedback loop adjusts the height of the tip keeping the current constant. The height profile is recorded for each line, and a three-dimensional image of the tip-height as a function of position is generated by rastering the tip across the sample. This is shown in Figure 2.4a.

Because it is such a sensitive imaging tool, STM is also an exquisite tool for testing the mechanical and electrical stability of the microscope. Minute vibrations between tip and sample will be read in the tunnelling current, which allows for a direct measure of mechanical stability. Also, any electrical noise, from crosstalk, ground loops or radiative pickup will be

induced in the tunnelling current, which is amplified by 10^9 V/A. If the microscope is stable to within 0.1 Å in STM, it will be as stable in LEEPS as well. An image, demonstrating the mechanical stability of the microscope to be sufficient for obtaining atomic resolution images in STM is shown in Figure 2.4b.

2.3.2 Preparing silicon surfaces

A fine standard for imaging on the atomic scale is the (111) face of a silicon crystal. The (111) 7x7 reconstruction of the silicon surface is particularly forgiving because the surface forms a two-dimensional metallic conductor, the atomic corrugations are quite high and the surface is very stable. This makes achieving atomic resolution easier in Si(111) 7x7 than in other surfaces.

To prepare a surface an Si(111) wafer is cut into 14x2.5 mm rectangular chips. A chip is loaded into the prep chamber and picked up by the pliers where it is heated to 600°C overnight, to degas the chip and the pliers. After the degassing cycle, the pressure in the prep chamber should be below $1.5\text{x}10^{-10}$ Torr with the crystal at 600°C. Next the crystal is heated by an additional few hundred degrees, until the pressure spikes to the mid 10^{-9} Torr range. The crystal is allowed to cool until the pressure recovers to the mid 10^{-10} Torr range. This is done repeatedly, each pulse hotter than the last and lasting a few seconds until the temperature of the crystal reaches 1250°C. The crystal is held at 1250°C for a few seconds at a time and is repeatedly flashed to this temperature until the pressure stays well within the 10^{-10} Torr range. Typically this requires five or so flashes for a fresh crystal, and fewer for a crystal which has been cleaned before. The crystal is allowed to cool for a few minutes and loaded into the scanning head for STM.

2.4 Mechanical isolation

As mentioned in Section 2.2.3, the scanning head hangs from a long spring. This is the last stage in the system to isolate the scanning head from external vibrations. The task is essentially to make the scanning head into the world's worst microphone; to ensure any vibration present in the environment is not picked up by the microscope. This is an arduous and painstaking task, in order to achieve atomic resolution.

2.4.1 Transmission of mechanical noise

To eliminate noise, it is first necessary to know what noises are present and to understand how it is transmitted to the scanning head. Vibration transmission in the microscope is best understood by examining the model system of two coupled masses, as in Figure 2.5. Consider a load with mass m, coupled to a foundation with a mass $m_f \gg m$ through a spring with constant k and viscous damping c. This is known as a passive isolator; the equations of motion for this stage are [21][22]:

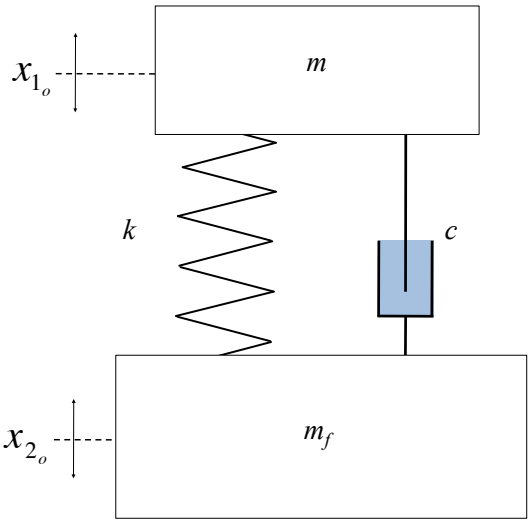

Figure 2.5: A schematic of transmission of vibration from the environment to a mass m. The mass is coupled to the floor by a spring with constant k and a viscous damper c.

$$\begin{aligned} m\ddot{x_1} + c(\dot{x_1} - \dot{x_2}) + k(x_1 - x_2) = 0 \\ m_f\ddot{x_2} + c(\dot{x_2} - \dot{x_1}) + k(x_2 - x_1) = 0. \end{aligned} \tag{2.1}$$

A convenient metric for studying the isolation properties of the system is the ratio of displacement of the foundation and the load. To study this, suppose the foundation is displaced sinusoidally by an amplitude x_{2o} and a frequency ω: $x_2 = x_{2o} \exp i\omega t$. To satisfy equations 2.1, solutions of the form $x_1 = x_{1o} \exp i(\omega t + \phi)$ yield the ratio of displacements for a given frequency ω:

$$\frac{x_1}{x_2} = \frac{k + icw}{(k - mw^2) + icw}. \tag{2.2}$$

The absolute magnitude of this ratio, known as μ_x, the amplification factor, or gain, simplifies to:

$$\mu_x(\omega) = \frac{|x_1|}{|x_2|} = \sqrt{\frac{1 + \left(2\zeta\frac{\omega}{\omega_o}\right)^2}{\left(1 - \frac{\omega^2}{\omega_o^2}\right)^2 + \left(2\zeta\frac{\omega^2}{\omega_o^2}\right)^2}}. \tag{2.3}$$

Where $\omega_o = \sqrt{k/m}$ is the natural frequency of the spring-mass system, $\zeta = c/2m\omega_0$ is a quantity known as the relative damping.

Equation 2.3 represents the frequency response of the coupled two mass system. It describes how well vibration in the foundation is transferred to the load over a range of frequencies. The passive isolator is essentially a low-pass filter for mechanical signals.

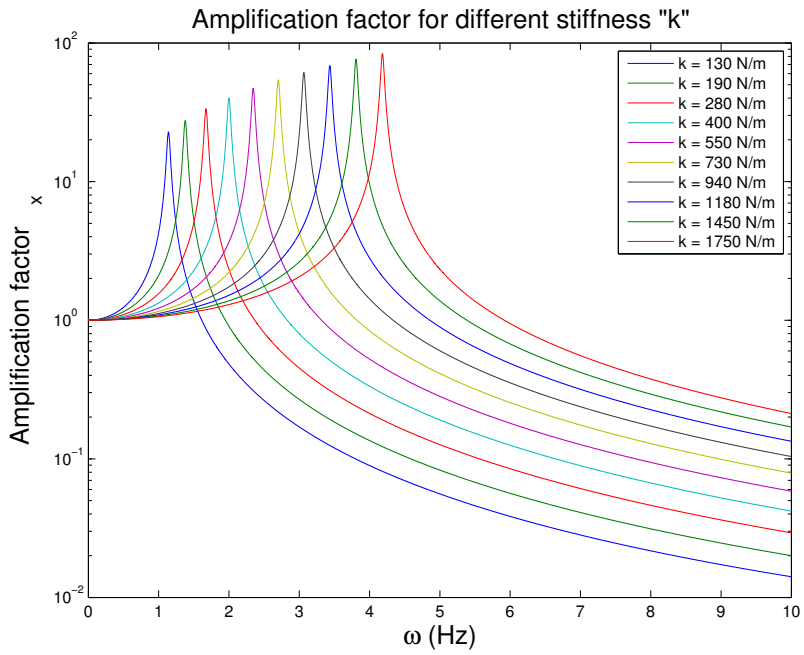

Figure 2.6: The effect on the gain of the isolation stage by varying k.

We can use this result to gain insight about what makes a good vibration isolation system. Remember, we need a microscope with as little vibration of the tip and sample relative to each other. The easiest way to accomplish this is to use passive isolation. However, there are a few parameters that need to be optimized. Typically, most scanned probe microscopes are isolated by the suspension from some kind of springs. The natural frequency of such a setup is equal to the extension of the spring under load Δx:

$$\omega_o = \sqrt{\frac{k}{m}} = \sqrt{\frac{g}{\Delta x}}, \tag{2.4}$$

where $\Delta x = mg/k$ at equilibrium.

The easiest parameter to vary is k, the stiffness of the spring suspending the scanner, by choosing different springs. Changing the mass of the scanning head is often difficult, since it involves designing and machining new parts. The effect of varying k can be seen in Figure 2.6; the softer the spring, the lower the resonant frequency of the isolator, and the greater attenuation at frequencies above the resonant frequency. This has the effect of transmitting the motion below the resonant frequency with no attenuation and amplifying motion near the resonant frequency. To achieve the most isolation, the softest spring possible must be chosen while keeping in mind the tensile strength of the springs.

The next parameter is the amount of damping in the system. Introducing damping to the system removes energy from the system. However, there is a balance that must be struck with damping. First, as can be seen in Figure 2.7, there is a clear tradeoff gained by increasing damping: an increase in damping reduces the amplification of the isolator at

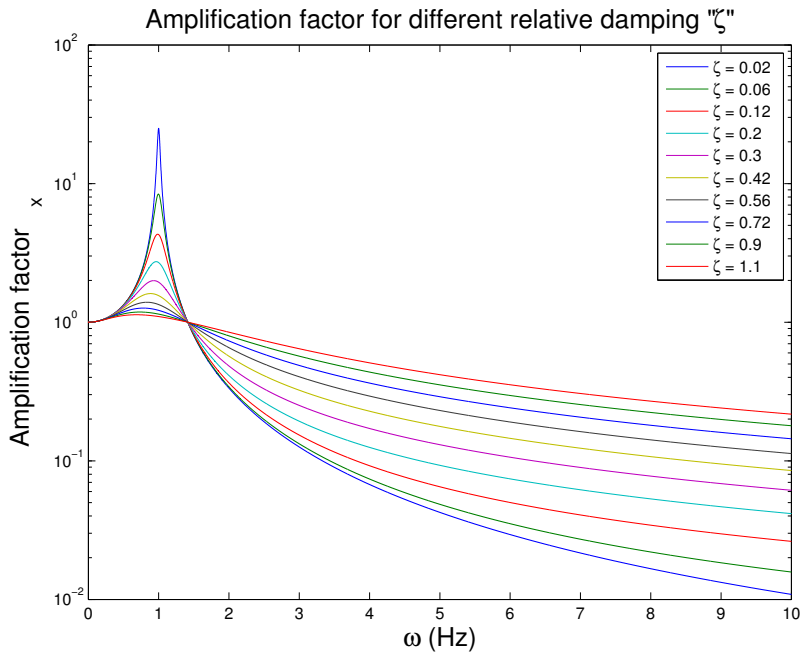

Figure 2.7: The effect on the gain of the isolation stage for varying ζ.

resonance but also increases the amplification of the isolator at higher frequencies. Secondly, from a practicality perspective, a system with insufficient damping with oscillate for a very long time if perturbed. Little or no damping renders the microscope effectively unusable, since a small disturbance due to realigning the microscope, or loading a tip or sample, will set the scanner into an oscillatory motion for a very long time. During this oscillation, it is impossible to use the microscope. A damping time for the system on the order of the amount of time it takes to acquire an image is a useful figure of merit. This means if the system damps in the time it takes to acquire one image (usually a minute or two) the damping is not upsetting the productivity of the instrument too much.

A simple way to improve vibration isolation is to have a few stages of isolation [23, 21, 24]. In this way, the resonance of one stage can be isolated by the other, so less noise is communicated to the microscope overall. Mathematically, the effect of multiple stages can be modelled by multiplying the amplification factors of each stage (equation 2.3), to get the overall amplification. Far greater isolation is achieved above the resonant frequencies of both stages, this can be seen in Figure 2.8. The construction of a typical UHV microscope offers two convenient opportunities for isolation stages.

2.4.2 Stages of vibration isolation

To build a quiet microscope, is must be housed in the quietest environment possible. Fortunately, the *characterization area* at the National Institute for Nanotechnology (NINT) provides some of the quietest research space in Canada. The largest source of noise for

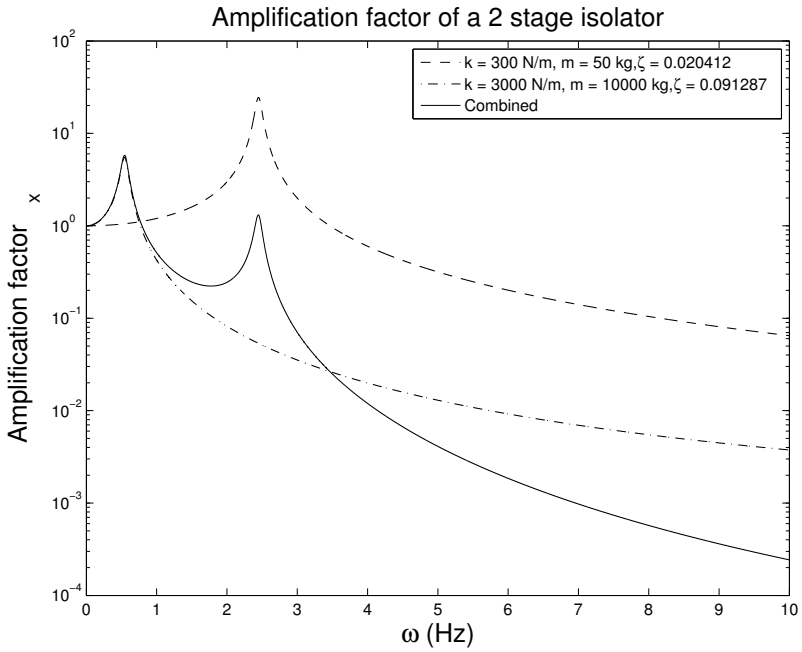

Figure 2.8: The effect of combining 2 stages of isolation.

a system such as ours in coupled in through the floor. The characterization area has a quiet floor for a few reasons. First, the floor is built on grade, there are no floors below, just concrete. This makes for a quiet floor, because the floor is totally supported. A lab with an unsupported floor will vibrate in a manner not unlike a drum. Secondly, the characterization area is mechanically isolated from the rest of the building and all of the air conditioning is mechanically isolated from the lab space. This reduces noise by decoupling the mechanical vibrations present in the rest of the building.

2.4.3 First stage of isolation: active isolation legs

Although the characterization area is a good start, it's far from perfect and the microscope needs to be isolated. The **first stage** of vibration isolation is between the floor and the UHV system itself. The system is built on a heavy platform. That platform is supported by three STACIS legs. The entire assembly is made to be as heavy as possible so as to lower its resonant frequency as much as possible. The STACIS legs are special supports designed to actively cancel incoming vibrations coming from the floor [25]. A transducer coupled to the legs detects incoming vibrations to the floor. This signal is amplified and fed into a piezo stack which applies the opposite signal nullifying the vibration. The system is designed to work over a wide bandwidth and cancels noise from less than 1 Hz to 200 Hz [26]. The effect of the STACIS legs on our system can be seen in Figure 2.9. They provide an order of magnitude reduction in vibration below 3 Hz, but almost no isolation between 5 Hz and 12 Hz.

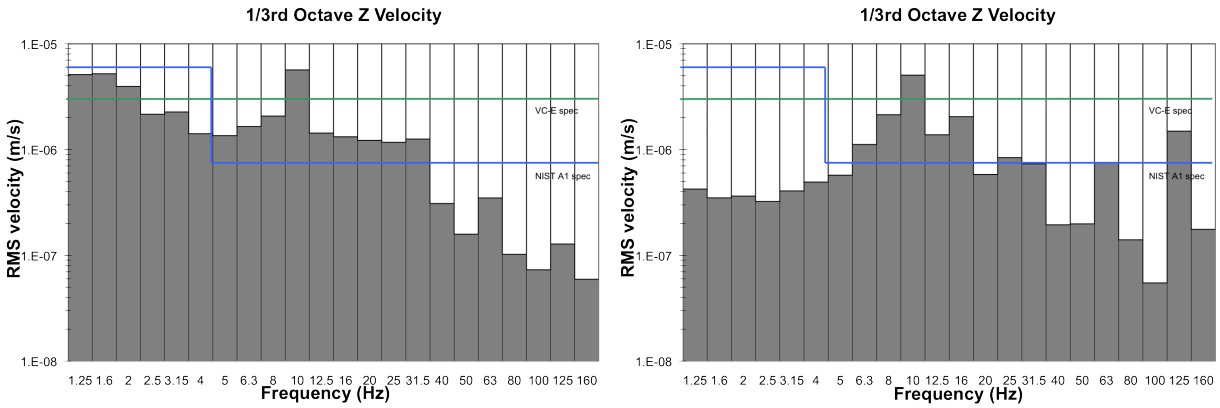

Figure 2.9: A 1/3 octave plot of the vibration on the floor of the lab (left) and on the STACIS supported platform (right). Frequency is binned in bandwidth sections 1/3 octave wide. The velocity as read by an accelerometer. This velocity is displayed on the vertical axis. The STACIS system provides isolation at low frequencies, below 5Hz.

This gap in the vibration reduction may be because the system itself is too tall and not rigid enough. The system has its own acoustical properties, which feed back vibration into the legs. This is something that can hopefully be mitigated in the future by reducing the overall height of the system, and stiffening the frame. Similar systems have introduced plates made of viscoelastic polymers and metal between the legs and the platform to achieve more passive reduction.

2.4.4 Second stage of isolation: hanging the scanning head

The **second stage** of vibration isolation is inside the chamber itself. Typically, a scanned probe microscope like this one is hung from three soft springs in the vacuum chamber. As a result, the springs and stage have a relatively low resonant frequency, filtering noise effectively above that frequency. Usually the microscope will have metal fins mounted to it, with chamber-mounted magnets interleaved within those fins. When the scanner moves, the fins move within the magnetic fields, producing an eddy current in the fins, which opposes the magnetic field, damping the motion of the scanner. This is know as eddy-current damping, and is a simple way of removing kinetic energy from the scanner.

Unfortunately, since this microscope needs to be isolated from magnetic fields, it is impossible to employ eddy-current damping near the scanner. An early solution was to suspend the scanning head from three long springs with magnets fixed coaxially within the springs. When the scanning head was lowered to the region where it would operate, the magnets would be located in the aluminum tubes, as shown in Figure 2.10. The hope was that the motion of the magnets within those tubes would introduce sufficient damping. There were several challenges in building this isolator: first, the springs themselves had to be made of a material which was UHV compatible, with a high working temperature (to withstand bakeout), that was also non-magnetic. Unfortunately, most spring alloys are rich

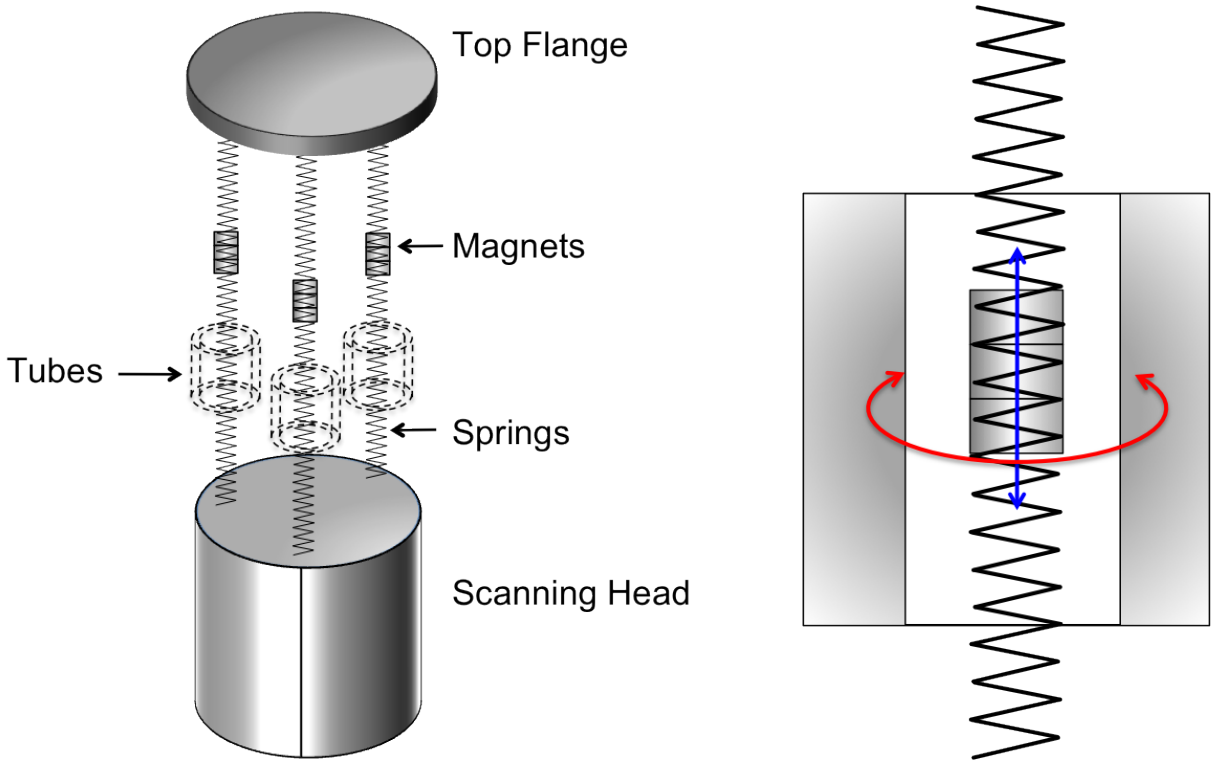

(a) A diagram of the the scanning head hung from springs. The top flange can be lowered until the magnets are within the tubes.

(b) A section view of the magnet and spring lowered into the tube.

Figure 2.10: An early solution to provide passive damping for the scanning head involved suspending the scanning head from long springs. The springs had magnets mounted coaxially that would be lowered into aluminum tubes, when the scanning head was in the operating position. The motion of the magnets in the aluminum tubes would provide damping.

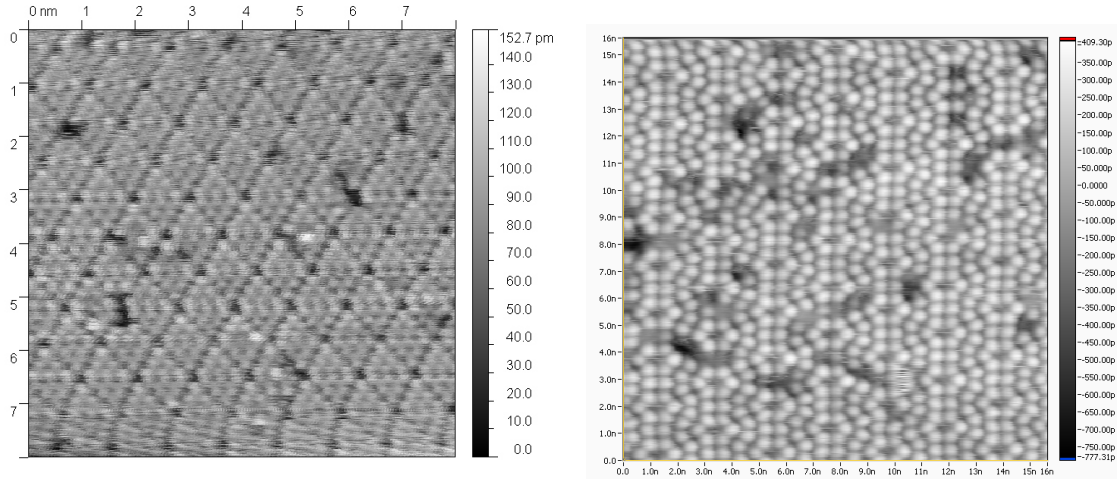

(a) STM image with the scanner hanging from the springs.

(b) STM image with the scanner hanging from Viton cord.

Figure 2.11: A comparison of STM imaging with the scanner suspended from TiAlV springs and from Viton cord. The difference in the definition in the images is striking. While atoms can be resolved in both images, the level of noise in (b), with the scanning head suspended from Viton cord, is far less.

in nickel, and those that aren't seldom have a high working temperature. The most readily available material was an alloy of titanium which is composed of 6% aluminum and 4% vanadium by mass, known as Ti6Al4V. There were no commercial sources of springs made of this material at the time, so as-drawn wire was purchased from Goodfellow and coiled by a local company, City Spring.

However, there were many problems with the aforementioned setup. Hanging each spring inside a tube narrow enough to provide any damping at all made it very difficult to align the springs in the tubes without touching them, shorting out the mechanical isolation. Moreover, with the springs painstakingly aligned, there was still a significant amount of motion communicated to the scanner. At best, 0.2 Å oscillation was seen while acquiring STM images. While it was still possible to image a silicon (111) 7x7 crystal with atomic resolution, it was very noisy, as shown in Figure 2.11a. This amount of noise would be a resolution limiting problem in holography. By taking a power spectrum of the noise (shown in Figure 2.12), it was seen that the oscillation had a resonance near 14 Hz and higher harmonics.

It was thought that this 14 Hz oscillation was a mode of the springs, which was undamped. This was confirmed by bringing in the pliers to touch the springs. This changed the frequency of the oscillation, like changing the pitch of a guitar string by moving a finger along the fretboard. Because there was not enough damping in the isolator, noise was being coupled into the scanner.

To introduce more damping, the springs and magnets were removed and the scanning head was suspended by a Viton cord. Viton was chosen because it is a UHV compatible viscoelastic polymer with excellent damping properties [24, 27]. One continuous cord was

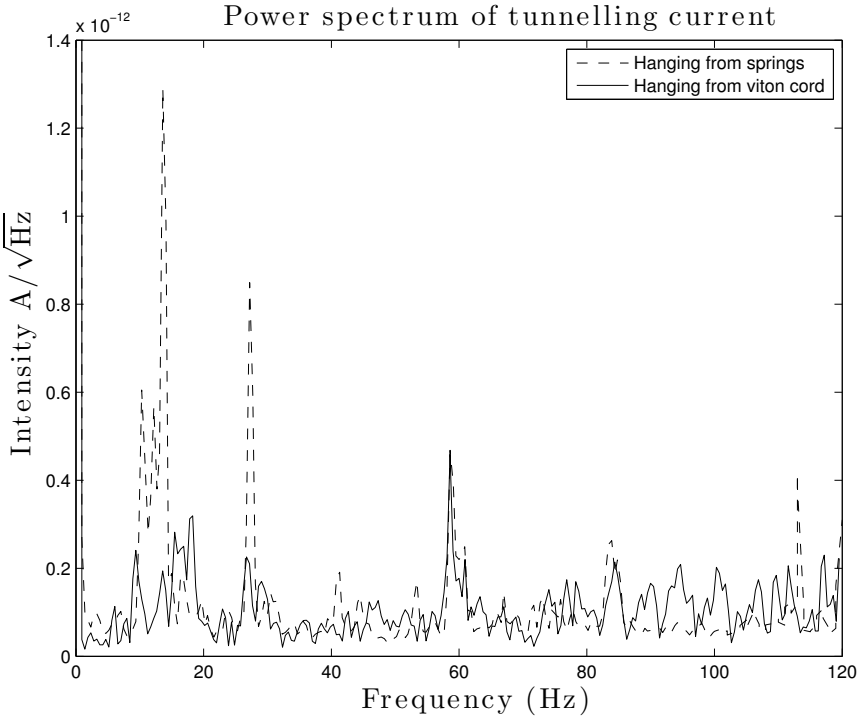

Figure 2.12: Comparing the tunnelling current signal of the scanner hanging from the springs and from the Viton cord. The overall level of noise is reduced by several times with the Viton cord.

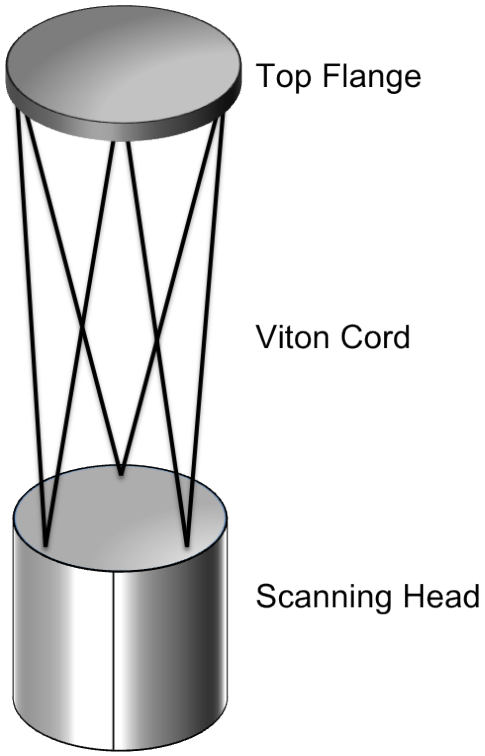

Figure 2.13: A diagram of the Viton cord vibration isolation and damping for the scanning head.

threaded between the three mounts on the top flange, through the three mounts on the scanner as shown in Figure 2.13. This arrangement was used to achieve effective damping of the vibrating scanner-cord system, since each direction of motion of the scanner is coupled to stretching of the Viton cord. Although the Viton is not as soft a spring as the TiAlV, it is sufficient to isolate the scanning head. Moreover, the damping inherent to the Viton cord itself and requires no alignment of the scanning head or cord relative to external features to introduce damping. The system is damped just as effectively regardless of where it is suspended. By switching to the Viton cord, the system was made simpler and the noise level in the system was reduced to the point where the relative motion between tip and sample was below 0.1 Å. The difference can be seen by comparing an STM image obtained with the scanning head suspended by Viton cord in Figure 2.11b, to the image obtained while the scanning head was suspended by springs in 2.11a.

2.4.5 Working principle of the Attocube movers

In order to move the tip relative to the sample over distances of several millimetres, a coarse motor must be used. The term 'coarse' is relative to the distances discussed in microscopy and refers to movement over distances of several milimetres with a step size of tens of nanometres. Typically, coarse motors use a stick-slip motor with piezo-electric actu-

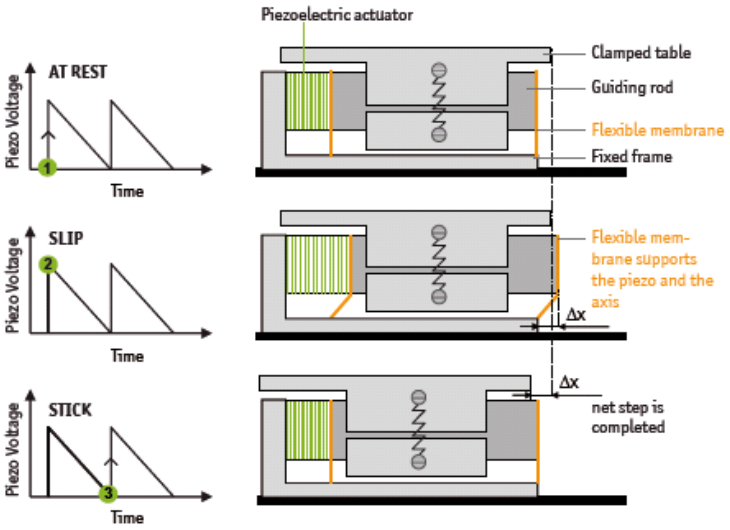

Figure 2.14: The working principle of the Attocube movers. (Figure used with permission of Atto**cube** systems AG.).

ator. The motors used in the scanning head are totally non-magnetic and are commercially available from atto**cube** systems AG.

The working principle of the Attocube motors is shown in Figure 2.14. The load of the motor is attached to a table, which is clamped to a rod by a precisely tuned force. The rod is suspended between two flexible membranes, one of which is pressed against a piezo-electric block. The piezo-electric block is polarized so that increasing the voltage across the block causes it to expand along the axis of the rod. When the voltage is increased very quickly, over a few microseconds, the piezo pushes the rod very rapidly so that it slides within the clamped table. The inertia of the loaded table holds it nearly totally still. The voltage is then slowly decreased, pulling the table over the distance which the rod was hammered into the stage. This is how the motor is moved one step. The motor can be moved by a train of such pulses, where the voltage is raised very quickly and lowered slowly, to move many steps. The greater the amplitude of the pulses, the larger the individual step. The higher the frequency of the pulse train, the faster the translation. The pulse can be reversed, with a slow increase followed by a sudden decrease, to reverse the direction of travel. Normally, the motor operates at 20 V and 1000 Hz.

The chief advantage Attocube offers over other commercially available motors is that they are made of entirely non-magnetic components. Most commercially available motors use magnets to control the friction between the load and the guide; Attocube uses a spring-loaded clamp. This is critical in this microscope, since stray magnetic fields have to be eliminated near the experiment in order to preserve the relative phase of the electrons in holography.

However, there are disadvantages to the Attocube motors. Each mover can only travel along the direction specified by the guide rod. Practically, it is necessary to have motion in

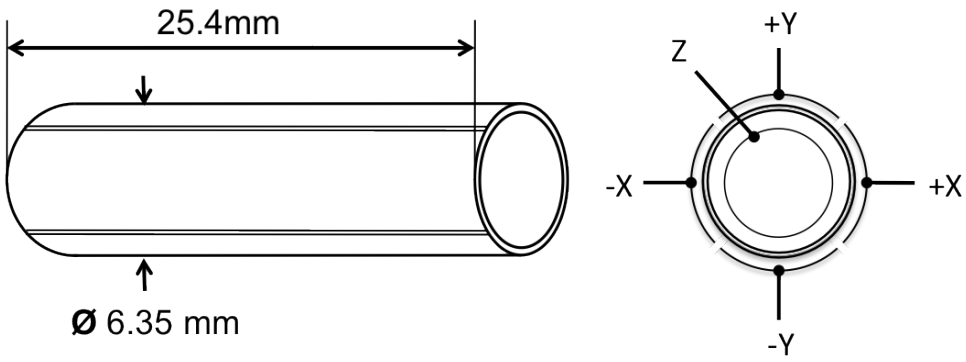

Figure 2.15: A diagram of the quartered electrode tube scanner. The hollow cylinder of the tube scanner is metallized with 5 electrodes; 4 outer electrodes and 1 inner electrode. The outer electrodes are biased to control the deflection of the tube laterally. The inner electrode controls axial expansion or contraction.

3 axes with as much travel as possible. This means three Attocube movers are necessary. Since the movers are designed to stack, one on top of the other, the assembly required to move in the 3 axes is at least 44 mm tall. The taller the mechanical system, the more inherently unstable it is and the lower the resonant frequency of the system. If the resonant frequency of the system is not in the bandwidth that is filtered by the passive isolators, more noise will be introduced into the system. The drawback is that using the Attocube motors makes the system more inherently susceptible to mechanical noise. Recently, a company called SmarAct has begun offering a line of lower profile non-magnetic motors, which may be used in the future to replace the Attocube motors, to make a more noise immune microscope.

2.5 Wiring and avoiding electrical noise

2.5.1 The scanning head wiring

Communicating with the scanning head presents its own set of challenges. First, only UHV compatible wiring and connectors can be used. This means that wires with teflon or Kapton insulation are required. There are three kinds of cabling used for the scanner, single conductor, twisted pair or coaxial. The choice of cabling depends on the signal, and the goal is to send and read electrical signals to and from the scanner with as high fidelity as possible.

A twisted pair is used when the circuit being wired has a forward and return line. The forward and return lines are twisted together so that any incident electromagnetic interference cancels out in the circuit as common mode noise. Moreover, in a balanced twisted pair, where the forward and return lines are equal in voltage but opposite in sign, the effective interference due to the pair is drastically reduced. There are several circuits in the scanning head with forward and return lines: the three Attocube coarse movers and

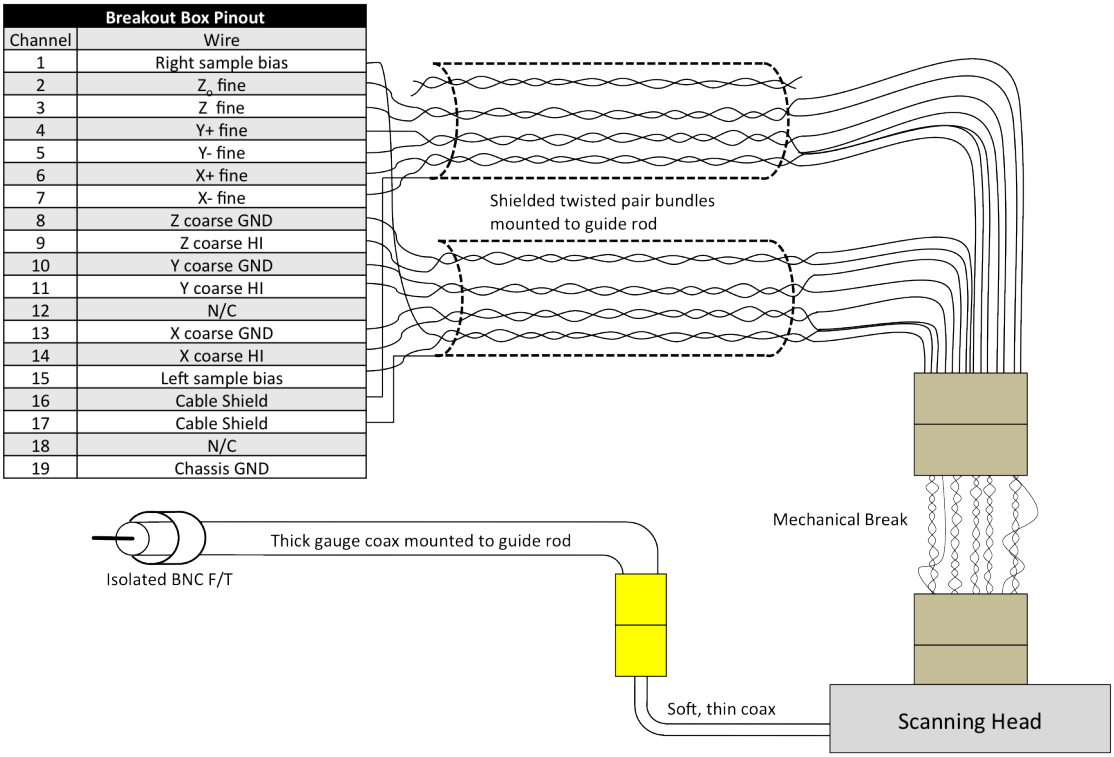

Figure 2.16: A complete wiring diagram of the scanning head.

the X and Y channel on the fine piezo-electric tube scanner. A twisted pair powers each of these circuits.

The tube scanner is used to move the tip with Angstrom precision. It is a hollow cylinder of piezo-electric material, polarized radially. The exterior is coated with metal, split into four equally-sized quadrants (see Figure 2.15); with the interior entirely coated in metal. To displace the tube scanner, when a voltage is placed across the opposite electrodes, the tube deforms in that direction, displacing the tip. The absolute displacement depends on the voltage applied. The tip will displace 80 nm/V of potential difference across the opposite electrodes. The tube can be deflected and the tip can be moved in an arbitrary lateral motion by applying to appropriate voltage across the electrodes. By placing a bias on the inner electrode, the tube can be made to lengthen or contract, raising and lowering the tip with a gain of 45 nm/V.

Because the exterior electrodes are biased by an equal but opposite signal, the leads to those electrodes make a perfect balanced twisted pair which will cancel out much of the induced interference due to sweeping the voltages of the electrodes while scanning the tube. Since the wire biasing the inner electrode, Z, does not have a balanced pair, it is twisted with a wire, Z_o (as shown in Figure 2.16) for the entire in-vacuum run of the wire. Z_o is not connected to anything, but a voltage equal to -Z can be applied to it, more effectively cancelling electromagnetic interference from the pair.

The system is wired as follows: starting from the air-side, wires are interfaced through a 19-pin breakout box, connected to a MIL-C UHV feedthrough. The pin-out of a MIL-C connector is shown in Figure 2.17. The breakout box itself has 19 female BNC connectors on one side, which are connected to the corresponding channels on a female MIL-C twist-lock connector. Each wire inside the breakout box is a coaxial cable with the shield grounded to the metal body of the breakout box. The MIL-C connector contains 19 individual, single-conductor pins in a honeycomb pattern.

The in-vacuum wiring for the scanning head is separated into three parts: the guided bundle, the mechanical break and the scanning head wires. Connected to the in-vacuum side of the feedthrough is a female MIL-C connector connected to a cable 89 cm long.

The cable contains two shielded bundles, each containing 4 twisted pairs. The wires driving the tube scanner are in their own shielded bundle, to prevent pickup by the sample bias during scanning. The sample bias shares a bundle with the coarse motors, which are inactive during imaging.

In order to avoid the cable twisting and interfering with the Viton cable as it is raised and lowered, it is rigidly mounted to an aluminum guide-rod. At the end of the rod is another female MIL-C connector fixed to the rod with an aluminum bracket (shown in Figure 2.18). In order to connect this rigidly mounted wiring to the scanning head, without communicating any vibration, there is a short run of wiring with very fine wires (38 gauge, Kapton insulated) in between the scanning head and the end of the rigidly mounted wiring. This is know as the **mechanical break** and has a MIL-C connector at either end, one male and one female. To reduce cross talk and radiative pickup without making the mechanical break too rigid, the wires for the tube scanner are a twisted pair, while the rest are kept as single conductor.

2.5.2 Crosstalk

The most critical wire for this microscope is connected to the tip. When operating as an STM, the current in the tip wire is amplified by 10^9 V/A in order to sense the minuscule tunnelling current. When being used as a coherent source of electrons, the current from the tip must be stable, to avoid spatial and energetic inhomogeneity.

In an early revision, the tip was not well shielded and isolated from the other channels. As a result, any voltage change driving the tube-scanner would induce a change in the tunnelling current. When acquiring an STM image, the tip is constantly in motion as it rasters back and forth. The feedback-loop is used to maintain a constant tunnelling current. Unfortunately, the voltage oscillation used to raster the tip induced a false signal in the tunnelling current, which was read by the feedback loop. For example, an oscillation in the X direction 1 nm in amplitude at a frequency of 1.4 kHz induced a 30 pA ripple in the tunnelling current. For reference, the current set-point for a typical STM image is 100 pA. This induced current made the feedback-loop incredibly unstable and rendered it

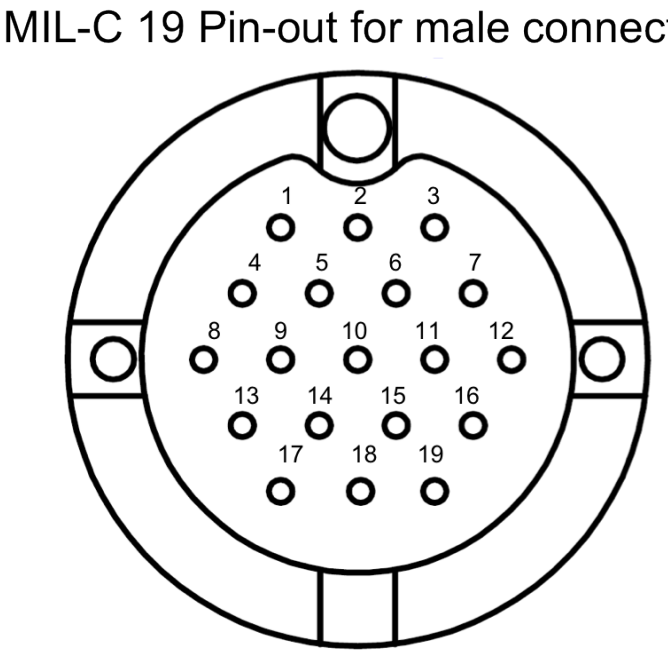

Figure 2.17: Pinout for the male end of a MIL-C 19 connector. Female connector is the mirror image.

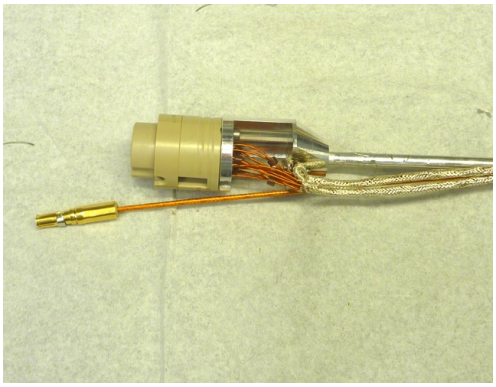

Figure 2.18: The connectors fixed to the bracket at the end of the guide rod. The MIL-C connector is beige and the coaxial connector is gold.

impossible to acquire good STM images, which in turn made it impossible to measure the noise level in the instrument.

Subsequently, the tip wire was completely rerouted to avoid crosstalk from the other channels in the system, and radiative pickup from the environment. Now, the tip current is carried by a coaxial cable for its entire run. To keep the signal well isolated from the rest of the electrical connections, it has its own coaxial BNC feedthrough. To avoid ground loops and provide more flexibility in grounding this circuit, the shield of the tip wire is isolated from the other grounds in the system.

In vacuum, the tip wire is installed in 2 sections: one section of semi-rigid, Kapton insulated coaxial cable which is mounted to the guide rod, along with the rest of the twisted pair. The second section is fine, soft, teflon insulated coaxial cable which is mounted directly to the tip and fixed to the body of the scanning head. This second section provides mechanical isolation from the semi-rigid cable.

The tip is further shielded by the electrical signals on the tube scanner by a grounded shield installed on the tip holder. This provides a ground plane between the tube scanner and the tip, attenuating the current induced in the tip from varying the voltage on the tube scanner.

After the tip wire retrofit, the crosstalk was benchmarked against the other STM systems in our group. The most noise-immune STM in our group is the STM1 system made by Omicron Nanotechnology GmbH. To measure crosstalk, the fine scanner was oscillated at a 200 nm amplitude in each axis, the frequency of the oscillation was swept from 10 to 1000 Hz and the induced current on the tip was read out at the corresponding frequency, using a software lock-in amplifier. This provides a direct measure of the current induced in the tip as a function of frequency. The data plotted in Figure 2.19 shows that the tip wire in the scanning head is actually better isolated than in the STM1.

2.5.3 Managing miscellaneous noise

There are other mechanical and electrical noises in the system that must be managed. There are various turbo-molecular pumps connected to the system; for the load-lock, the differential pumping on the rotary seal on the manipulator and a large pump for use during bakeout. Each of these pumps induces vibration in the scanning head at the frequency which they vibrate. Although the turbos must be used when pumping out the loadlock, or transferring tips and samples with the manipulator, they must be turned off before imaging in STM or LEEPS.

Another frustrating source of noise is the Attocube controller, ANC 150. When powered, the controller injects low-frequency broadband noise in the system, by physically shaking the scanner. It is thought that there is some ripple in the voltage that powers the piezos in the coarse motors that actually oscillates the tip. In order to eliminate this, the controller must be turned off when making sensitive measurements. Unfortunately, the coarse motor

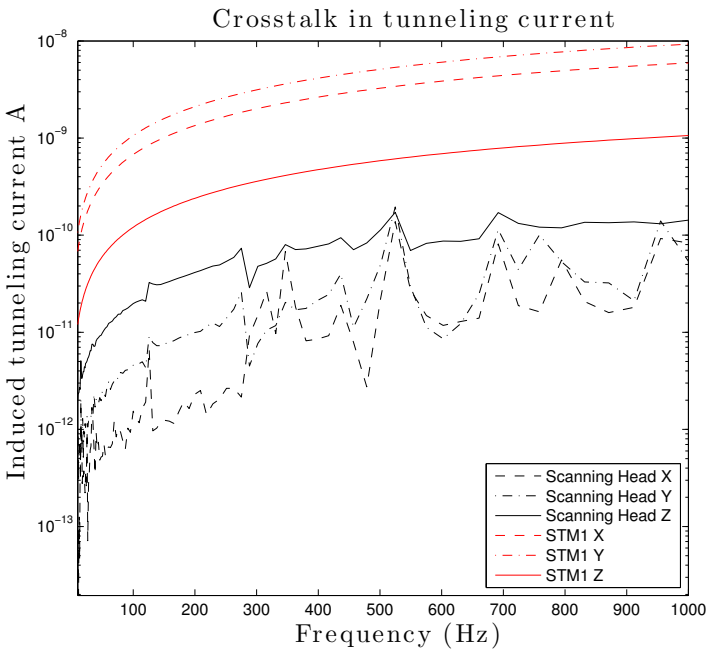

Figure 2.19: The current induced in the tunnelling signal by oscillating the fine scanner over a range of 200 nm. Comparison of the scanning head to the Omicron STM1.

must be used during the automatic approach of the STM tip. However, there is a setting on the Nanonis STM control software which forces the tube scanner to retract immediately once the tip has approached into tunnelling. After the tip has successfully approached and the scanner retracted, the Attocube controller must be turned off, before turning the feedback loop on to bring the tip back into tunnelling.

Also when navigating over the sample in LEEPS, the coarse motors must be used to find an appropriate region of interest. Again, the motors are used to navigate to this region, but then the fine scanner is retracted and the controller is turned off, before positioning the tip using the tube scanner in order to take the final image.

2.6 Maintenance

The subsequent section is meant to satisfy two purposes. First, it will instruct future users of the microscope on maintenance and repair. Second, by illustrating the inner workings of the microscope, this section is meant to show the reader explicitly many of the systems described in the preceding chapter.

2.6.1 Maintenance of the scanning head

To repair or replace parts of the scanning head it must removed from the UHV system for maintenance. Any time the UHV chamber is opened it must be baked. Before opening the

system, one must make sure that the ion pumps in the chamber being opened are closed to keep them as clean as possible. Also, one must isolate the chamber being opened. For example, if maintenance is only required on the main chamber, close the valve to the prep to ensure it is kept under UHV conditions. Obviously, when dealing with UHV parts always wear gloves and use clean tools. When reaching into the main chamber through the main window, longer gloves and a lab-coat must be worn so that the edges of the chamber aren't contaminated by bare forearms.

Before venting the main chamber to ambient pressure, the bellows on the main chamber must be supported. This is because while the main chamber is under vacuum, atmospheric pressure forces the bellows straight. The bellows itself behaves like a coil spring under compression and when it is not under vacuum it will bend. The bellows is most easily supported by a cardboard sleeve, fixed to it before venting the system.

To remove the scanning head from the main chamber, it is best accessed through the larger window on the main chamber. Once the window is removed, a sheet of UHV grade aluminum foil must be placed below the scanner to catch any items or debris that might fall and damage the fragile MCP below. To remove the scanning head, the first step is to disconnect the coax connector from the scanner to the wire guide. Hold both connectors firmly and gently pull them apart. Make sure the coax from the scanner is not twisted around any wires or cord, and let it hang from the scanning head. Next, the mechanical break must be disconnected from the scanning head and wire guide. Again gently but firmly, remove the connector from the top of the scanning head, then remove the other connector form the bottom of the wire guide. Carefully remove the mechanical break from the chamber, ensuring that none of the delicate wires are tangled to the Viton cord. Place the mechanical break on a clean tissue.

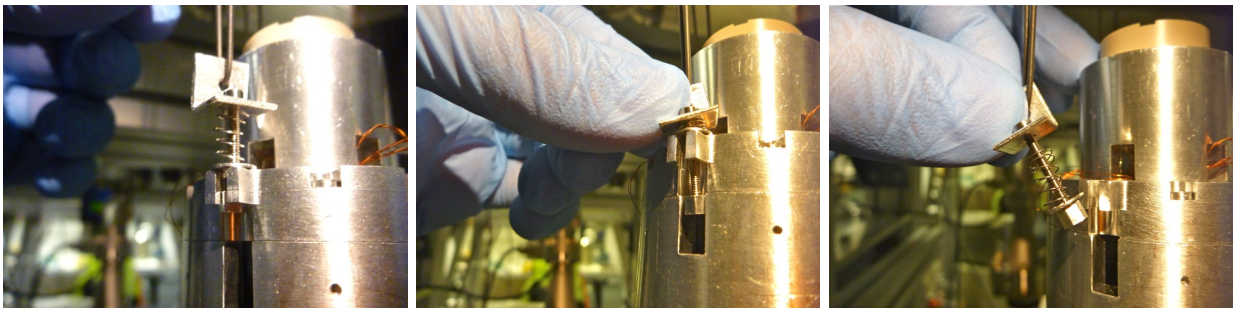

Figure 2.20: Removing the scanner from the spring-loaded hooks.

Next, remove the scanning head from the Viton cord. Hold the scanning head in one hand as you remove the cords, if the scanning head is unsupported during this process it will fall and may damage the MCP below or the scanning head itself. To unseat the spring loaded hooks, press down on the angle bracket holding the cord and slide it away from the scanning head (see Figure 2.20). Repeat this for all three brackets and remove the scanning head from the chamber.

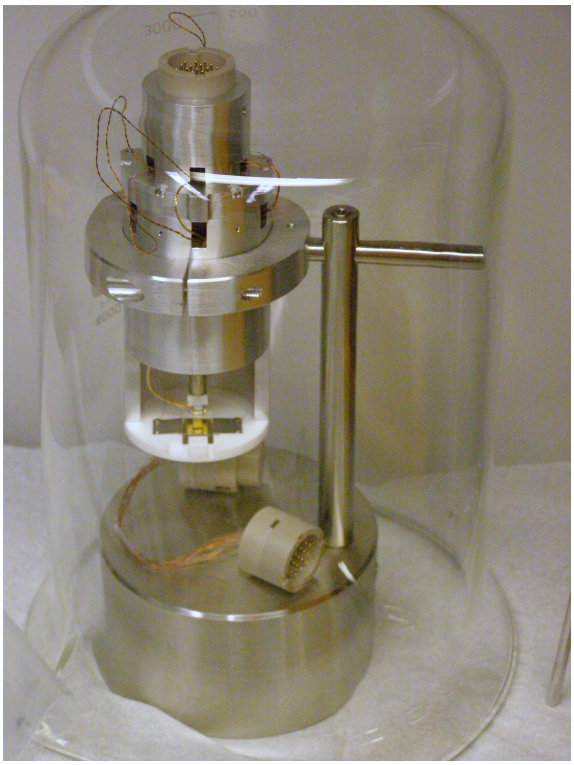

Figure 2.21: The scanning head loaded into the maintenance base. Mechanical break is at the bottom.

Once the scanning head is free, load it into the maintenance base pictured in Figure 2.21. Make sure the collar is sufficiently tight around the waist of the scanning head. The scanning head can be oriented in any way on the arm of the maintenance base. It can be fixed in any orientation by tightening the set-screws on the arms of the maintenance base.

The scanning head can be reinstalled by repeating the removal process in the exact reverse order. Between each step, ensure that the wires, cabling or cord do not interfere with one another. Also, the scanning head may need to be leveled once hung from the Viton cord again.

Once reinstalled, check for continuity between each channel on the breakout box and the items on the scanning head. The Attocube movers have no place to check continuity, to test proper connection: hook up the appropriate channel on Attocube controller box (ANC 150), to the breakout box with the coax on the connector labelled HI (e.g. channel 9 for Z) and place a grounding cap on the corresponding channel GND (e.g. channel 8 for Z). Switch the mode on the appropriate channel of the controller to CAP. If the motor is connected, the controller will read between 800-1000 nF for each channel. In order to check continuity to the electrode on the inside of the tube scanner, a lead has been wired between the inside of the tube scanner and the isolated gold connector on the body of the scanning head.

Once the scanning head has been reinstalled, and the connections tested, a tip and sample must be manually loaded into the scanning head. The best test sample is gold on

mica, as it has easily resolved steps 1 nm in height [28]. These samples have a finite shelf life and must be ordered periodically to ensure quality samples are available.

Once the maintenance is complete the chamber should be closed again and the scanning head should be tested in STM mode under rough vacuum, but never above 10^{-2} Torr since operation at this pressure may cause electrical shorts. The main chamber should be pumped by the roughing pump through the turbo pump. Once the system is under rough vacuum well below 10^{-2} Torr, the Attocube movers must be moved manually using the ANC150 controller. Typically, after exposing the scanning head to atmosphere the Attocube movers don't respond normally, or at all. Once the scanning head has been placed under rough vacuum again, it is necessary to increase the voltage applied to the movers to actuate them. Normally, 20 V is applied to the movers. If movers do not respond, use the ANC150 controller increase the voltage in 5 V steps and manually pulse the movers quickly forward and backwards for a fraction of a second. Do not use the single step mode. You may rarely have to increase the voltage all the way to 70 V, but carefully drive the movers at this voltage, as driving them for prolonged continuous times can damage the motors. Once they are set in motion, they should operate normally at 20-30 V until bakeout, when then will operate normally.

2.6.2 Maintenance of the wiring

Sometimes the in-vacuum wiring for the scanner has to be removed, either because a connection has broken or a channel has to be added to the cabling. In order to remove the cabling and the rod, the μmetal tube and MCP must be removed entirely. Unmount it from the 6" flange at the bottom of the spherical square and set it aside. Cover the tube in aluminum foil to prevent dust or other particulate from settling over the MCP. Make sure not to have the MCP in ambient pressure for more than a day, or else too much water will absorb in the fragile pores. This will damage the MCP. If the system is open for longer, fix a flange to the end of the tube and pump it down to a rough vacuum.

The cabling is fixed to the top flange, above the bellows. The coax and twisted pair come from separate feedthroughs and are mounted to the aluminum guide-rod some distance down its length. The first step in removing this wiring is to remove the coaxial feedthrough (shown in Figure 2.22a), and disconnect the coaxial cable from the feedthrough. Next the two 2-3/4" flanges on the opposite the coaxial feedthrough must be removed. Through the open 2-3/4" ports, use a long pair of needle nose pliers to remove the MIL-C connector from the feedthrough (shown in Figure 2.22b). Next, loosen the mounting bolt holding the guide rod to the top flange as shown in Figure 2.22c. While the guide rod is supported from below, unscrew the bolt supporting the guide rod (as shown in Figure 2.22d) and remove the entire wiring assembly from the bottom of the main chamber.

Once the cabling and guide are removed, place it on a clean surface. The cabling is fixed to the guide rod simply using twisted wire. As shown in Figure 2.23a, cut the ties

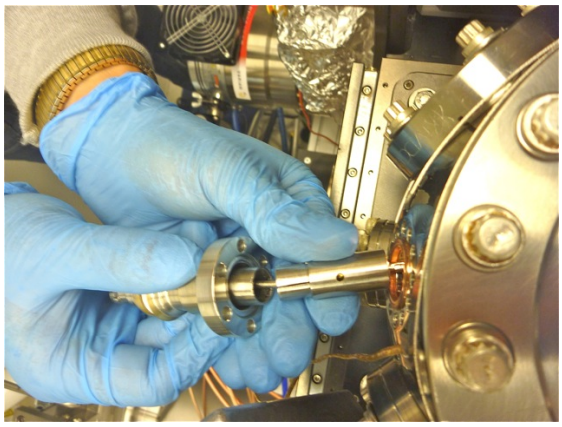

(a) Removing and disconnecting the coaxial feedthrough.

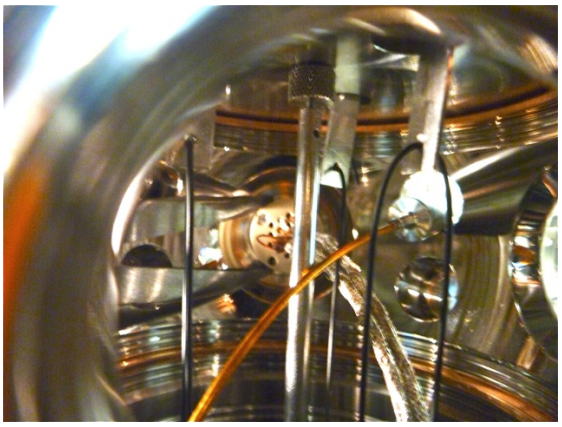

(b) Disconnecting the MIL-C connector from the feedthhrough.

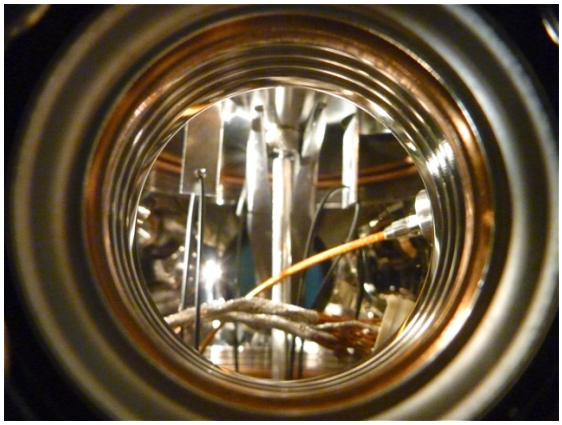

(c) Loosening the guide-rod mounting bolt.

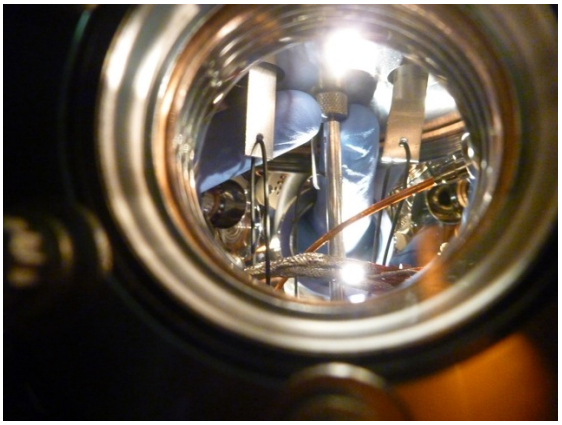

(d) Unscrewing the guide-rod mounting bolt.

Figure 2.22: Removing the wiring and guide from the top of the chamber.

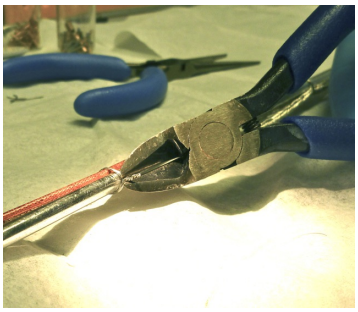

(a) Cut the twist ties.

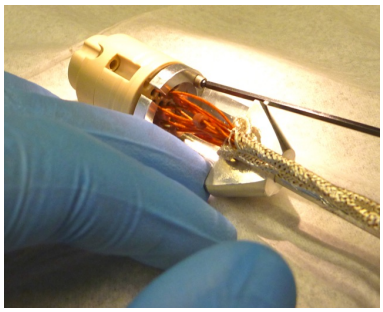

(b) Open the connector.

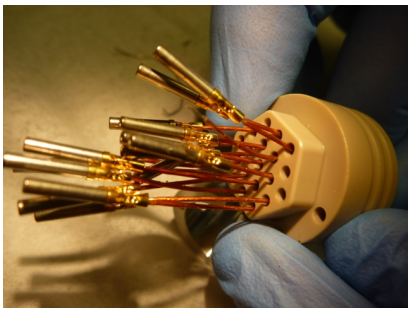

(c) Feed the wires through the connector.

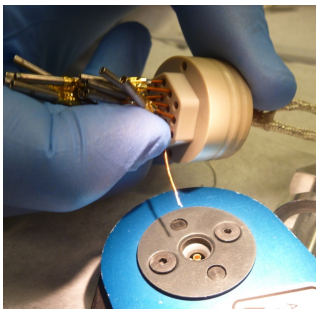

(d) Isolate the channel of interest.

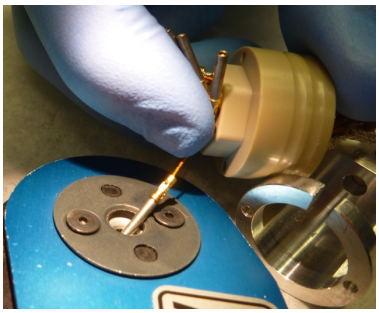

(e) Crimp the pin or socket the the channel.

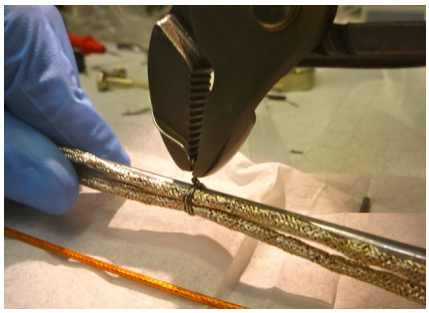

(f) Fix the cable to the guide rod.

Figure 2.23: Repairing and adding connections to the guide rod cables.

to free the cabling. Once the cabling is free, to access the connectors, to repair or add channels, the MIL-C connector must be opened. As shown in Figure 2.23b, this is done by unscrewing the two 2-56 screws in the body of the connector and carefully removing the cap from the connector. Individual pins and sockets are installed in the connector by feeding the wire through the appropriate hole in the connector and crimping on the pin or socket. The wires are similarly maintained in the scanning head and the mechanical break. Once the maintenance of the cabling is complete, the connectors are closed and remounted to the guide rod and the cabling is fixed to the rod with the twist-ties. All connections should be checked for electrical continuity between either end of the cable. Figure 2.23 c-f illustrate the process of crimping wire connections into the cable.

To reinstall the cabling and guide, first take a clean zip-tie and fix the connectors nearest to the mounting bolt to the guide rod, as shown in Figure 2.24a. Lift the guide rod up the bellows and manually tighten the mounting bolt to the top flange. The connectors will be easy to access since they are zip-tied to the guide rod. Grab the connectors, remove the zip tie (Figure 2.24b), and connect them to the appropriate feedthroughs, as shown in Figure 2.24c. Tighten the mounting bolt using the long needle-nosed pliers. Again, check for electrical continuity between the feedthroughs and the appropriate pins on the cable to make sure no connections broke during installation. Once the connections are checked, reinstall the scanning head and the mechanical break. Once all connections are checked

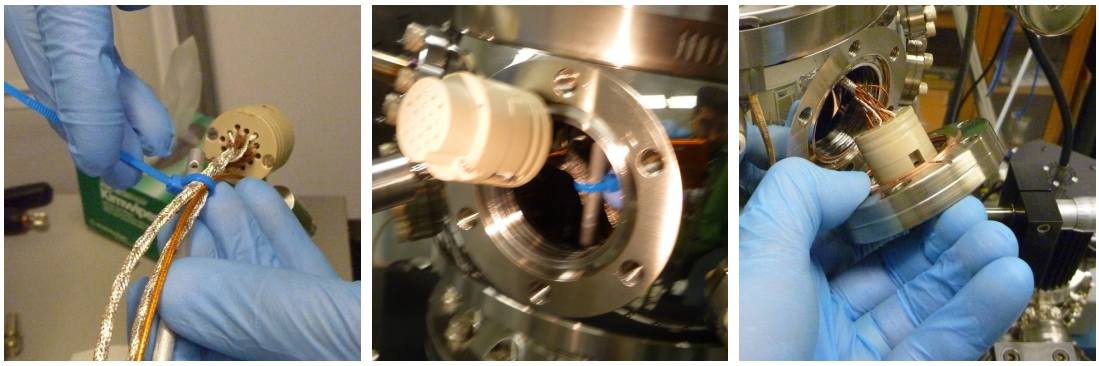

(a) Zip-tie the connectors to the end of the guide-rod.

(b) Grab the connectors and remove the zip-tie.

(c) Plug the connectors into the feedthroughs.

Figure 2.24: Reinstalling the guide rod cables.

between the feedthrough and the terminals on the scanning head, reinstall the μmetal tube and close the system.

2.6.3 Bakeout

In order to attain UHV pressures, the entire vacuum system must be elevated in temperature in order to desorb any volatile material, such as water and hydrocarbons, from the walls of the chamber. This procedure is colloquially known as 'bakeout.' In order to properly bake a system, the entire UHV chamber must be heated to between 120° and 150°C. This number is typically 150°C, but since the scanner hangs from Viton, a viscoelastic polymer, instead of metal springs, we take care to keep the bakeout temperature lower on the main chamber. This is to avoid heating the Viton beyond its working temperature, which would ruin its viscoelastic properties. As a results we typically bake the main chamber at 120°C for 3 days, instead of the more typical 150°C for 1 or 2 days. Despite this longer, cooler bake, we still manage a base pressure for the main chamber less than 1x10^{-10} Torr.

The typical bakeout procedure for the entire machine is as follows: the chamber is pumped out using the turbo-pumps, the ion-pumps are typically valved-off, and kept at UHV pressure before vacuum is broken. The load-lock is closed to the preparation chamber, and opened to the leak lines. The load-lock turbo is used only to pump the load-lock and the leak lines. The gate valve between the main and prep-chamber is opened, and the entire chamber is pumped through the large turbo in the main chamber. The pressure should be in the low 10^{-6} Torr range while being pumped out by the turbos before bake. The filament current on the ion gauges should be set to 0.1 mA.

The chamber must first be outfitted with many thermocouples. This is to ensure that the system is evenly heated. If parts of the system are too cold, they will not sufficiently outgas, and the system will not reach a low enough pressure. If parts are too hot, then they may be ruined: windows can crack, valves can leak, etc. K-type thermocouples, usually bare wires, are first tested in boiling water to ensure they read properly at elevated temperatures. The

thermocouples are then fixed to flanges on the chamber using ordinary metal hose clamps. The location of the thermocouple is labelled on the electrical connection. To record the temperature and pressure of the bake, 8 select thermocouples are connected to a multi-channel meter with a GBIP-interface that is read by custom made LabVIEW software that logs the temperature as the bake progresses. The analog-output of the ion-gauge is also connected to this meter to record the pressure.

Once the thermocouples are installed once, they are usually kept on the chamber. Next, the windows are wrapped in aluminum foil, this is to insulate the windows so that the temperature across the window doesn't rise or fall too quickly, which could crack the window, due to differential thermal expansion. The system is then wrapped in the custom-made insulated tent, and heaters are installed. The system uses 3 bakeout heaters placed in slots in the insulated tent and two radiative heaters placed beneath the prep chamber. The two lower bakeout heaters must be run at their highest temperature setpoint in order to sufficiently heat the lower parts of the chamber. The upper heater, near the top of the main chamber bellows is run cooler because the hot air from the rest of the chamber rises to the top of the bellows. The main chamber is heated to between 120-130°C to safeguard the Viton cord that the scanner hangs from. The prep and ion pumps can be heated to 150°C. The ion pumps have their own built-in heaters which are controlled using transformers (variacs). Each pump has 4 heaters, each with a cord and a standard 120 V three-prong plug. Each variac powers two heaters, for a total of 4 variacs for the two pumps. The ion pumps will reach 150°C when variacs are set at 50% power, however the thermocouples on the ion-pumps should be checked frequently to ensure the temperature doesn't overshoot.

Once the pressure has peaked and begun falling, the gate valves to the ion pumps are opened, and the ion pumps are turned on. This typically happens when the pressure is below $5\text{x}10^{-7}$ Torr. The current filament current is typically turned up at this time, to 1 mA. The working theory behind turning the ion-pumps on part way through the bake is that the bulk of the material volatilized during the first part of the bake can be removed from the system, through the turbo pump, without saturating the ion-pumps. Once the pressure reaches the mid 10^{-8} Torr range filament current on the ion-gauge is turned up to 10 mA.

Once the pressure has fallen near $3\text{x}10^{-8}$ Torr, the heaters are turned off, and with the chamber still hot the titanium sublimation pumps filaments are degassed. They are typically degassed in current increments of 5 A, from 10 A to 45 A and then finally at 48 A. The titanium sublimation pump filaments are degassed in series at the same current level, to allow each filament to cool before being degassed at the next current increment. For example with the current set at 15 A, filament 1 is degassed, then 2, then 3 and then 4. The current is then set at 20 A and each filament is then degassed again at that current. The filaments are never heated for more than 2 minutes at a time. There is an automatic degas feature on the controller, but it does not work. It will falsely report each filament

as broken, when it is perfectly functional. Each current set point and filament must be selected manually through the menu on the controller.

With the chamber still hot, after the titanium sublimation pump filaments are degassed, the ion gauges are then degassed. Once the pressure reaches the low 10^{-9} Torr range, the valve to the turbo pump is closed and the turbo is shut off. The temperature will continue to fall over the next day until the pressure typically reaches 1-2x10^{-10} Torr. The titanium sublimation pump filaments are fired at 48 A several times a day for the next few days, as the pressure falls below 1x10^{-10} Torr. The filaments are fired by running 48 A through a given filament and watching the pressure. The pressure will rise sharply before plateauing and falling slowly. Once the pressure stops falling, or begins to rise again, the current through the filament is shut off. The filament is never heated for more than 2 minutes or it may break.

The final item that needs to be degassed is the residual gas analyzer (RGA), which is a mass spectrometer used to measure partial pressure of gases present in the vacuum system. Once the chamber has cooled, the RGA head is installed and the "degas" feature on the RGA 3.0 software is run 30 times. This takes a rather long time as the routine takes about 2 minutes to complete, and must be selected manually each time.

Chapter 3

Low-energy electron point source microscopy

In LEEPS, the tip is brought very close to the sample, and a bias is applied between tip and sample. The bias draws electrons from the tip which are field emitted through the sample, towards a distant detector. This is shown schematically in Figure 3.1. The result is a magnified image of the sample on the screen. This microscope was built to perform LEEPS in as quiet and clean an environment possible, using the best electron source available. This chapter will discuss the process of preparing tips and samples used in the LEEPS experiment as well as the technique used to obtain images.

In order to use LEEPS to record holograms, the electron beam emanating from the tip must be sufficiently coherent. To obtain the most coherent beam, the tip must be crafted on the atom scale [29, 30, 31, 16]. The technique for constructing such tips, and the impact of the structure of the tip on imaging will be discussed in detail.

Sample preparation is also critical. It's difficult to prepare nano-scale objects to examine with low energy microscopy. Because of the low energies used, any contamination will obscure the sample. The easiest way to clean a sample in vacuum is to heat it, to desorb any contaminants. As a result, samples with nanoscale features, that can also withstand enough heating to desorb any contaminants, are required. Also, samples must be electrically conductive, since the sample must also serve as the anode in LEEPS.

3.1 Tip preparation

The development of techniques for creating tips that emit electrons from a single terminal atom have been ongoing since the first work by Fink in 1986 [32, 33]. Since then, many techniques have been explored for creating single-atom tips by building a sharp apex on the tip through field-assisted melting [34], or by depositing a thin film of noble metals which is then heated to form self assembled pyramids which act as single-atom emitters [35, 36, 37]. Recently, these tips have been shown to be completely coherent: the coherence angle of the beam is greater than or equal to the emission angle of the beam [29].

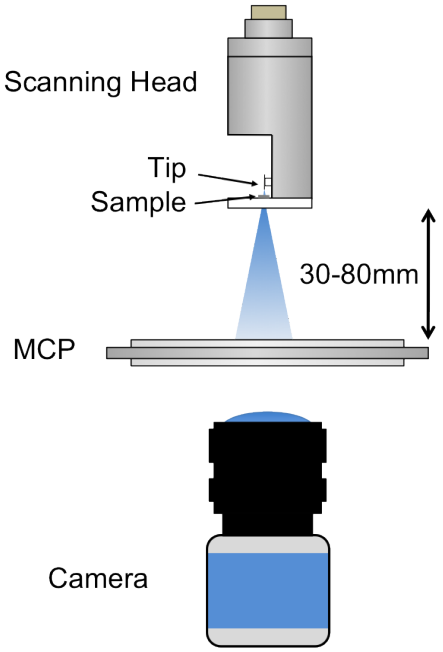

Figure 3.1: In the LEEPS experiment, the scanning head is lowered near the MCP. Electrons are projected from the tip, through the sample, towards the MCP. The resulting image on the MCP is acquired with a CCD camera.

Another method for creating ultra-sharp tips was reported in 2006 [38], using a field-assisted etch where material is removed from the shank of the tip, and etching is inhibited at the apex of the tip. This leaves a tip with a sharp apex with a higher aspect-ratio than those made by previous methods, which involved building a nano-structured apex on a relatively large tip [38, 39].

3.1.1 Field ion microscopy

To understand the etching process, it is first necessary to understand the technique of field ion microscopy (FIM). In 1951, Erwin Müller pioneered the technique of FIM [1, 40]. Using a very simple apparatus consisting of a sharp tungsten tip, biased in a glass vessel filled only with helium gas, at low pressure Müller and his grad student Kanwar Bahadur used FIM to obtain the first direct images of atoms [41].

To obtain an atomic resolution FIM image, a sharp piece of material (less than 50 nm radius of curvature) is biased with a high positive potential, typically 5-15 kV, in the presence of a dilute imaging gas (typically helium). In the high field near the apex of the material, imaging gas atoms are polarized and attracted to the apex (step 1 in Figure 3.2a). Once the atom is pulled towards the apex, it is ionized by the high field (step 2). The positive ion is instantly repelled from the apex and accelerated towards an MCP some distance away (step 3). The trajectories of the individual ions reflect the atom-scale structure of the apex of the tip. The result is that an atomic resolution image of the apex

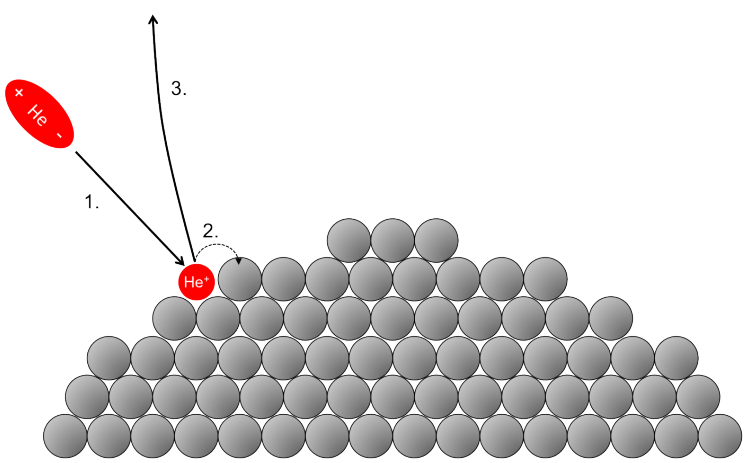

(a) FIM image formation process. 1. A helium atom is polarized by and attracted to the high-field surrounding the tip. 2. The high field causes an electron to tunnel from the helium atom to the tip, ionizing the helium atom. 3. The positively charged helium ion is repelled by the positively biased tip.

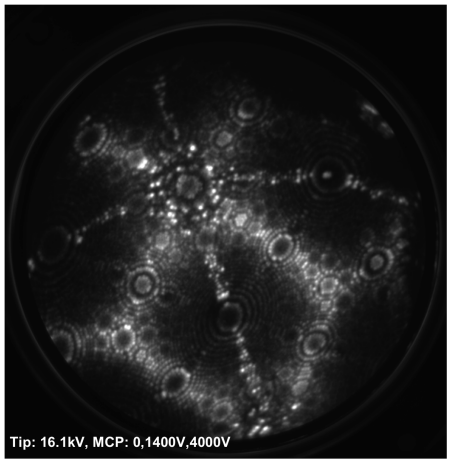

(b) An atomic resolution FIM image of a tungsten tip. Each bright spot corresponds to a tungsten atom.

Figure 3.2: Field ion microscopy.

is formed on the MCP. A typical image is shown in Figure 3.2b.

There is an apparatus for performing FIM located in the prep chamber illustrated in Figure 3.3a. The apparatus consists of an electrically isolated high-voltage (HV) tip holder, a MCP and a camera. The HV holder itself is a copper block mounted on two tubes. The tubes allow for liquid nitrogen (LN_2) to flow through the tip holder in order to cool the tip during imaging. The cooling decreases the diffusion of the imaging gas on the tip and results in a much sharper image on the screen. The tubes each have a section of ceramic isolator. This allows the tip holder to be biased at high-voltages, while being electrically isolated from the rest of the system.

The entire HV holder is mounted on a bellows, so that it can be inserted or retracted. In order to keep the HV holder out of the way of the pliers during normal tip and sample preparation, the HV holder is completely retracted. The holder is inserted partway in order to load a new tip. Once a tip is loaded, the bellows is fully inserted until the tip is less than a centimetre from the MCP.

In order to have the appropriate amounts of gases for FIM and etching, a gas handling system is installed on the prep chamber, illustrated schematically in Figure 3.3b. The gas handling system is used to leak a controlled background pressure of helium and nitrogen at pressures ranging from $1x10^{-8}$ to $2x10^{-5}$ Torr. In order to leak such precise amounts, a sapphire leak valve is used for each gas. Each gas is stored in a compressed cylinder nearby and connected to the leak valve through a 1/4" stainless steel tube through a series of valves.

When leaking a controlled amount of either gas into the chamber, the valves must start closed. Valve 1 (in Figure 3.3b) is opened and the regulator is used to adjust the pressure

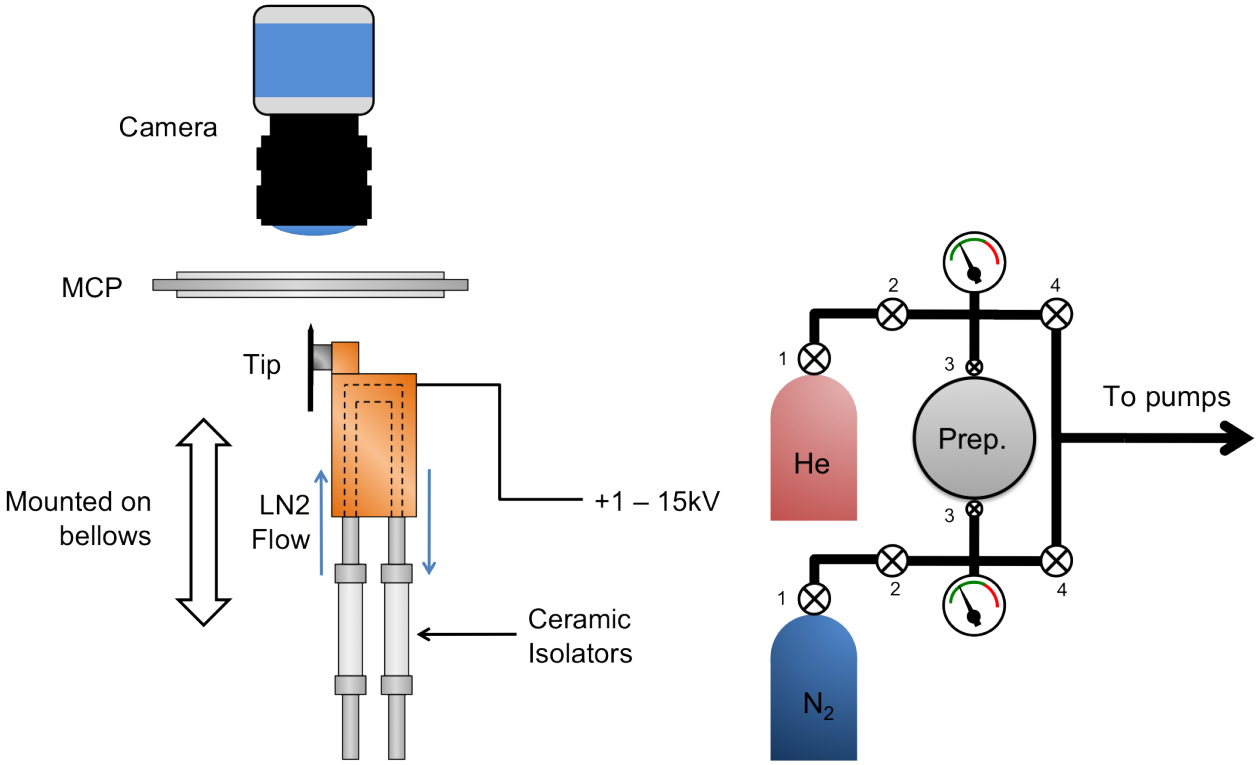

(a) The FIM setup.

(b) The gas handling system for leaking gases for FIM and etch.

Figure 3.3: The FIM setup and gas manifold.

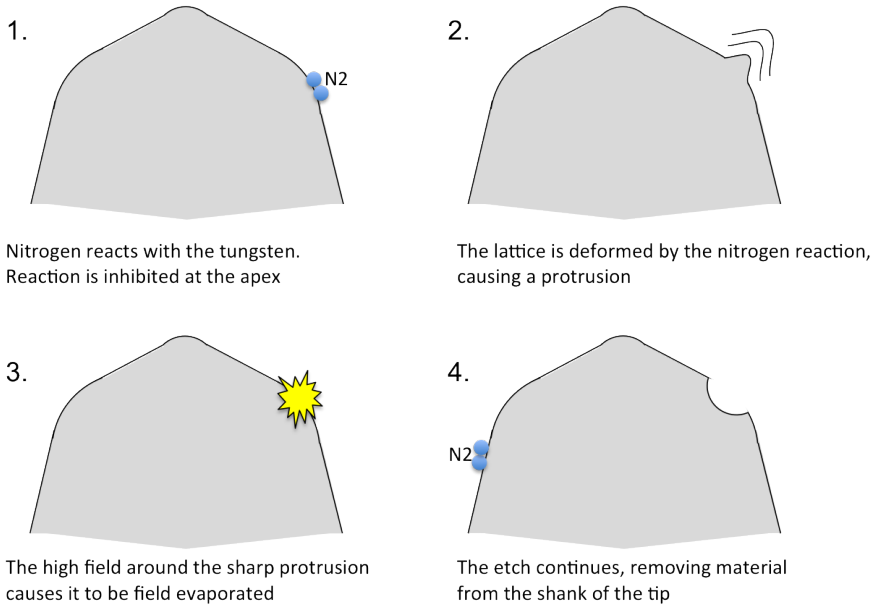

Figure 3.4: The field-assisted etch process.

in the line. Typically, 1 atm is sufficient pressure for the leak lines. Next valve 2 is opened to fill the line with gas up to the leak valve. With the RGA reading the relative pressure of the gas being leaked, the corresponding leak valve is carefully opened (valve 3). Once the desired partial pressure is reached, the experiment is carried out.

To ensure the leak lines are clean, they must be evacuated after each use. To do this, the open leak valves and valve 1 at each tank must be closed. The pumping line to the roughing pump must be opened and valve 4 is carefully opened. Once pressure on the appropriate gauge falls below 0.1 Torr, the line can be pumped with the turbo, until the gauge reaches its lower limit.

The field-assisted etch technique [38] employed in our system creates a nano-tip by preferentially removing atoms from the shank of the tip. Under FIM conditions, a partial pressure of nitrogen gas is leaked into the system. Some of the nitrogen reacts with the tungsten at the surface of the tip, causing a small protrusion. The field at this protrusion is instantaneously high enough to field-evaporate - i.e. to remove the material. The high fields used in FIM inhibit the nitrogen from adsorbing at the apex, which allows field-induced evaporation to occur preferentially at the shank of the tip, while safeguarding the apex of the tip. This process is illustrated in Figure 3.4.

By controlling the parameters during the field-assisted etch, tips with different aspect ratios can be produced [39, 42, 43, 44]. The etch parameters that can be tuned are partial pressure of nitrogen and tip voltage. Varying the nitrogen partial pressure changes the etch rate, since there are more nitrogen molecules present to react with the tungsten, material will be moved away more quickly. The tip voltage controls two factors: the area which is exposed to the nitrogen etch and the rate of field evaporation from the apex. A higher

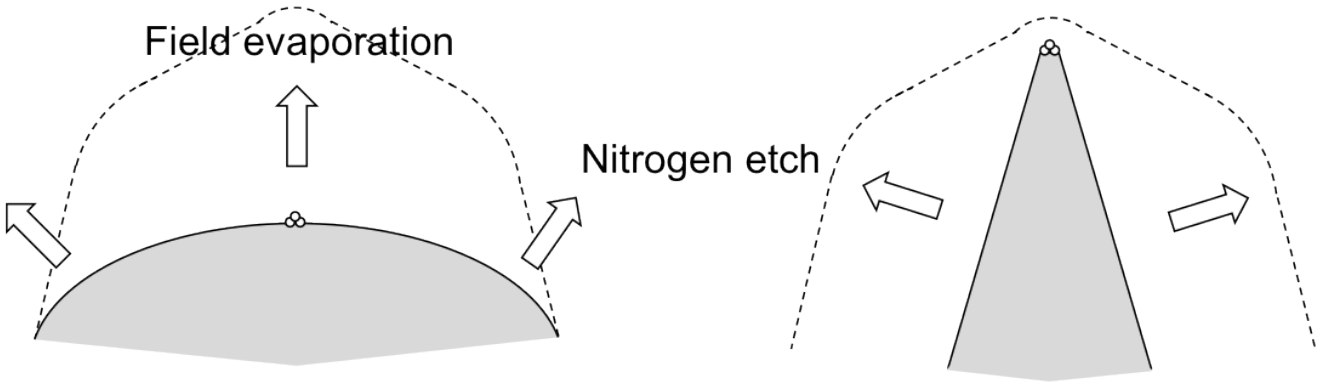

Figure 3.5: Crafting tips with different aspect ratios by tailoring the etch process. Material from the tip is removed by two competing mechanisms: nitrogen etching and field evaporation. Nitrogen etching predominantly etches the shank of the tip. Field evaporation removes material from the apex. Tips with different aspect ratios can be created by controlling these relative rates.

voltage will result in a higher field over a greater area of the apex, inhibiting the etch over a larger area. A high field causes W atoms to be field evaporated from the tip, even in the absence of nitrogen. A higher voltage results in a higher field at the apex, if that field is high enough material will constantly be field-evaporating from the apex of that tip. As the etch proceeds, the apex becomes sharper, which naturally increases the field at the apex for a given voltage. In order to maintain the same field at the apex, the voltage must be dropped over the course of the etch.

If the etch is carried out at higher voltages, the field-evaporation from the apex will be competitive with the etch at the shank of the tip. What results is a tip with a low aspect-ratio, essentially a single-atom tip sitting on a broad base.

If the tip voltage is kept below the field-evaporation threshold during the etch, the apex of the tip will be protected and material will continually removed from the shank of the tip. As a result, a tip with a high aspect-ratio will remain. These two extremes are illustrated in Figure 3.5.

3.1.2 Electrochemical etch

To etch a tip to a single atom, a tip sharp enough to be imaged in FIM is required. This can be accomplished readily by electrochemically etching a tungsten tip in NaOH [45] in an electrochemical etching station, like one illustrated in Figure 3.6. The station consists of a shallow dish filled with NaOH. Submerged in the dish is an anode connected to the negative terminal of a power supply. A tungsten wire is connected to the positive terminal and is partially submerged in the solution. When a bias is placed across the terminals, tungsten is etched away preferentially at the meniscus of the solution creating a cusp shape to the wire. Eventually the wire will break at the meniscus. The power supply is designed to detect the fall in current that accompanies the break of the wire and shuts off the voltage, and stops

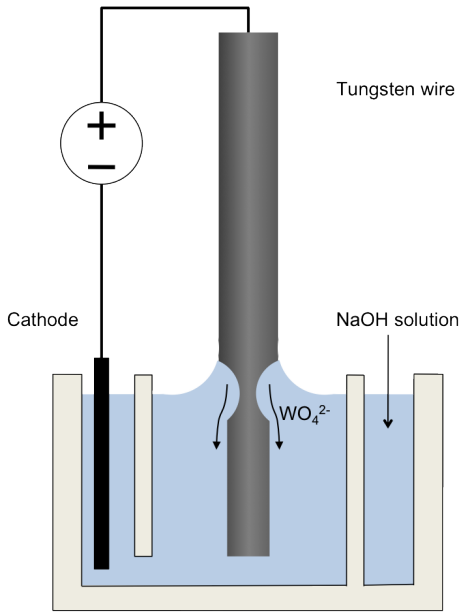

Figure 3.6: A schematic of the station used for electrochemical etch.

the etch. What remains of the wire at the meniscus is a very sharp tip, usually with less than a 50 nm radius of curvature.

To produce a sharp tip reliably, the following procedure is used. First, a 20 mm segment of 125 μm diameter polycrystalline tungsten wire is wiped clean using an isopropanol soaked tissue. The wire is inserted about 5 mm deep into a 2 molar solution of NaOH and the power supply is turned on for 10 seconds. The tip is quickly removed from the solution. This quick etch removes the outer layer of tungsten from the wire, leaving a clean segment to continue etching. The wire is rinsed in clean water before being reinstalled in the etching station. Once reinstalled in the etching station, the tip is re-inserted about 3 mm into the solution and the power supply is turned on. This time the supply is kept on until it switches off automatically upon the break of the wire. This usually takes 10 minutes. Once the etch is complete, the tip is removed and cut to a length between 13 and 14 mm before being inspected under an optical microscope. If the tip appears to be smooth and straight under 10x magnification it is kept, otherwise it is discarded. Using this procedure, tips with a radius of curvature below 50 nm are etched with nearly 100% yield.

3.1.3 In-vacuum preparation

Once the tip is electrochemically etched and cut to size, it is loaded into the prep chamber via the load-lock. In preparation for the in-vacuum etch, the load-lock and the leak lines should be pumped out for several hours. The tip is then picked up with the pliers and brought into view of an optical pyrometer. The pyrometer is used to read the temperature of the tip during cleaning by an in-vacuum anneal. To heat the tip, the pliers are loosened and a current is run through the tip. If the grip of the pliers on the tip is too tight, the

jaws will sink heat away from the tip and excessive current is required to heat the tip. The goal is to heat the tip to 700°C for 2 minutes. This should take between 2-5 A of current. If more current is being run through the tip and it is not heating up, the pliers are probably sinking away heat and should be carefully opened further.

Once the tip has been cleaned, it must be loaded into the high-voltage (HV) holder. The HV holder must be raised until it can be seen through the camera on the 2-3/4" window directly above the load-lock. With the pliers tightly closed, carefully load the tip into the HV holder using the pliers. To avoid damaging the HV holder, when the pliers are within a few centimetres of the HV holder operate the pliers only in 'slow' mode. Once the tip is loaded in the HV holder, open and retract the pliers fully and raise the HV holder to its limit.

Next, the RGA should be turned on and degassed a few times. Make sure the valve pumping out the leak lines is closed. The gate valve to the load-lock should then be opened the pressure in the prep should not exceed $5\text{x}10^{-9}$ Torr. The gate valve to the ion pump should be closed and the ion gauge be shut off. The MCP should then be turned on, typical voltages used for FIM are -1600 V, GND and +2000 V on the MCP front, back and phosphor, respectively.

The widest electron beam will produce the highest resolution image. Recalling Figure 1.7 and simulations in [15], a tip with the highest aspect-ratio possible is needed. The field-assisted etch can be used to tailor that aspect ratio. A typical recipe for etching the tip is as follows: while flowing LN_2 through the HV holder, a background pressure of $1\text{x}10^{-5}$ Torr of helium imaging-gas is leaked into the chamber. A bias between 10-20 kV is placed between tip and MCP (depending on the radius of curvature) until a clean, stable FIM image of the tip can be obtained. A background pressure of $2\text{x}10^{-6}$ Torr of nitrogen is then leaked into the chamber, and the tip bias is held constant for 45 minutes. This 'pre-etch' allows the material along the shank of the tip outside of the FIM image to be etched away. The voltage is then decreased automatically at a rate of 1 V/s at a constant pressure of N_2, until the bias reaches 5.5 kV. This is to ensure that material is not field-evaporated from the apex as it is etched away from the shank of the tip. At this point the voltage is lowered in 100 V increments at 1 V/s. When the voltage has reached 5 kV, the N_2 pressure is lowered to $8\text{x}10^{-7}$ Torr and the voltage is lowered in 10 V increments until the tip is sufficiently sharp. The etch is halted, by stopping N_2 flow, when a sufficiently sharp tip is obtained. Using this method tips ending in a single atom can be routinely produced. A typical etch is shown in Figure 3.7.

A single atom tip is not always required. For example when using a tip for STM, the tip is still imaged in FIM. Typically, the tip is annealed and placed in the HV holder. The MCP voltages and helium gas pressures as above are used, but no nitrogen. The voltage on the tip is raised until an FIM pattern in visible on the screen. The voltage is then slowly raised at a rate of 10 V/s, until a broad portion of the tip is visible in FIM. By visualizing

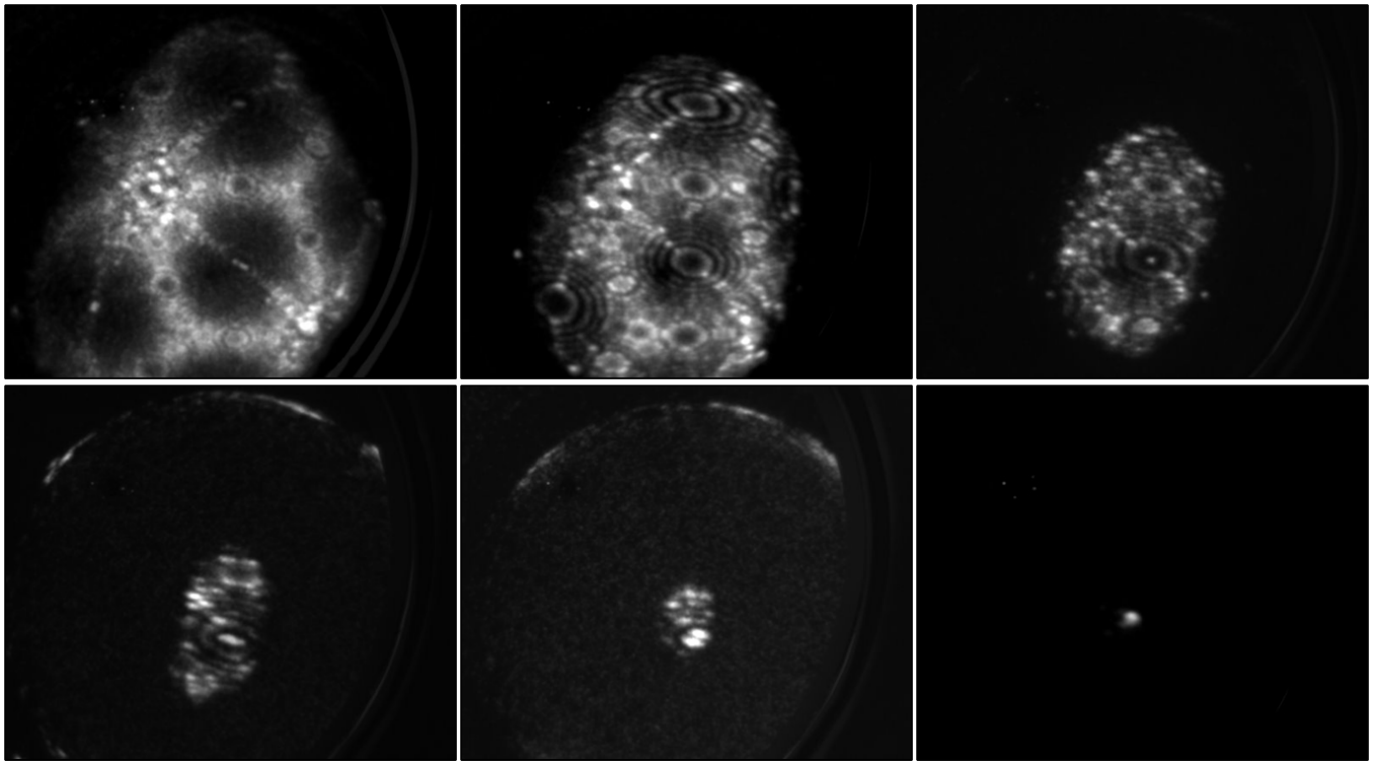

Figure 3.7: FIM images of a tungsten tip being etched to a single atom.

the tip in FIM, contaminants are being field evaporated from the tip. This leaves a clean metal surface for STM. Every tip is subject to FIM before STM and LEEPS. This helps with the repeatability of each technique.

Once the flux of helium and nitrogen is closed, the MCP is turned off, the ion pump is reopened and the pressure is allowed to recover. Only after the pressure in the main chamber has returned to the 10^{-10} Torr range is the tip unloaded from the HV holder and then loaded into the scanning head, using the pliers.

3.2 Sample subtrate

The substrate of choice for examining samples in LEEPS is a silicon nitride window perforated with a regular array of round holes. The silicon nitride (SiN) membrane is 50 nm thick and the holes are 2 μm spaced on a 4 μm pitch. The substrates are sold by Structure Probe Inc. [46]. The grid is shown in Figure 3.8.

The SiN windows are used for a variety of reasons, primarily because they are very clean and outgas a good deal less than TEM grids made of amorphous carbon. Outgassing is a critical problem, because the tip is held so close to the sample, and outgassing near the tip can damage it irretrievably. Another benefit of these grids is their high tolerance to heat. They can be annealed to temperatures exceeding 1000°C, which allows them to be cleaned thoroughly. The windows are supported by a silicon frame, 200 μm thick, which

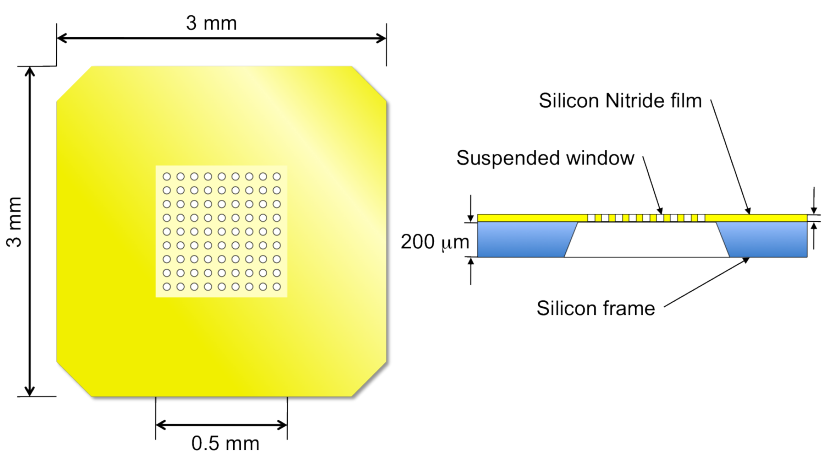

(a) A diagram of an SiN window with a regular array of holes.

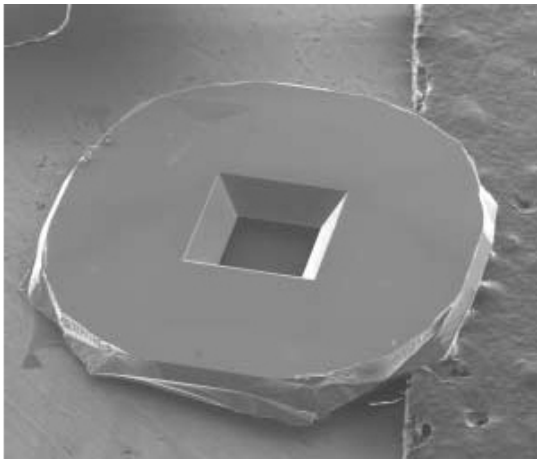

(b) An SEM image of an SiN grid. The frame is etched away to a suspended SiN membrane.

Figure 3.8: A diagram of the construction of a SiN grid as well as and SEM image. (b) taken from http://www.2spi.com

makes them relatively robust and easy to handle. However, great care must be taken to avoid dropping them face down, as the window has a tendency to stick and tear.

Silicon nitride is chemically compatible with a wide array of solvents, which is useful because many samples are suspended on the windows by placing a small droplet of nanoparticles suspended in solvent. This allows for a wide variety of samples, suspended in a wide variety of solvents, to be cast on the windows without dissolving the window.

Another benefit of the SiN windows is that they are designed primarily as substrates for SEM and TEM, which allows us to easily load the samples into other electron microscopes to examine the quality of the samples before imaging them in LEEPS. It is always useful to use many microscopy techniques in conjunction with one-another, especially when developing a new technique, so as to have multiple methods for determining structure and contrast.

As previously mentioned, since samples have to serve as both anode and substrate, it must be conductive. Unfortunately, SiN is an insulator. To make them conductive, the grids are first sputter-coated with 45 nm of gold atop a 5 nm chromium adhesion layer.

Once samples have been prepared by suspending them on the SiN windows, they need to be loaded into UHV. First, the 3x3 mm SiN grids must be loaded into an adapter, which will allow them to be handled by the UHV pliers. Specific adapters were cut from 125 μm thick tantalum sheets. Tantalum was chosen because of its high melting point (3017°C), machine ability, overall UHV compatibility and lack of nickel which causes contamination. The adapter is essentially a winged slot, which holds the window while giving something for the pliers to hold onto. An adapter, loaded with an SiN window is pictured in Figure 3.9. The adapters are reusable.

After being loaded in the adapter, it is placed in the tray in the load-lock which is then pumped out using the turbo for at least 20 minutes. The load-lock is opened to the prep

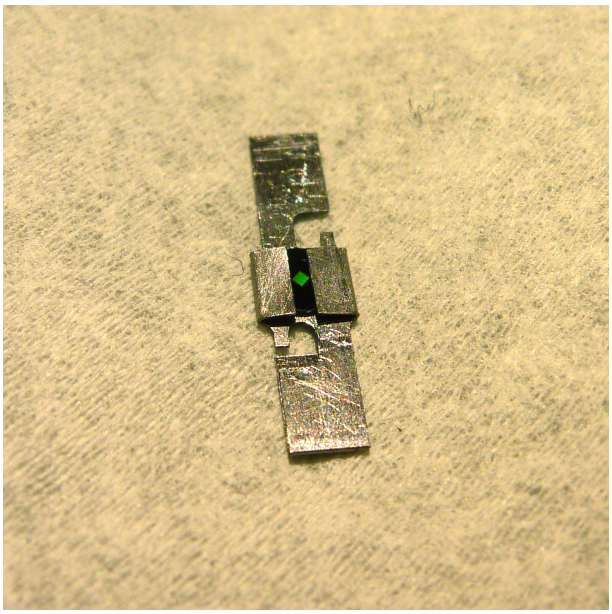

Figure 3.9: The SiN window in a tantalum sample holder.

chamber and the tray is slid in. The pliers can then pick up the adapter. Once in the pliers, the adapter is heated within view of the pyrometer. Depending on the sample, the SiN window is heated at some temperature above 250°C. Once properly cleaned, the sample is loaded into the scanning head.

3.3 Acquiring images in LEEPS

Once a clean sample and appropriate tip are loaded in the scanning head, the tip must be moved over the window. This is most easily done in a few steps. First, mount the camera so that it is viewing the scanning head through the 6" CF window. Focus the camera on the sample and with the coarse motors, move the tip in the Y-direction (axis 2 on the ANC150), until the tip is lined up over the window. The tip does not need to be approached close to the window, as it will field emit electrons when many millimetres away. It is in fact better to the have the tip far away at this stage, as there is less chance of the tip crashing into the sample. Also, it is easier to align the image with the tip farther away, because magnification factor is lower and the image encompasses a larger field of view. Next, move the camera back to the 2-3/4" viewport for an isometric view of the scanner. Try and align the tip over the window in the X-direction (axis 3 on the ANC 150).

Open the following software applications: the Nanonis controller, the LabVIEW applications for camera and Keithley 237 source meter control. Set the current limit on the source-meter to 2 nA. Make sure that the piezo gains are set to '1' for x,y and z on the Nanonis HV amplifier. Make sure the gains are the same in the Nanonis software and that the piezo is fully retracted in the z-direction.

With the tip appropriately positioned, lower the scanning head to the '3' mark on the bellows. At this mark, the bottom of the scanner is 8cm away from the face of the MCP. Train the camera on the MCP at the base of the μmetal tube. Turn on the camera control software. Next, power the MCP at the base of the μmetal tube. Typically, the MCP is operated at rather low gains, since the electron flux is high and the lower the gain, the smaller the pixel size on the MCP. Increase the MCP voltages slowly, all the while paying attention to the pressure in the main chamber, which should stay steady. Set the MCP voltages to (GND, +1600 V, +3300 V). There should be a few bright-spot defects on the MCP. Use those to focus the camera on the MCP.

Next, make sure the Keithley 237 source-meter is connected to the tip feedthrough. Using LabVIEW program for controlling the voltage, slowly ramp the voltage from 0 V to -100 V, looking for electron emission on the MCP and checking the current on the source meter. When there is no emission, the source meter should read less than 10 pA if everything is properly connected. If the meter is reading a higher current, check all connections. Otherwise, keep raising the voltage until the electron emission is seen on the detector. This should happen between -300 and -500 V. If the perforated grid pattern is visible on the detector as in Figure 3.10a, proceed with aligning the beam. The aligned beam should appear as in Figure 3.10b.

LEEPS is a transmission microscopy technique, the more electrons being transmitted through a portion of that sample, the brighter it appears. If the system is behaving properly and the tip is aligned above the grid, an array of bright spots will appear on the screen. Each bright spot corresponds to a hole in the perforated window. The SiN membrane itself totally absorbs electrons at the energies used in LEEPS and as a result is completely opaque. Each hole is 2 μm in diameter.

If electron emission is seen on the MCP, with no discernible image, the tip is probably not properly aligned over the perforated window. Only diffuse electrons scattered by the sample holder are visible on the MCP. In this case, the image will resemble Figure 3.10c. Because the tip was visually aligned over the window in the X-direction before lowering the scanner, to find the window, using coarse motor control in the Nanonis software, step in the Y-direction. Move the tip 100 steps at a time, from 0 to +1000, then back to -1000. If no grid is visible then expand the search. If no grid is visible after searching between -3000 to +3000 steps, repeat the search after moving the tip to $\pm$500 in the X-direction. If the grid remains lost, lift the scanner into the loading position and reposition the tip over the window using the camera.

Once an image of the grid is present on the screen, the beam must be aligned so that it is centred on the MCP. This is done by adjusting the micrometer screws on the top stage of the bellows. The scanner may have to be lowered further to the '4' mark, so that the entire spot is within the screen. Otherwise, it is impossible to align. Unfortunately, adjusting the micrometer screws will set the scanner swinging. Take care not to adjust the voltage or

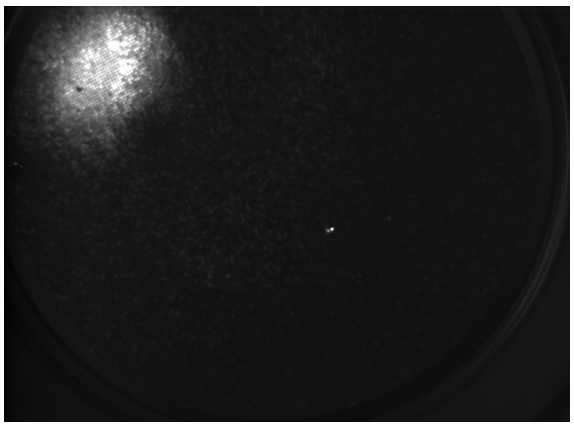

(a) Electron pattern emission with grid visible.

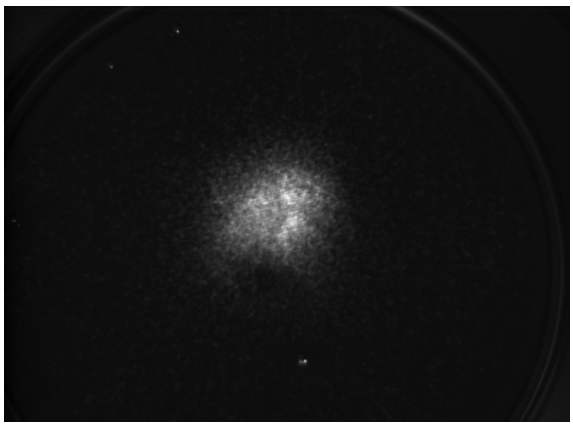

(b) Pattern with the emission spot centred.

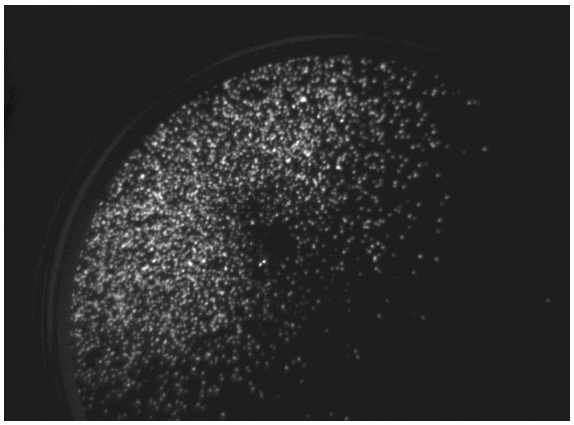

(c) Diffuse electron emission when tip is not positioned above grid.

Figure 3.10: Initial electron emission from tip: pattern appears diffuse when tip is not positioned over the grid. Once the grid is visible on the screen, it must be centred.

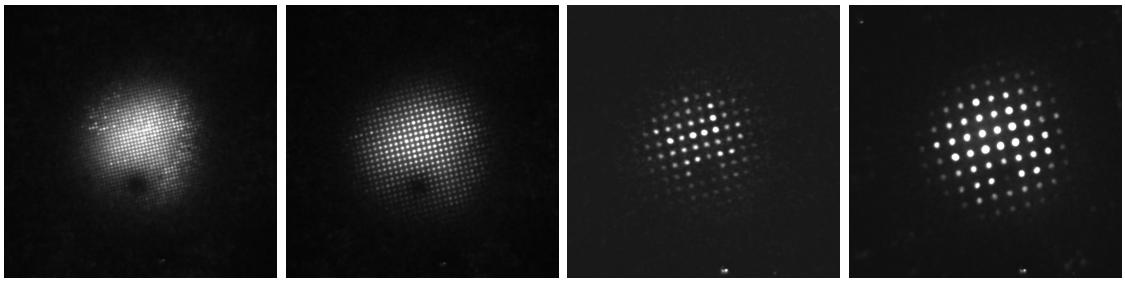

Figure 3.11: Increasing the magnification of the image as the tip approaches the sample.

move the tip while the scanner is swinging. The motion should damp out in a few minutes.

Next, approach tip 10 steps at a time, paying close attention to how much the magnification factor changes during each set of ten steps. Also, pay attention to the current being drawn from the tip, and keep it below 0.1 nA. Periodically, stop approaching, increase the current and save an image. Once the magnification factor of the image starts noticeably changing for each set of 10 steps, and reduce the interval to 5 step intervals. Continue approaching with only the coarse motors until the image contains only 2 or 3 grid-holes. Images of the grid as the tip approaches are shown in Figure 3.11.

Once the tip is so close that only a few grid-holes are visible, the tip must be approached more slowly. If the tip is brought closer to the sample by a significant fraction of its distance, then the field around the tip will increase too quickly, drawing too much current and damaging the tip. To carefully approach: while watching the current from the tip and the image on the MCP, slowly extend the z-axis of the tube scanner using the Nanonis controller. If the emission current increases above 0.1 nA or the image on the screen becomes very bright and defined, slop extending the current and lower the voltage. If the emission current is below 0.1 nA with the tip fully extended, retract the tip and then approach 2 steps at a time with the coarse motor. Continue this until the magnification increases a great deal while extending the fine scanner, then do the same process, but only extend the tip by half the range and take 1 coarse step. Continue until the desired magnification is reached.

Periodically, an image should be acquired during the approach with the same landmark over several images with different magnifications. This is done so as to have a good idea of the relative tip-sample distances during each image. To acquire an image, hold the tip steady and slowly increase the current to 0.25 nA. If the current is unstable at 0.25 nA, increase the voltage until the current hits the limit of 2 nA. The current will flicker for a short time but will ultimately settle. Reduce the current to 0.25 nA and the current should be more stable. Also, pay attention to the shape of the emission pattern. If bright lobes are flickering in the image, the current will be unstable. It is thought that these flickering lobes are field-emission from sites where contamination is absorbed on the tip. Pulsing the voltage to the current limit desorbs this contamination, causing more stable emission. Make sure to turn the Attocube movers off before acquiring an image, as noise induced by the controller will blur the image.

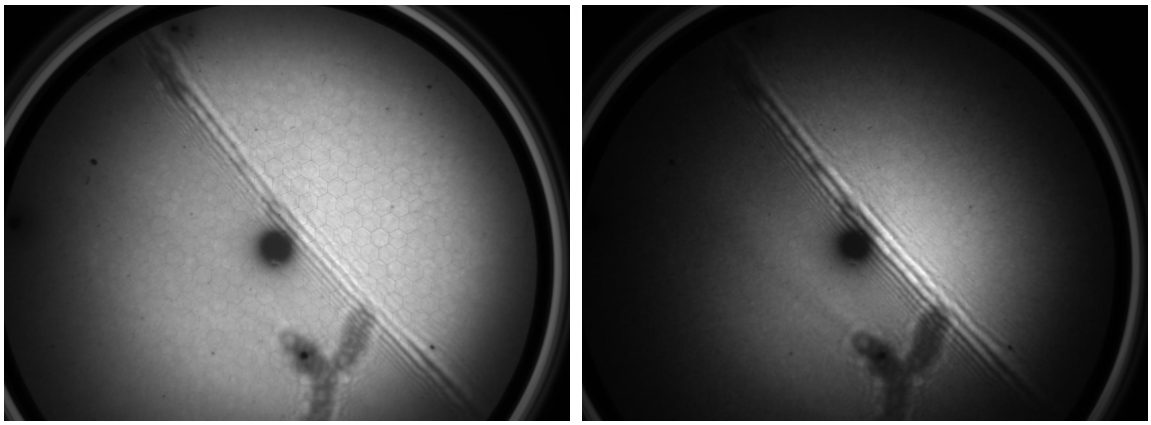

(a) An image taken at 1.6 nA emission current.

(b) An image taken at 0.29 nA.

Figure 3.12: The effect of emission current on imaging. Care must be taken to ensure that images are not being over-exposed (or clipped).

Increasing the emission current may saturate the MCP, and the MCP voltage may have to be reduced to lower the gain. Take care to make sure the dynamic range of the camera is being used properly. Make sure there are no portions where the image is being saturated and features are lost because the data is clipped. Image processing and alignment will be covered in Chapter 6. The effect of emission current on imaging is seen in Figure 3.12.

Also, before acquiring a dataset for a given tip, it is necessary to take a reference image. The reference image is taken when the tip is centred over an area with nothing in between the tip and detector; it is essentially an image of the field-emission from the tip. The reference image is later used to correct images for the non-uniformity in the tip emission and for defects and the native hexagonal pattern in the MCP. Take care to acquire images at the same emission current for the entire dataset as well as the reference, this will simplify the correction of the data later on.

It must be stressed, that the closer the tip, the more careful the user must be in navigating the tip. When the tip is close, the field changes drastically. By moving the tip too quickly, too much current will be drawn from the tip causing the emission area to heat up rapidly, destroying the tip. To prevent this, use very low voltages when moving the tip, either laterally or approaching the sample, as this will keep the field near the tip low. Use a voltage where a recognizable image barely forms, allowing the tip to be navigated relative to the sample. Only increase the voltage to the desired imaging current once the appropriate area is found and the tip is held static. Moreover, after moving the piezo there is some natural creep. This can take minutes to subside, depending on the amount the tip was moved. This will cause drift in the image which may have to be corrected later.

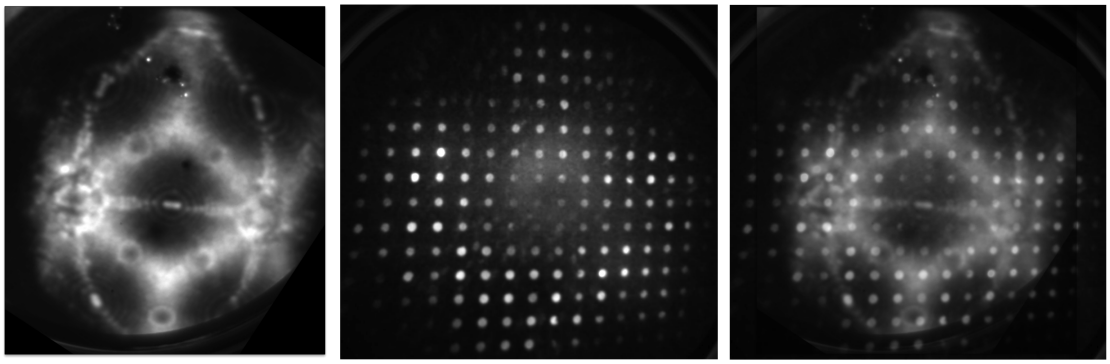

(a) The atomic structure of an extended tip as seen in FIM.

(b) A LEEPS image of the SiN grid with the same tip.

(c) The tip image overlaid on the LEEPS pattern.

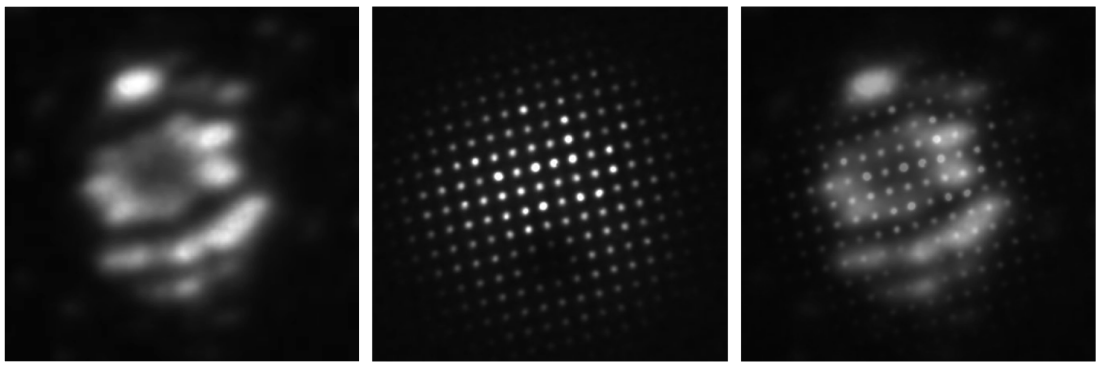

(d) The atomic structure of a few atom tip as seen in FIM.

(e) A LEEPS image of the SiN grid with the same tip.

(f) The tip image overlaid on the LEEPS pattern.

Figure 3.13: The effect of the tip structure of the LEEPS image. Tips with a larger radius of curvature act like an extended source limiting coherence.

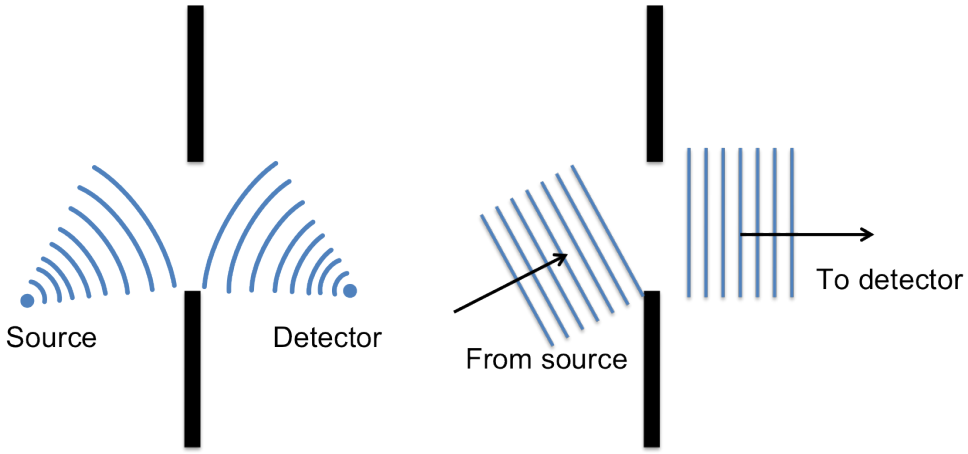

(a) Fresnel diffraction.

(b) Fraunhofer diffraction.

Figure 3.14: Diffraction by an aperture in the near field (Fresnel) and far field (Fraunhofer) limits.

3.4 Effect of tip shape on LEEPS imaging

The structure of the tip has a drastic effect on imaging. This effect is shown in Figure 3.13. The LEEPS image is an image of the sample convolved with a field emission image of the tip. The broader the tip, the more intricate the field emission pattern, each lobe corresponding to an emission area on the tip. Fortunately, the sharper the tip, the more gaussian the emission pattern. Moreover, a larger tip is less spatially coherent than a sharp tip.

Care must be taken when aligning the beam with the micrometer screws on the BLT that the image is not being centred on an emission lobe, but on the overall emission pattern.

3.5 Case study: LEEPS studies of an opaque edge

As discussed in Section 1.4.1, a good experiment for determining the coherence of the source is to scatter the beam off a sharp edge. This is done by approaching the tip near the edge of a hole in the perforated SiN window. From this very simple experiment, many properties of the microscope can be elucidated. Most importantly, coherence properties of the source can be determined. But this simple example also leads to a simple quantitative model for extracting parameters about the optical system.

The interaction of the electron wave with the SiN substrate can be described qualitatively by Huygens' principle: each point where the wave scatters acts as a point source of electrons. The case of the tip and the edge, there are two sources of electrons: those emanating form the tip and those scattered off the sharp edge. This was the case discussed in Section 1.4.1.

Each hole in the SiN membrane forms an aperture 2 μm in diameter. As the tip is

approached closer and closer, fringes near the edge of the hole become visible. These fringes are the diffraction pattern of the electron beam passing through the circular aperture that is the grid-hole. This diffraction pattern can be in one of two regimes: *Fresnel*, near field diffraction or *Fraunhofer*, far field diffraction. The difference between the two regimes is the shape of the wavefront incident on the object; in the Fresnel limit the source is very close to the object and the waves are spherical. The Fraunhofer regime is in the opposite limit; the source is far away, and the wavefronts are planar. This difference is illustrated in Figure 3.14. As a rule of thumb, the pattern is in the Fraunhofer regime when the source-object distance d satisfies the following expression [47]:

$$d > \frac{a^2}{\lambda} \tag{3.1}$$

For the aperture radius $a = 1$ μm and electron wavelength approximately 1 Å, the diffraction pattern will be within the Fresnel regime for source-object distances less than 1 mm. For an appreciable magnification, the source-object distance is far less than 1 mm - the image of the aperture is always a Fresnel diffraction pattern. Equation 3.1 is essentially a measure of the curvature of the wavefront compared to the size of the object. If the wavefront is curved over the extent of the object, it will create a Fresnel diffraction pattern.

As the tip is approached closer to the edge, still finer fringes become visible in addition to the Fresnel diffraction pattern due to the aperture itself. These finer fringes are shown in Figure 3.15a and b. These fringes are due to the scattering off the edge of the hole, rather than the pattern formed by the collective diffraction off the aperture, highlighted in Figure 3.15c. The difference in the period and decay length of the fringes is seen clearly in Figure 3.15d. Qualitative agreement between the Fresnel fringes seen in 3.15c and a simulated Fresnel diffraction pattern is shown in Figure 3.16.

The fine fringes originate from the wave scattering off the edge of the hole interfering with the wave directly from the source. If this is the case, there should be good agreement between these fringe patterns and the expression derived in Section 1.4.1. In order to properly fit the fringe pattern, the baseline must be removed. This is most easily accomplished by applying a high-pass filter to the data, removing the low-frequency shifting baseline. This preserves the frequency and phase of the fringes. The effect of this filter is seen in Figure 3.17a.

Unfortunately, this also has the effect of centring the fringe pattern at zero intensity, whereas the intensity of equation 1.7 is dependent on $\cos^2(\pi d\alpha^2/2\lambda)$, which varies between 0 and 1. To remedy this, the identity $\cos^2\theta = 1/2(\cos 2\theta + 1)$ is used to yield the expression used in curve fitting:

$$I(\alpha) = I_o \cos\left(\frac{\pi d\alpha^2}{\lambda}\right) e^{-\Gamma\alpha}, \tag{3.2}$$

which has appropriate intensity centred at zero. Additionally, to match the decay seen in

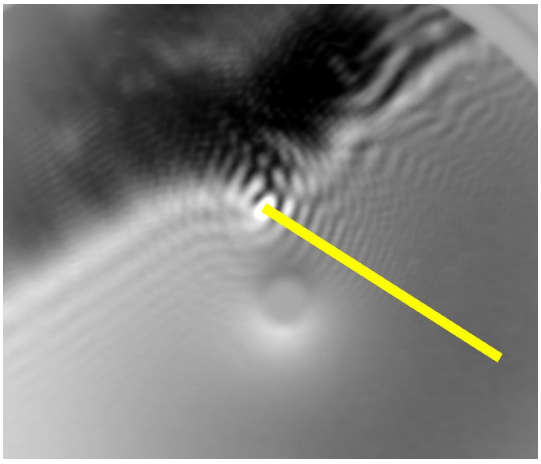

(a) The interference pattern from scattering off an opaque edge. The spot in the middle is a defect in the channel plate.

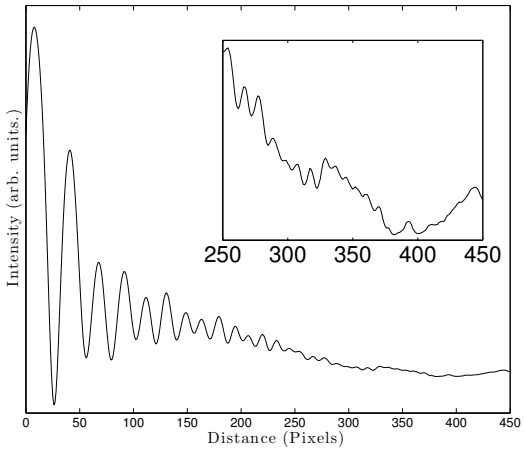

(b) A profile plotted along the line in (a). Inset: the tail magnified revealing many fringes.

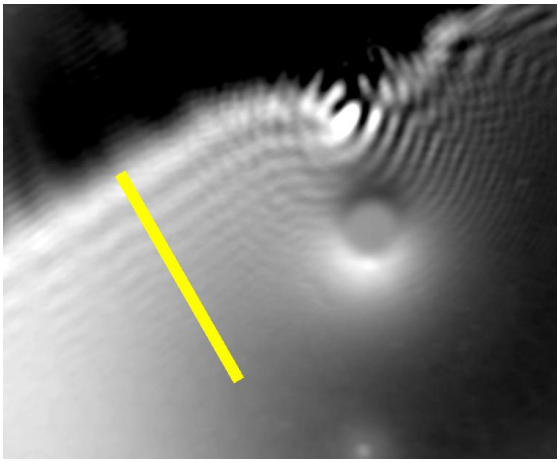

(c) Fringes along a different feature have a larger pitch

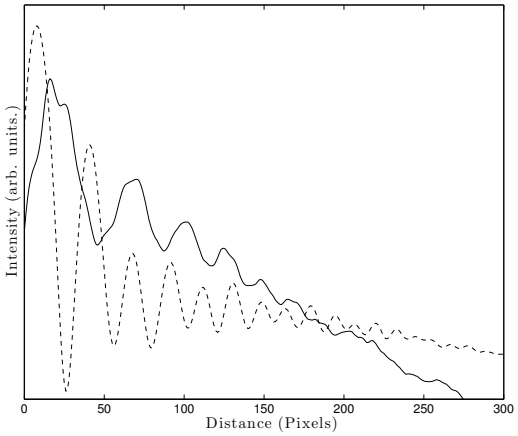

(d) A comparison of the finer fringes in (b) to the fresnel fringes in (c).

Figure 3.15: Many fringes are visible from scattering off an edge. Two different regimes of fringes can be seen. The fringes due to the interference pattern form scattering off the edge, highlighted in (b). Also visible, are fringes due to the Fresnel diffraction pattern, highlighted in (c). The direct comparison in (d) of the two fringe patterns show that the periodicity and decay length of the fringes is different.

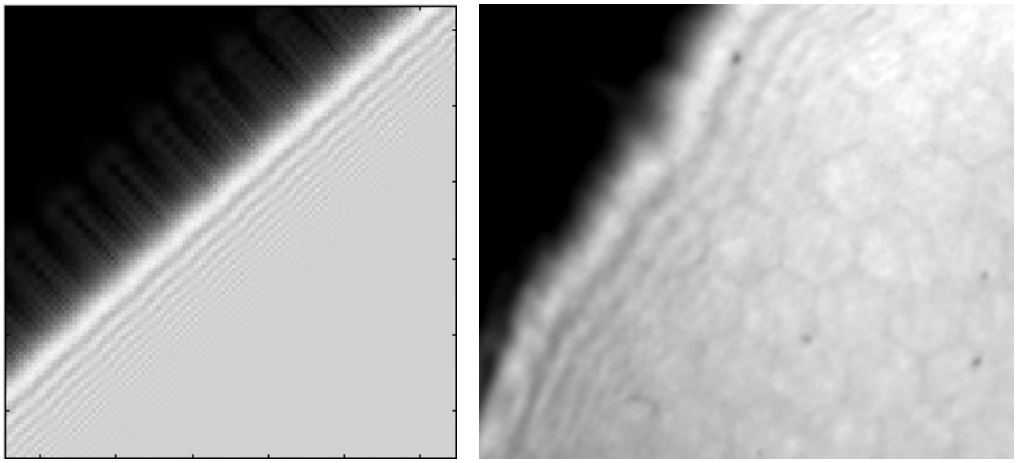

(a) Simulated Fresnel Fringes [48].

(b) Experimental image of Fringes along the edge of the aperture.

Figure 3.16: Comparison of Fresnel fringes to simulation.

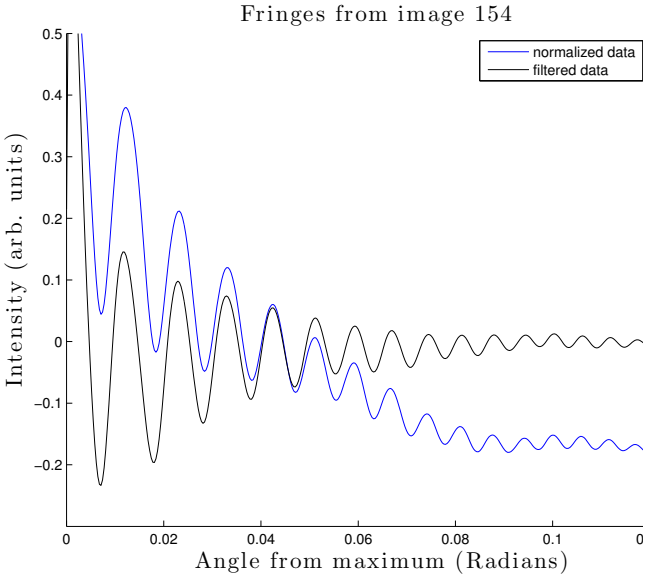

(a) Filtering the data, to fit the fringe pattern without the baseline.

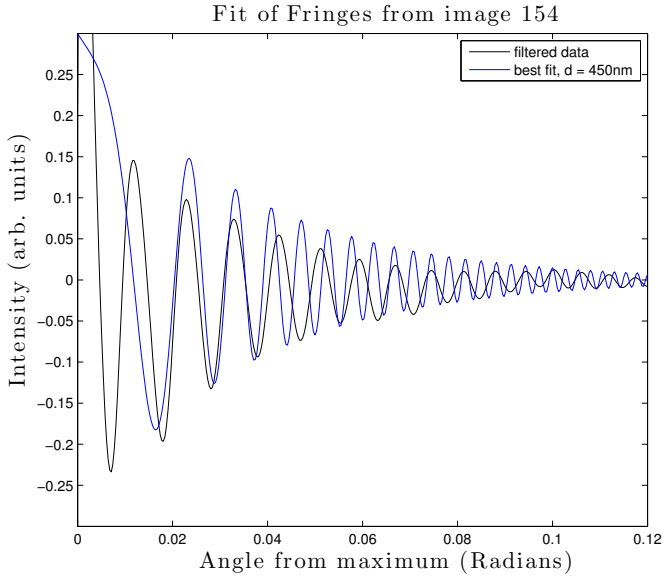

(b) The curve of best fit using eq: 3.2.

Figure 3.17: Filtering and fitting fringe data

the data, the fitting expression was multiplied by an exponential factor with a decay length Γ.

Unfortunately, the equation 3.2 gives poor agreement to the data. As shown in Figure 3.17b, at most two neighbouring fringes can be fit. The period of the fringe pattern decreases as the pattern evolves, but not at the same rate as in equation 3.2. Better agreement can be found considering the more general situation, where the tip and the edge are not on the same optical axis, but are offset by some small angle γ. Physically, the interference pattern is the same as the one described in equation 1.7. The only change is the path difference between the wave scattered off the edge and directly from the tip.

This path difference can be found using Figure 3.18:

$$\Delta r = r_3 + r_2 - r_1 \approx r_3 - r_3 \sin\beta = \frac{d}{\cos\gamma}(1 - \sin\beta), \tag{3.3}$$

where $r_1 = |\vec{r_1}|, r_2 = |\vec{r_2}|$ and $r_3 = |\vec{r_3}|$.

This expression easily reduces to the case discussed in Section 1.4.1, by taking $\gamma = 0$ and $\beta = \pi/2 - \alpha$. More generally, $\alpha + \beta + \gamma = \pi/2$. For any experiment γ is held fixed, and β is related to α by $\beta = \pi/2 - \gamma - \alpha$. Substituting this result into 3.3 yields:

$$\Delta r = \frac{d}{\cos\gamma}(1 - \sin(\pi/2 - \gamma - \alpha)) = \frac{d}{\cos\gamma}(1 - \cos\gamma + \sin\gamma\sin\alpha). \tag{3.4}$$

Now, expanding to second order in α near $\alpha = 0$ and simplifying yields:

$$\Delta r = d\left(\frac{1}{\cos\gamma} - 1 + \frac{\alpha^2}{2} + \alpha\tan\gamma\right), \tag{3.5}$$

substituting in equation 1.7:

$$I(\alpha) = |\Psi_{tot}|^2 = I_o\cos^2\left(\frac{d\pi}{\lambda}(\frac{1}{\cos\gamma} - 1 + \frac{\alpha^2}{2} + \alpha\tan\gamma)\right). \tag{3.6}$$

Which, again for $\gamma = 0$ reduces to the result in 1.7. It is also worth noting that expanding to second order in α near $\alpha = \pi/2 - \alpha$ leads directly to the familiar result for the double slit:

$$I(\alpha) = I_o\cos^2\left(\frac{\pi d}{\lambda}\alpha\right) \tag{3.7}$$

As in expression 3.2 using equation 3.6, to fit the high-pass filtered data, the expression must be centred at zero amplitude and attenuated by an exponential decay. Applying the same identity and exponential decay yield the expression used for fitting:

$$I_{\text{fit}} = I_o\cos\left(\frac{2\pi d}{\lambda}(1/\cos\gamma - 1 + \alpha\tan\gamma + \alpha^2/2)\right)\exp(-\Gamma\alpha) \tag{3.8}$$

This fitted expression has four parameters: γ, Γ, λ and d. For each image, the electron energy and hence the wavelength, λ, is given by voltage difference between tip and sample.

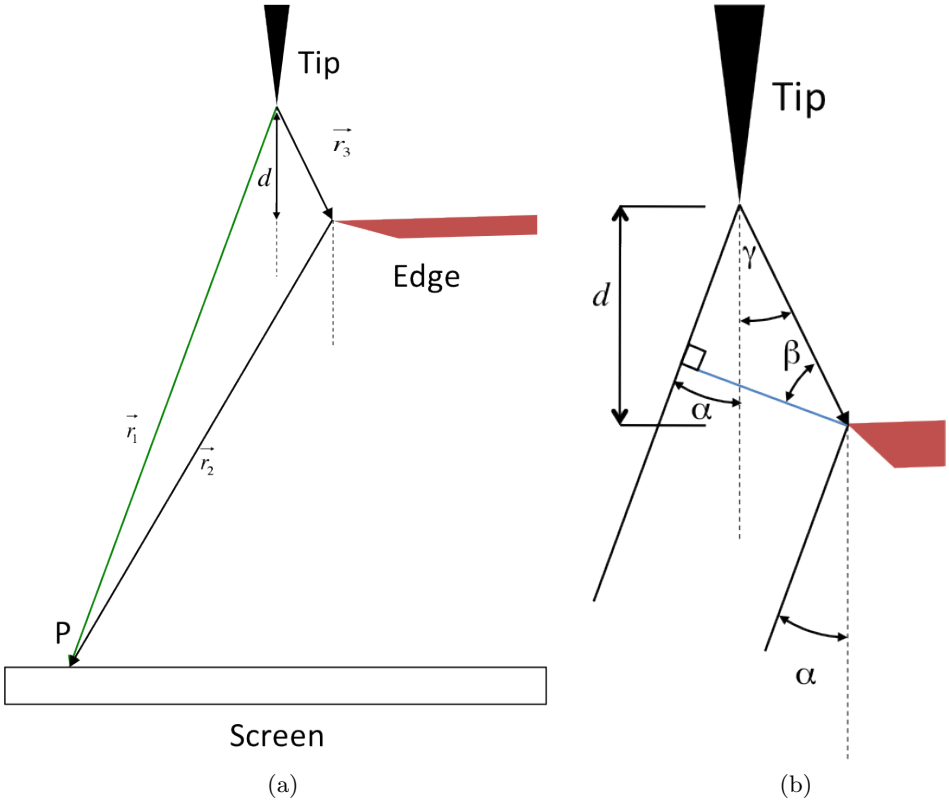

Figure 3.18: Scattering from an off-axis edge.

The fit can be used to extract physical quantities of γ and d, the tip-sample separation. The decay Γ is thought to reflect many complicated processes that limit the coherence of the source and little physical significance is attached to the exact parameter.

This model for the creation of the fringe pattern gives some insight to the general process for hologram formation. Objects imaged using LEEPS will be on the order of a nanometre in size, a small distance compared to the tip-sample separation. The object itself can be thought of as a series of discrete sources, re-radiating towards the detector. These sources will be all very near a distance d from the tip and offset from the optical axis by some angle very near to γ. As a result, holograms resulting form objects much smaller than d are expected to qualitatively agree very well with the fringe patterns predicted by equation 3.8. Agreement will be less strong for higher order fringes, which will cause differences in the fringe pattern for extended objects, compared to simple point scatterers.

Using this fit, good agreement can be found with the filtered fringe patterns, as seen in Figure 3.19a. The fit is not perfect, especially for higher order fringes. This disagreement is most likely due to the edge not being a simple point scatterer, but an extended object. Moreover, the angle γ used in the fits is uniformly small, around 2°, which is reasonable because the edge is near the axis of the tip in all the images.

In the Nanonis software, the displacement of the tip is measured by the voltage applied to the z-channel of the tube scanner. This relationship is known to be fairly linear over the

voltage range used (-10 V to 10 V) [49]. This value is the displacement of the tip relative to zero-voltage. Fitting the fringes using 3.8 gives the absolute displacement between tip and sample d. These two displacements can be compared by taking the difference between the tip displacement in subsequent images, by setting the displacement in the first image to 0. This comparison yields good agreement between the known displacements of the tube scanner, as seen in Figure 3.19b.

Ideally, the tip would be moved into tunnelling with the sample in each experiment to obtain an absolute measurement of the tip-sample distance. In practice, this is difficult, since the coherence properties of the tip depend on the specific structures of the terminal atoms of the tip. There is a concern that by bringing the tip near enough to the sample for tunnelling, a few Angstroms, the interactions between the tip and sample will alter the carefully prepared structure of the tip. This might ruin the coherence properties of the source.

Since there is good qualitative agreement of the fringe patterns and the quantitative agreement of the relative tip-sample distances, the model described above can be used to extract information from the fringe pattern that will be critical to holographic reconstruction. Fringe patterns for a variety of magnifications and incident wavelengths are shown in Figure 3.20.

3.6 Coherence properties of the beam

The fringe patterns can also be used to extract information about the coherence of the beam and ultimately the expected resolution of the instrument with a given source. The width of the fringe pattern is related to the resolution by the numerical aperture, first touched on in Chapter 1 in equation 1.4:

$$R \geq \frac{\lambda}{2 \sin \alpha}. \tag{3.9}$$

Since the wavelength and the coherence angle change slightly from image to image, the resolution as predicted above varies. The coherence angle is $8 \pm 0.5^\circ$ in these data the resolution is expected to be 5 ± 0.6Å.

Another measure for the resolution, widely accepted by the community [30, 31, 16, 29, 50], is the virtual source size:

$$R_{\text{eff}} = \frac{\lambda}{\pi \alpha}. \tag{3.10}$$

This value gives a more flattering estimate of resolution of 3 ± 0.6Å.

The number of fringes present in the fringe pattern also gives some information about the energy spread of the source [16]. Specifically:

$$n_{\max} \leq \frac{E}{\Delta E}. \tag{3.11}$$

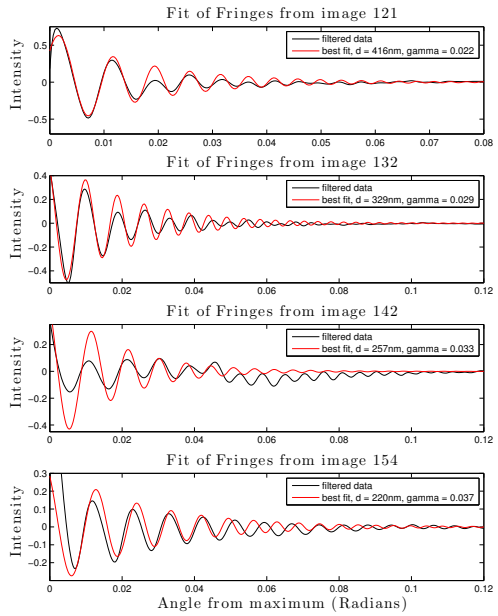

(a) Agreement between fringe patterns and fit. Sections taken along the same line as in Figure 3.15a

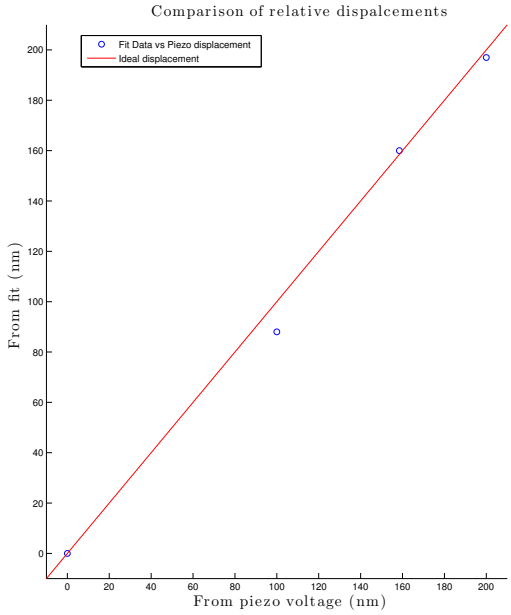

(b) Tip sample displacements from fitting and measured from absolute tube scanner displacements

Figure 3.19: Fitting fringes using equation 3.8 produces good agreement between fringe patterns and absolute measurements of tip-sample displacements

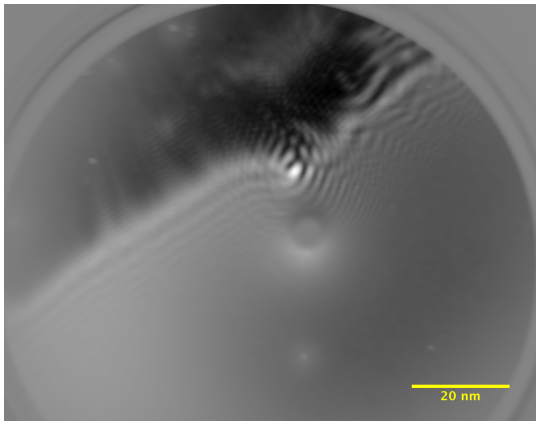

(a) 329 nm, 96 eV, 1.25 Å, 0.26 nA.

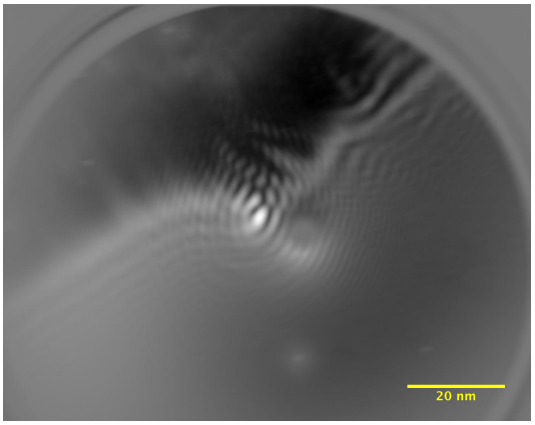

(b) 257 nm, 88 eV, 1.30 Å, 0.32 nA.

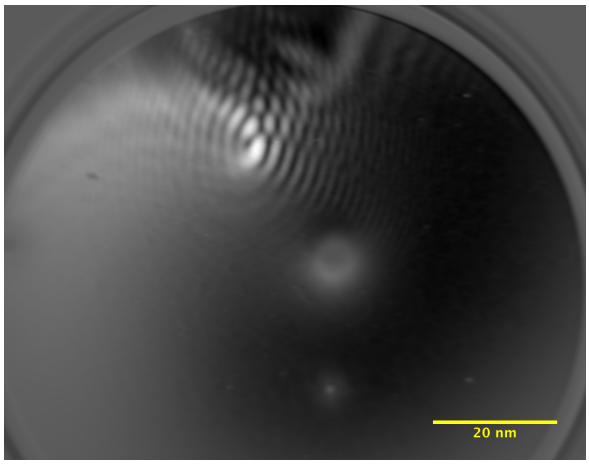

(c) 220 nm, 80 eV, 1.37 Å, 0.39 nA.

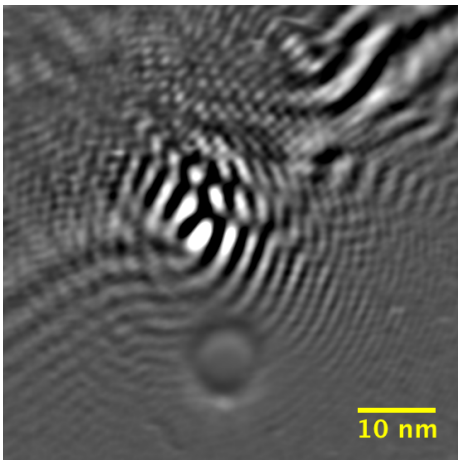

(d) same as (a), high-pass filtered to show fringes.

Figure 3.20: Fringe patterns from scattering off the edge. Listed below are tip-edge distances, imaging voltages, electron wavelengths and beam currents

From Figure 3.15b, with 28 fringes at 96 eV, the energy spread can be found to be no greater than 3.4 eV. This number of significantly greater than measured energy spreads of typical tungsten nanotips. Previous studies have reported energy spreads less than 1 eV [51, 52, 47] even at room temperature. The fact is, energy spread is not the limiting factor in the coherence of the beam, the opening angle is. The limited divergence of the electron beam restricts the number of fringes than can be seen in a manner unrelated to the energy spread. The effect of tip shape on opening angle and coherence is a matter for further study.

In conclusion, scattering off an edge gives insight in the behaviour of the microscope as well as a good qualitative model for the mechanism for the formation of interference patterns. The model leads to good quantitative agreement between known displacements and magnifications of the LEEPS microscope. Finally, this experiment yields an upper bound for the energy spread of the electron source and a lower bound for the resolution of the microscope.

Chapter 4

LEEPS study of carbon nanotubes

Since their discovery in 1991 by Sumio Iijima [53], carbon nanotubes have been an example of the promise of nanotechnology. Structurally, they are hollow tubes made from rolled up sp^2-bonded graphitic carbon. Their promise is derived from the sensitivity of their electronic characteristics to their structural properties: depending on their diameter and chirality, nanotubes can vary from semiconducting to metallic. Because of this variety of electronic characteristics, it's tantalizing to envision how carbon nanotubes might be applied to some kind of nanoscale computing architecture. Although nanotubes can be grown to possess this variety of electronic properties, there is no recipe that provides a high yield of nanotubes with identical structure. To separate nanotubes according to their electronic characteristics, the nanotubes are mixed with surfactants that selectively bind to certain the tubes. The tubes are then separated according to their density by using ultracentrifugation [54]. Single-walled carbon nanotube (SWNT) samples monodispersed in this manner, with similar diameter and electronic characteristics, are commercially available from companies like Nanointegris. Conveniently, the optical characteristics of the nanotubes reflect their electronic structure: metallic nanotubes can be readily discriminated from semi-conducting and insulating. The separated nanotubes can be seen in Figure 4.1, along with their optical characteristics.

SWNTs are a sample of interest primarily because they are conductive, mechanically-robust, easily characterized, nanoscale samples that can be handled in ambient conditions. In order to prevent charging under the electron beam, metallic nanotubes must be used. As a standard, metallic nanotubes 1.1 nm in diameter, purchased from Nanointegris.

4.1 Sample preparation

SWNTs were delivered mixed with surfactant in aqueous suspension, in order to prevent the nanotubes from agglomerating into large bundles. However, this surfactant was removed from the suspended SWNTs before imaging in LEEPS to avoid contamination. To accomplish this, the as-delivered aqueous suspension was mixed with isopropanol, to dissolve the surfactant. Next, the isopropanol mixture was placed in an ultra-sonic bath to disperse the

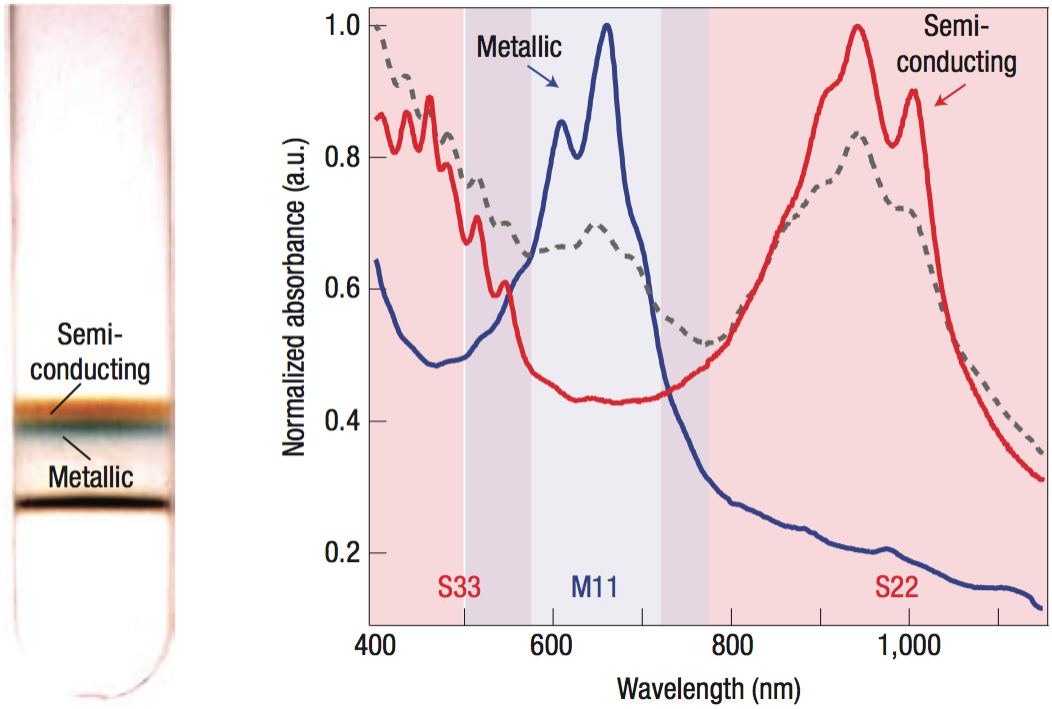

Figure 4.1: Using a combination of selective chemistry and ultracentrifugation, single-walled nanotubes can be sorted according to their electronic characteristics (left). The electronic characteristics of SWNTs are readily measured using optical absorbance (right). Figure used with permission from [54].

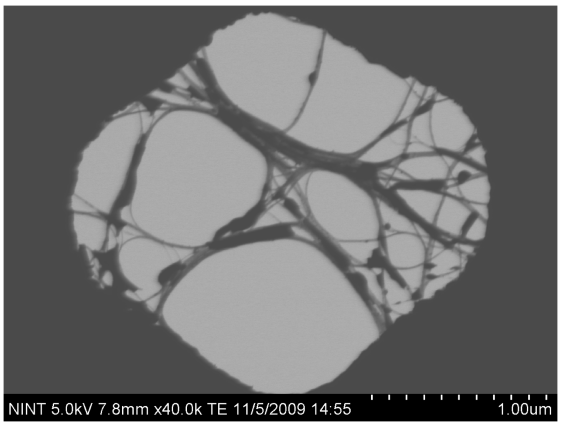

(a) SEM image of SWNTs bundles suspended across a hole in the SiN window.

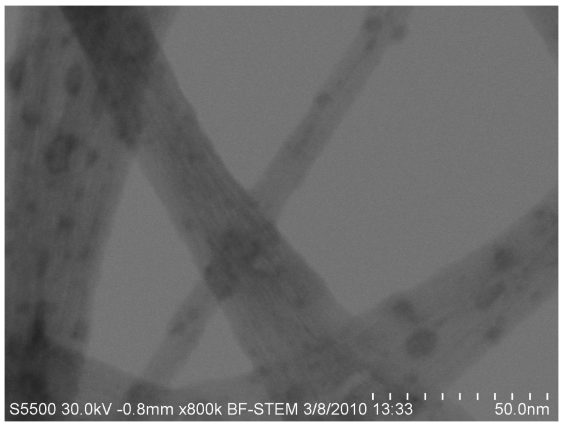

(b) A high magnification SEM image of a SWNT bundle.

Figure 4.2: SEM images of bundled SWNTs.

nanotubes. The SWNT were transferred onto an SiN window by using a pipette to drip the SWNT suspension onto the window and allowing the suspension the be drawn through the window onto filter paper. The SWNT concentration on the window was controlled by the number of drops.

Unfortunately, individual suspended SWNTs were never achieved. Some degree of bunching was always observed in SEM as seen in Figure 4.2. However, bundles as small as 10 nm in width were observed and the samples were examined in LEEPS.

Once the samples were deposited on the grid, they were brought into vacuum through the load-lock. Once in the prep chamber they were heated in the pliers between 400 and 500 °C until the pressure fell below $1.5\text{x}10^{-10}$ Torr. This usually took about 45 minutes. Samples may be annealed hotter, for shorter times, but the the temperature must be changed slowly as rapid thermal expansion and contraction can break the fragile grids.

The sample was then loaded into the scanning head, and the tip approached to within a few millimetres of the perforated window. High magnification was obtained during imaging as described in Section 3.3.

4.2 Carbon nanotubes bundle as a double slit

The simplest model to describe the fringe patterns generated by scattering an electron wave off a nanotube bundle is to consider the bundle as a double slit. Again, according the Huygen's principle, each scattering site can be treated as a discrete source. In the case where the edges of the nanotube bundle are strongly scattering the electron wave, the situation can be approximated by a double slit, where the sources of radiation are either edge of the bundle, as in Figure 4.3.

The largest shortcoming of this model is that it ignores the effect of the electric field surrounding the carbon nanotube bundle. In LEEPS, the sample must also serve as anode and a voltage difference must be applied between tip and sample which results in a drastic potential gradient between the tip and the bundle. The trajectories of electrons emitted from the tip are directed by the field gradient around the nanotube. As a result, simple scattering is an incomplete description of the physical situation.

4.3 Carbon nanotubes as a bi-prism

A simple model for understanding the effect of the electrostatics of the carbon nanotube in LEEPS is to treat it as a bi-prism [55, 56, 57, 58]. Developed by Möllenstedt in 1953 [59], the electron bi-prism was a pioneering invention in the field of electron interferometry. The device itself is simply a thin conductive filament, typically made from a metallized quartz thread [51, 60, 61]. The filament is biased relative to nearby electrodes by a potential U_f. When an electron wave is incident on the filament, wavefronts on either side filament are distorted by a constant angle due to the constant potential gradient. The wavefronts

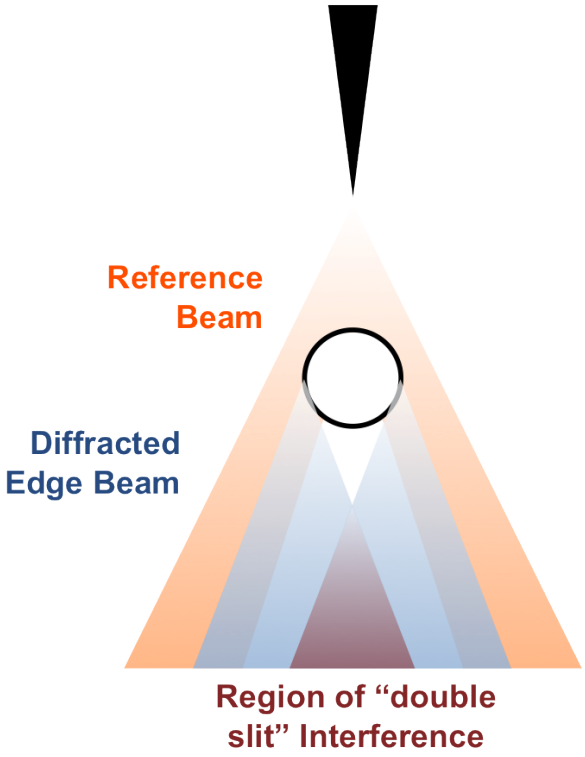

Figure 4.3: A simple model to describe the fringe patterns from imaging a nanotube bundle in LEEPS.

are directed towards one-another, resulting in the interference of the waves on a nearby detector. The degree of coherence of the beam can be ascertained by the pattern resulting from the bi-prism. A bi-prism is illustrated in Figure 4.4.

The degree of distortion and hence the degree of interference of the waves can be tuned by changing the voltage on the filament. To understand how this works, consider two waves ψ_1 and ψ_2 deflected by a bi-prism. The bi-prism deflects the waves so that the magnitudes of their wave-vectors are equal, but their trajectories are bent towards one another. Consider electrons with wavevector:

$$\begin{aligned} |\vec{k_1}| &= |\vec{k_2}| = k_o \\ \vec{k_1} &= (k_x, 0, k_z) \\ \vec{k_2} &= (-k_x, 0, k_z). \end{aligned} \tag{4.1}$$

The pattern created by the interference of the waves is: $I = |\psi_1 + \psi_2|^2 = |\psi_1|^2 + |\psi_2|^2 + \psi_1\psi_2^\dagger + \psi_2\psi_1^\dagger$. For planewaves of the form $\psi_n = a_n e^{2\pi i \vec{k_n}\cdot\vec{r}}$, the intensity of the pattern along the x-direction is:

$$I(x) = 2I_o(1 + \cos(4\pi k_x x)) = 4I_o \cos^2(2\pi k_x x) \tag{4.2}$$

From the ray diagram in Figure 4.4b, the angle of the overlap between the two waves is given (in the paraxial approximation) by $\beta = 2(a/(a+b))\gamma$, where γ is the deflection

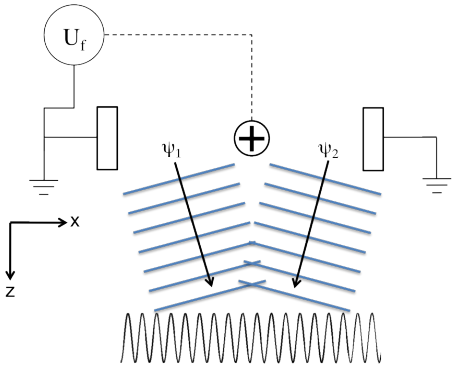

(a) An electron bi-prism.

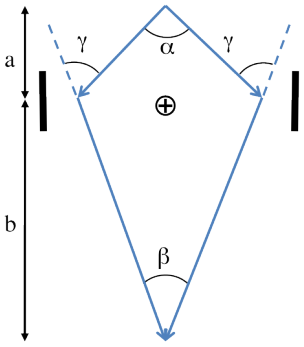

(b) A ray diagram showing the electron beam incident on the bi-prism from source to detector.

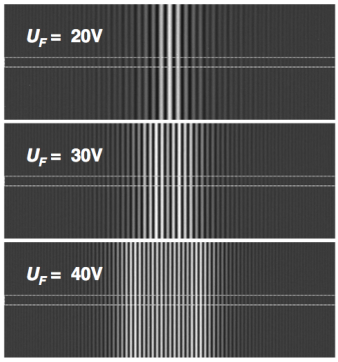

(c) Fringes tuned by a bi-prism in TEM reproduced with permission from [60].

Figure 4.4: The working principle of an electron bi-prism along with a typical interference pattern.

angle of the bi-prism and a and b are the source-filament and filament-screen distances, respectively. Each side of the bi-prism can be thought of as a set of deflection plates, like in an old cathode ray tube, where the constant voltage gradient directs the beam. This deflection angle can be expressed as $\gamma = \gamma_o U_f$, where γ_o is the angular deflection per volt of the bi-prism. The fringe spacing of the interference pattern is therefore:

$$s = \frac{1}{2k_x} = \frac{a+b}{2k_o a \gamma_o U_f}. \tag{4.3}$$

Isolating for k_x yields:

$$2k_x = \frac{2k_o a \gamma_o U_f}{a+b} = \frac{2a\gamma_o U_f}{a+b}\frac{1}{\lambda}, \tag{4.4}$$

since $k_o = 2\pi/\lambda$.

Substituting 4.4 into 4.2 yields:

$$I(x) = 4I_o \cos^2\left(\frac{4\pi a \gamma_o U_f}{a+b}\frac{1}{\lambda}x\right). \tag{4.5}$$

Approximating α for small angles: $\tan(\alpha) \approx \alpha \approx \frac{x}{a+b}$, yields:

$$I(\alpha) = 4I_o \cos^2\left(\frac{\pi D}{\lambda}\alpha\right), \tag{4.6}$$

where:

$$D = 4a\gamma_o U_f. \tag{4.7}$$

When compared to equation 3.7 it is easy to see the purpose in isolating $D = 4a\gamma_o U_f$, since the expression in equation 4.6 is identical to that of the double slit. The bi-prism ex-

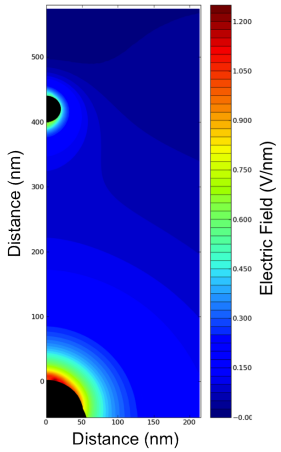

(a) Simulation of the magnitude of the electric field surrounding the tip-nanotube system [62].

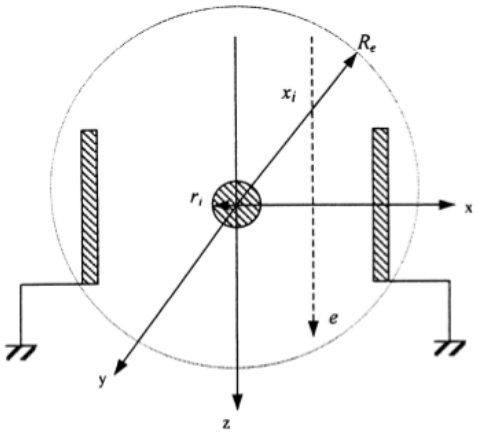

(b) How the field around a nanotube bundle approximates a bi-prism. Reproduced with permission from [56].

Figure 4.5: The field around the nanotube bundle and how it can be compared to that of a bi-prism.

periment is analogous to the double slit, where the effective slit separation can be controlled by the bi-prism voltage and the distance between the emitter and the filament.

Instead of an independently biased filament arranged between grounded plates, the nanotube bundle is grounded relative to the tip. This situation can be approximated by a bi-prism; the field surrounding the bundle is nearly constant over a region around the tube as illustrated by the simulation in Figure 4.5a. This region can be thought of as the region between the filament and the plates in a traditional bi-prism as illustrated in Figure 4.5b. As a result, the electrons incident on either side of the nanotube bundle experience a potential gradient which deflects their trajectory towards each other.

The relationship between the imaging geometry and electrostatics can be explored using LEEPS. By bringing the tip very close to the filament and recording the pattern for a variety of tip voltages and tip-sample distances. By exploring this relationship, it is possible to study the coherence properties of the beam [60] and the validity of treating the nanotube bundle as a bi-prism [55, 56, 57, 58]. Also it is possible to gain some insight about the behaviour of the field surrounding the nanotube-bundle and the validity of the simple models of a nanotube bundle as a simple double slit, or a bi-prism.

4.4 Fringe patterns

As the tip approaches the nanotube bundle, fringes appear along the axis of the bundle. This is shown in Figure 4.6. Again, as in the experiment with the edge of the SiN window, there are two qualitatively different types of fringes in the pattern: a broader, low-frequency set, and a fine, high-frequency set. These fringes can be seen distinctly by filtering the data,

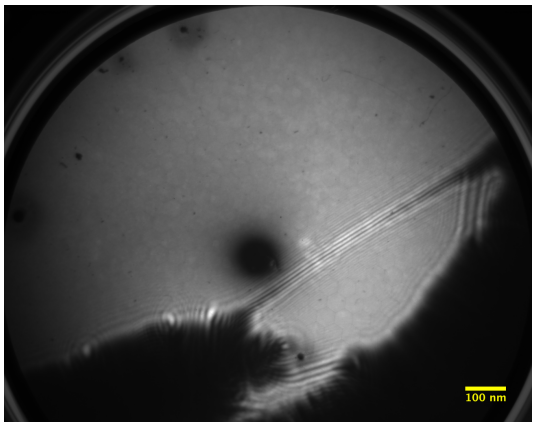

(a)

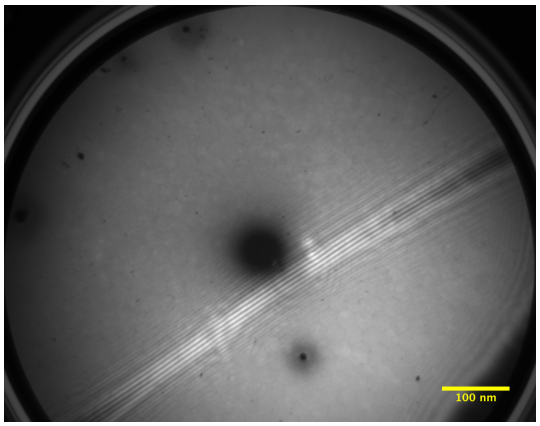

(b) 118 eV, 1.12 Å, 0.29 nA.

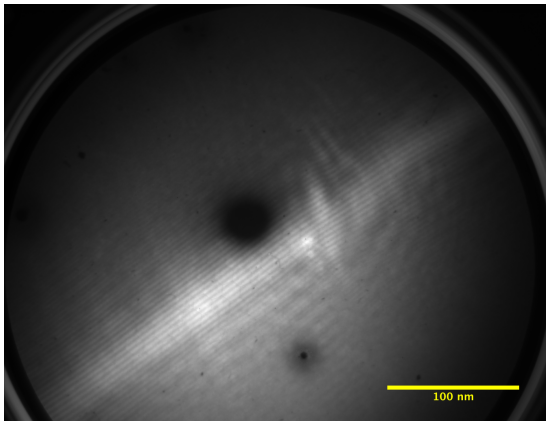

(c) 87 eV, 1.31 Å, 0.29 nA

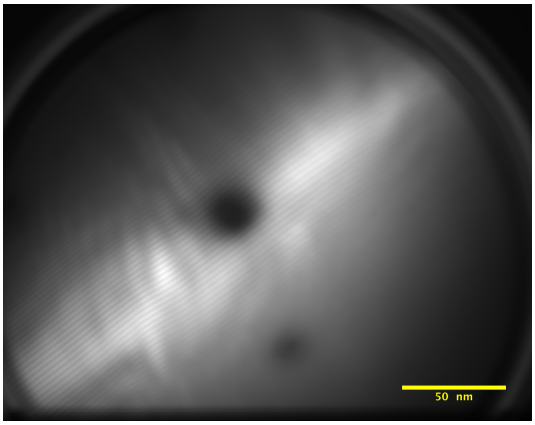

(d) 89 eV, 1.3 Å, 1.2 nA

Figure 4.6: Change in interference pattern while approaching the SWNT bundle. As the tip is approached the fringe pattern qualitatively changes. The broader set of fringes is magnified in a manner that is qualitatively different than the finer fringes. At high magnifications, as in (d) fringes can be seen to extend to the limits of the detector. Listed below each image (where available) are the incident electron energy, electron wavelength and beam current.

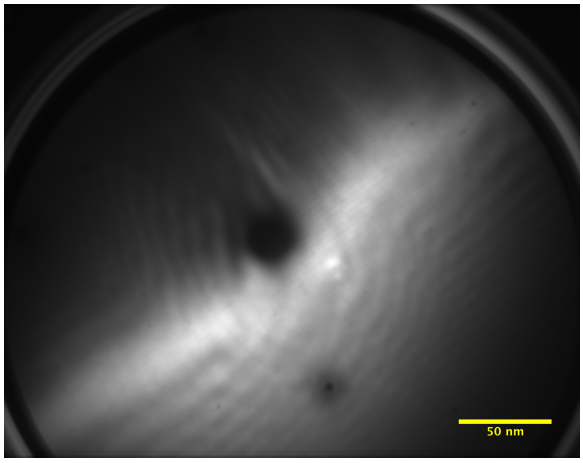

(a) 82 eV, 1.35 Å, 0.44 nA.

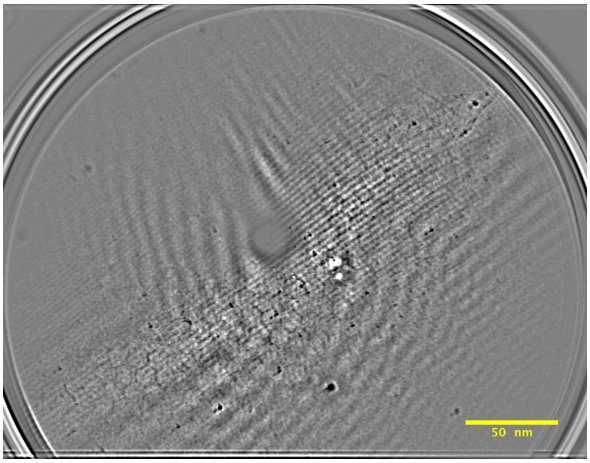

(b) High-pass filtered image.Note: hexagonal pattern is the structure of the detector.

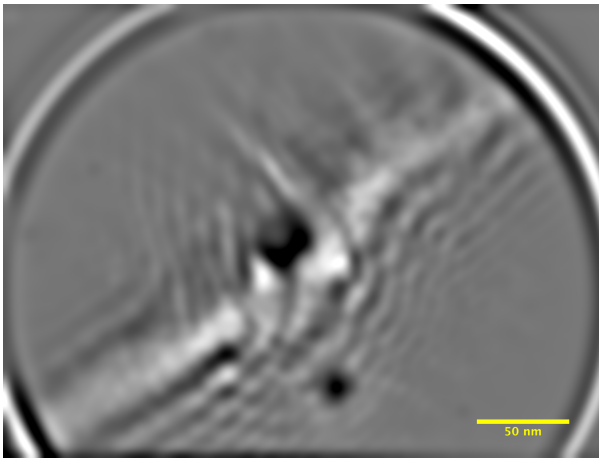

(c) Low-pass filtered image. Note: hexagonal pattern is the structure of the detector.

Figure 4.7: Filtering the data to reveal the different sets of fringes. The original image (a) (shown with the electron energy, wavelength and beam current below) contains two distinct sets of fringes. High-pass filtering the image results in (b). This accentuates the fine fringes, thought to be due to the bi-prism interference. The high-pass filter has the unintended consequence of amplifying the noise in the image. The image can be low-pass filtered, as in (c). This accentuates the low-frequency fringes, which are thought to be the Fresnel diffraction pattern due to classical scattering off the SWNT bundle.

as is shown in Figure 4.7. The broader set of fringes is thought to be the Fresnel diffraction pattern from scattering of the bundle. These fringes share many qualitative aspects of a typical Fresnel diffraction pattern resulting from a rectangular barrier, or equivalently a rectangular slot. The finer, more sinusoidal fringes are thought to be due to the bi-prism effect. These different sets of fringes can be accentuated by high-pass or low-pass filtering the images. The finer fringes are accentuated by using a high-pass filter, as in Figure 4.7b. The broader fringes can be accentuated by applying a low-pass filter, as in Figure 4.7c.

For processing, the images were high-pass filtered to accentuate the finer fringes, and a line profile was taken across each fringe patterns. The fringe pattern was fit according to equation 4.6. This process is illustrated for two extremes in magnification in Figure 4.8. The number of fringes with constant period varied by image magnification. Images with lower magnification had fewer fringes of constant period. Images with higher magnification had more constant period fringes. The angular width of the constant period fringe pattern scales roughly with magnification.

Also, the limited width over which the fringes have a constant period reflect a further limitation of this simple model. Outside the regime of constant period fringes, the interference pattern is that of a hologram, consisting of interference between the reference beam and the wave scattered off the bundle in a manner that is not simply described by the bi-prism behaviour.

As the tip approaches the bundle, the visibility of the finer fringes relative to the diffraction pattern decreases. The *visibility* of the fringes is defined by [60, 30, 31, 16, 29]:

$$V = \frac{I_{max} - I_{min}}{I_{max} + I_{min}}, \tag{4.8}$$

where I_{max} and I_{min} are the intensities of neighbouring maxima and minima. As the tip is approached nearer to the sample, this visibility drops proportionally. The relationship between tip-sample distance and fringe contrast is shown in Figure 4.9a. The contrast is reduced as the tip approaches the bundle, since a greater portion of the beam is simply scattering off the bundle. As a result, a larger portion of the intensity of the pattern is due to this simple Fresnel diffraction, rather than the bi-prism interference pattern.

For each fringe pattern of constant period, a value of D according to equation 4.5 can be fit. From the parameters of the experiment, the filament potential relative to the source U_f, and the displacement of the filament relative to the source a are known. This allows the relationship between D and $4a\gamma_o U_f$ to be explored by plotting D vs. $4\gamma_o(aU_f)$. The slope of this linear plot should equal to $4\gamma_o$.

4.5 Fitting the data

The data are plotted in Figure 4.9b and can be fit a with a line of slope 2.1x10^{-5} rad/V. This yields a bi-prism deflection value for γ_o of 5x10^{-6} rad/V. A typical value for a bi-prism

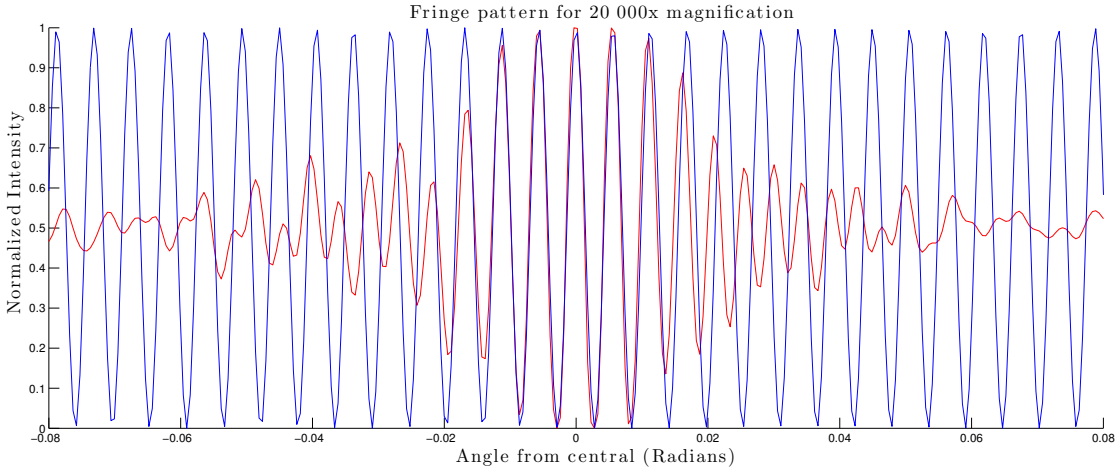

(a) Fringes, along with fit from image 4.6b.

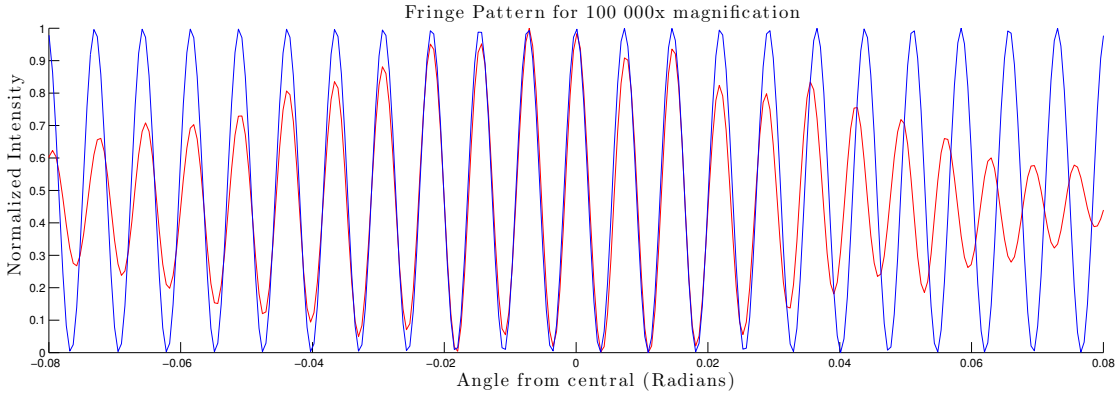

(b) Fringes, along with fit from image 4.6d.

Figure 4.8: Change in interference pattern while approaching the SWNT bundle.

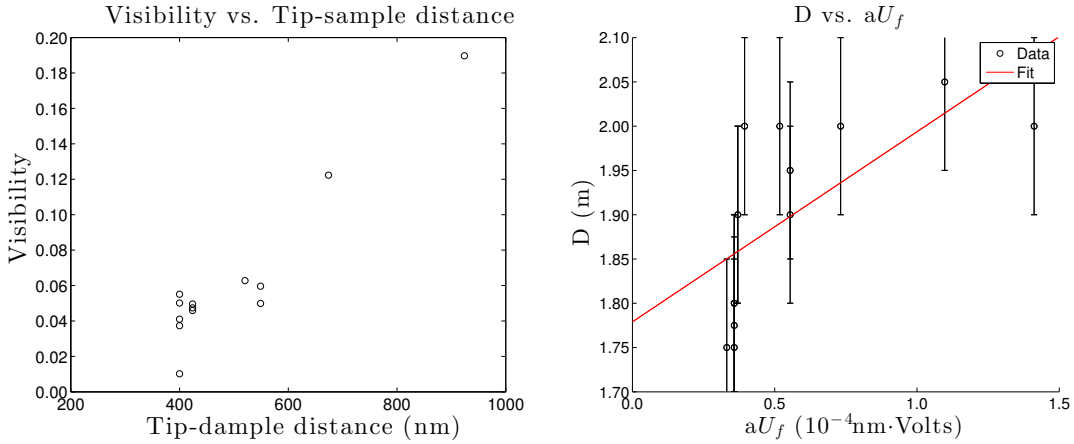

(a) Change in fringe visibility as the tip approaches the sample.

(b) Fitting to find γ_o.

Figure 4.9: Determining the parameters of the bi-prism from fitting. (a) As the tip is approached nearer to the SWNT bundle, the visibility of the fine fringe pattern decreases. This is thought to be due to an increased portion of the electron beam being scattered by the bundle. Since less of the electron beam is being re-directed by the bi-prism, the visibility of the fine fringe pattern drops. Shown in (b) are fits of the fringe patterns to the parameter described in equation 4.7. This allows the behaviour of the bi-prism model to be tested over a variety of distances and relative filament voltages.

employed in a TEM is on the order 10^{-4} [60]. For a typical bi-prism, this angular deflection is a consequence of the potential gradient imposed by the geometry of the electrodes that make up the bi-prism. As previously mentioned, a bi-prism is similar to two deflection plates, side-by-side, directing the beams towards each other. For an electron being accelerated by a potential V_o through parallel plates of length l with an electric field E between them, this deflection angle γ is equal to [63]:

$$\gamma = \frac{El}{2V_o}. \tag{4.9}$$

The physical situation of the nanotube bundle is significantly more complicated, as the electrons don't pass through a uniform electric field along a single direction; instead the electrons pass through the radial field due to the bundle.

Additionally, there is quite a spread in the value for D for images taken at high magnifications and low voltages, as seen on the left side of the plot in Figure 4.9b. This spread may be due to an additional effect of the beam on the bundle: charging. As mentioned in Section 4.1 the nanotubes are delivered mixed in surfactant, which has proven to be difficult to remove. When being imaged in SEM, a layer of contamination is often visible on the nanotubes. Although the nanotubes are metallic, the contamination present on the nanotube bundles may cause them to charge.

In Figure 4.10, the fit parameter $D = 4a\gamma_o U_f$ is plotted versus the beam current emitted from the tip. These data show that higher beam-currents tend towards a lower value of

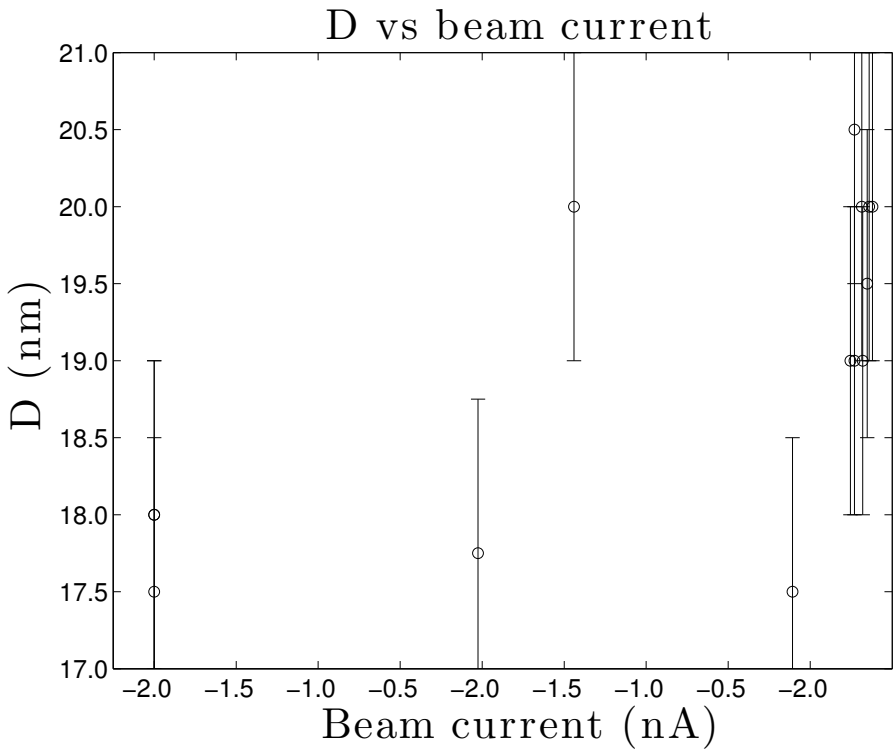

Figure 4.10: The relationship between beam current and D. As the tip is approached nearer to the bundle, the deflection angle decreases. As the tip is approached, the flux of field-emitted electrons incident on the bundle increases. The bundle may become negatively charged as the flux increases which would account for this decreased deflection angle.

D. A lower value of D corresponds to a lower deflection angle. As beam current increases, the bundle may becomes negatively charged under the increased flux of incident electrons. This charged filament will repel electrons more than an uncharged filament, reducing the deflection angle at the bi-prism. Incident electron energies in this system are very low, so positive charging due to secondary electron generation is not expected [64].

4.6 Coherence properties of the beam

As discussed in Section 3.6, there are two popular measures for extracting the resolution of the beam from the lateral coherence angle for the pattern: the virtual source size and the numerical aperture.

From Figure 4.11, the angular width of the fringe pattern is $\alpha = 14.3 \pm 0.5°$. Using the DeBroglie wavelength, $\lambda = 1.3$ Å, the expected resolution from the numerical aperture is:

$$R \geq \frac{\lambda}{2 \sin \alpha} \approx 2.6 \pm 0.6 \text{ Å}.$$

These measurements yield a virtual source size of:

$$R_{\text{eff}} = \frac{\lambda}{\pi\alpha} \approx 1.7 \pm 0.6 \text{ Å}.$$

Resolution is improved from the edge scattering experiment in Section 3.6. This is likely due to the fact that tip used in the nanotube experiments is sharper than the one used in the edge experiment. As seen from FIM after the field assisted etch, the tip employed in the edge experiment ended in a small cluster of atoms, whereas the tip used in the nanotube experiment ended in a single atom. Both of these tips are shown in Figure 4.12. The impact of the structure of the terminal atoms of the tip on the coherence of the images is a matter for future investigation.

Even so, the above calculations are likely underestimates of the resolution of the beam for two reasons. First, the width of the pattern is limited by the width of the detector. Fringes with high signal to noise are detectable at the limits of the detector. Second, much of the beam is being diffracted by the wide nanotube bundle, leaving less of the reference beam to interfere and contribute to the pattern. This is evident by the drop in visibility of the fringes as a function of magnification in Figure 4.9a. A smaller bi-prism would yield a similar fringe pattern but with much higher visibility, like those seen in lower magnification images in Figure 4.6.

Also a more refined estimate of the energy spread of the tip can be found. From the pattern we can count some 81 fringes, which leads to an upper limit on the energy spread of 1.1 eV. Again, this is likely an overestimation of the spread since the width of the pattern, and hence the number of fringes, is limited by factors other than the coherence of the beam.

Although these data provide insight into the coherence properties of the beam, they are also holograms which can provide structural information about the sample. In Figure 4.11b, there is a change in the fringe pattern along the length of the nanotube bundle. The bi-prism model suggests that this inhomogeneity is due to distortions in the field along the bundle, which must reflect a change in the structure of the bundle along its length. However, reconstruction of these holograms is a non-trivial task, since the field distortion of the electron beam is convolved with the structure of the bundle. In the past, the structure of such objects has been reconstructed by modelling the field around the filament in conjunction with the generation of the hologram [57, 55]. This method will be explored in future reconstruction attempts.

Overall, carbon nanotubes provide a useful method for controlling the interference of the beam, using a bi-prism-like experiment. This experiment can help deduce the coherence properties of the beam, demonstrating that the microscope is very close to Angstrom resolution and is actually limited by the geometry of the detector and sample, rather than by the beam itself.

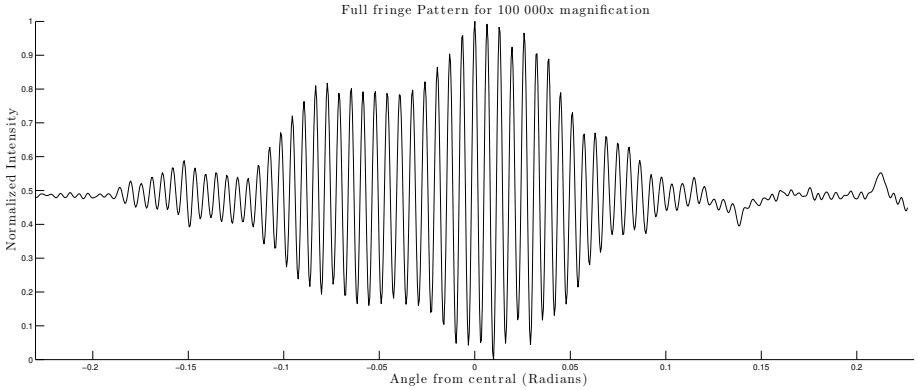

(a) Line profile showing angular width of the fringe pattern in Figure 4.6d.

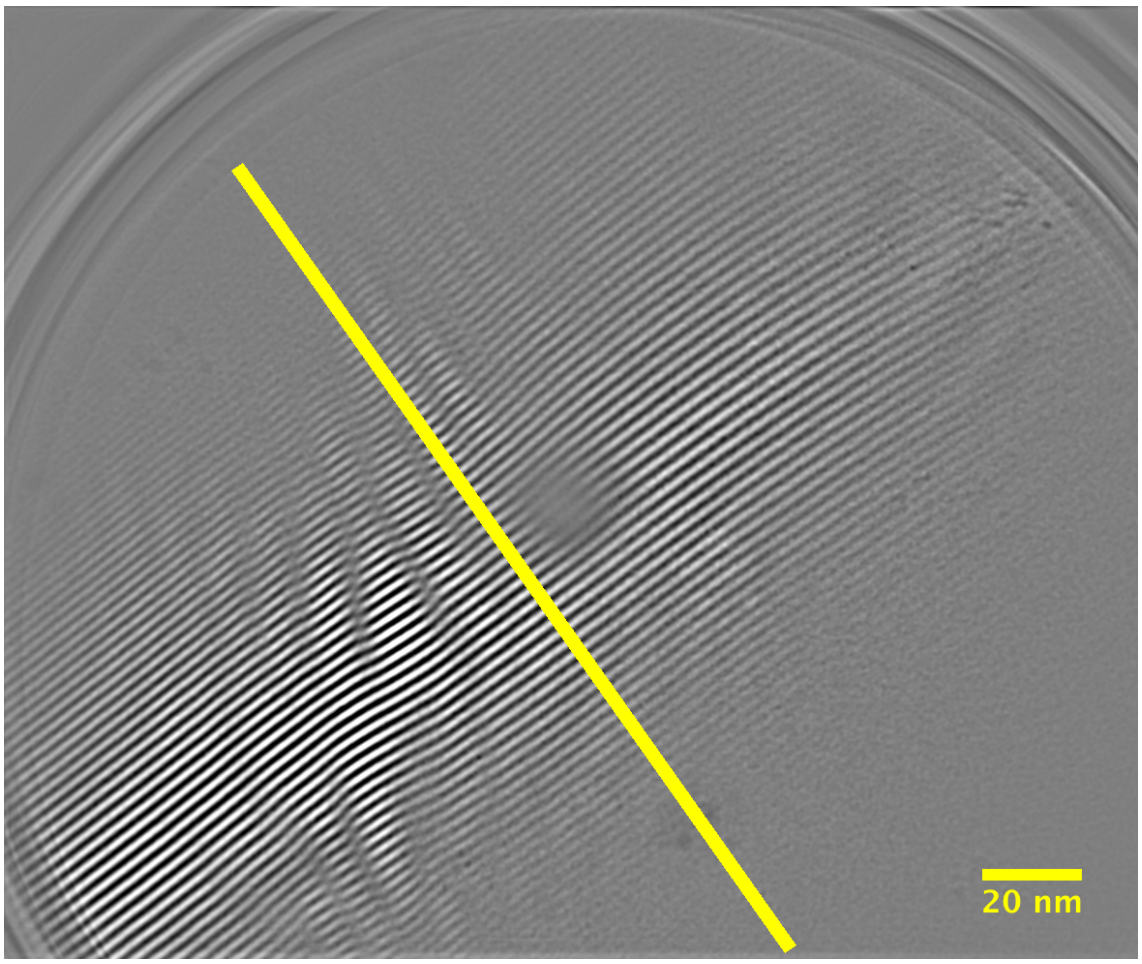

(b) Figure 4.6d high pass filtered to reveal the fringes.

Figure 4.11: The angular width of the SWNT bundle fringe patterns shows that the pattern extends to the limits of the detector. Because of this the coherence angle measurements are actually limited by the detector width, rather than the coherence of the beam.

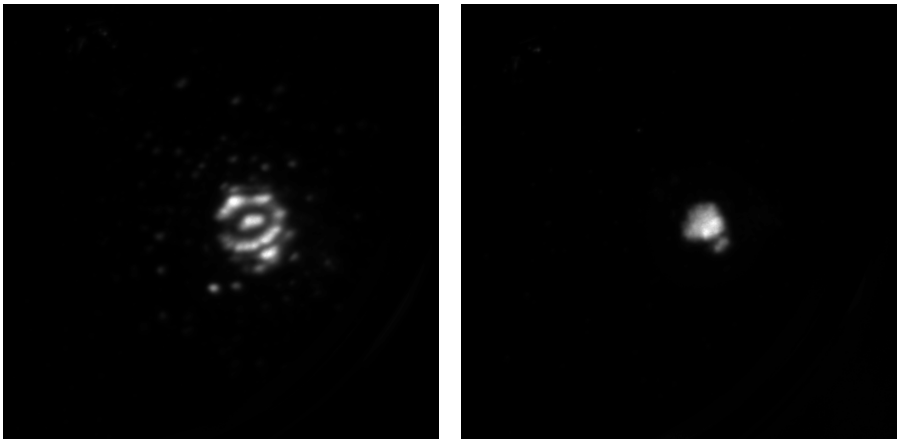

(a) The final FIM image of the tip used in the edge scattering experiments.

(b) The final FIM image of the tip used in the nanotube scattering experiments.

Figure 4.12: FIM images of the nano-tips used in the edge and SWNT bundle experiments. The tip used in the edge experiments ends in a small cluster of atoms. The tip used in the SWNT bundle experiments was sharpened to a single atom. This may be why the coherence angle given by the SWNT bundle experiment is wider than that of the edge experiments.

Chapter 5

LEEPS study of Graphene

5.1 Graphene

Graphene has gained a lot of attention over the past decade, not to mention a Nobel Prize. Graphene is a monolayer of sp^2-bonded carbon atoms, and is essentially the flattened sole ingredient of every fullerene or nanotube. Much like carbon nanotubes, the electronic behaviour of graphene is intimately related to its structure. Originally modelled by P.R Wallace in 1947 [65], graphene has been shown to have many anomalous electronic properties. These include high electron mobilities and zero effective mass charge carriers. Owing to its exotic characteristics, graphene has become a popular theoretical playground as well as the cornerstone of the potential technological revolution of carbon electronics [66]. It was recently popularized by Andre Geim [67], who famously isolated sheets of graphene by exfoliating them from bulk graphite with scotch tape.

Graphene is interesting in LEEPS for a variety of reasons. Primarily, it is a relatively robust and forgiving nanoscale sample to handle in ambient conditions. This robustness makes it an attractive sample to prepare and image with LEEPS. Graphene is also very conductive and nearly electron transparent [68, 69, 70] - even at low energies. For LEEPS this means graphene can function as both anode and an ideal microscope slide [3]. This can solve a problem presented by many samples in LEEPS holography; to obtain enough signal from the reference wave to record a proper hologram, the sample itself has to be very small, and grounded relative to tip. This means that only linear samples suspended across gaps, or small samples protruding from edges can be imaged. Moreover, the electric field around these samples is highly curved which distorts electron trajectories near these samples. This complicates interpretation such holograms, as was the case in Chapter 4. Similarly complicates their reconstruction [58, 55, 57].

By depositing samples on graphene, the samples lie on a grounded plane, removing any drastic potential gradients around them. This has the effect of allowing the electrons to scatter off the sample and travel towards the detector without being steered by the potential gradient due to the sample itself. The effect of a potential due to an isolated nanoscale sample and a sample suspended on graphene is show in Figure 5.1.

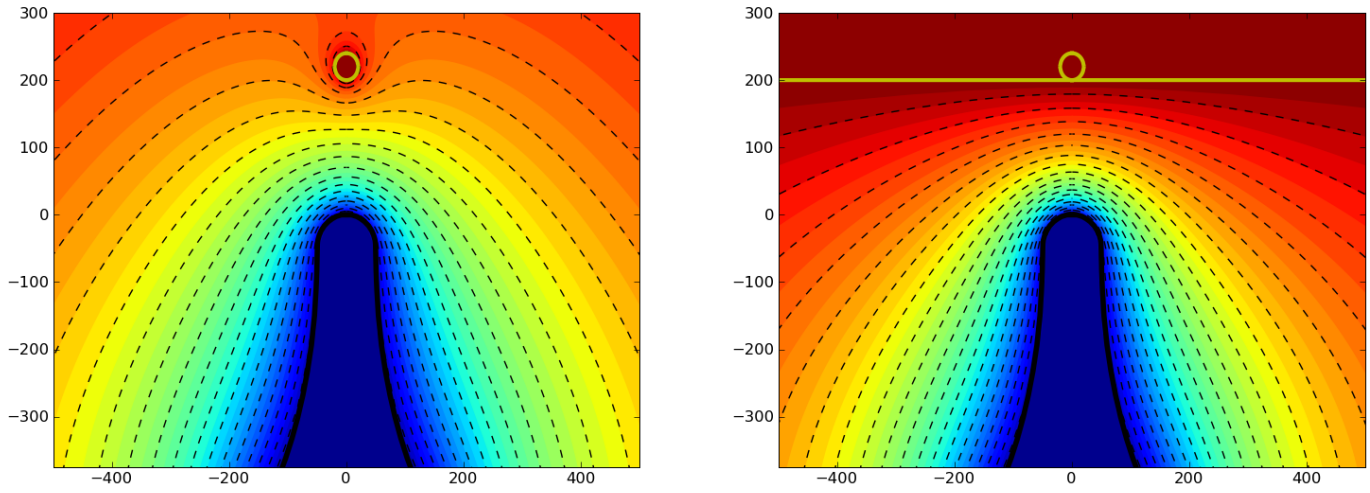

Figure 5.1: Reprinted with permission from [3]. The vertical and horizontal scales are in nm. "The electrostatic potentials due to a grounded discrete nanoscale object (left) and the same object suspended on graphene, modeled here as a thin grounded plane (right). The nanotip appears in blue, the small object is represented as a yellow circle, and graphene as a yellow horizontal line. The distance between tip apex and graphene is 200 nm and the potential difference between them is 100 V. In the first case, electrons emitted from the tip will have their paths distorted by the spatial inhomogeneity due to the field around the object while the grounded plane provides a flat anode mitigating distortions."

5.2 Growth and transfer

Interest in graphene has increased over the last decade, leading to many innovations in the isolation of graphene sheets and the manufacturing of devices with graphene [66, 71, 72]. As a result, many groups world-wide have developed techniques for the growth large sheets of monolayer graphene [73, 74, 75].

Our interest in graphene is as a sample and a substrate for low-energy electron microscopy. Because of the high electron energies used substrates that would appear as transparent in in SEM and TEM, such as thin amorphous carbon membranes, appear as totally opaque in LEEPS. Since it is only a single layer of graphite one atom thick, graphene is far more transparent to low energy electrons than typical EM substrates [3].

Currently, the best way to obtain large area, single-layer graphene is through a CVD process on copper [73]. First, copper foils are cleaned in citric acid, to remove any oxides. The foil is then placed in a low-pressure tube furnace, which is evacuated to a pressure below 50 mbar. Argon is flowed through the tube as the tube is heated to 1000°C. Once at temperature, hydrogen gas is flowed across the foil to remove any native oxide from the copper. Argon is flowed again to purge the hydrogen. Next, methane is flowed across the foil. The methane is meant as a source of carbon: the methane reaches the surface of the copper where it dissociates due to the high temperature of the copper foil and the solubility of the carbon in copper. With enough carbon dissolved in the copper, the methane flow is stopped, while the foil is allowed to cool under argon flow. The carbon precipitates out of the copper and forms graphene islands, which continue to grow as the copper cools. The islands grow into a continuous tapestry of single-layer graphene domains [76].

Much work is ongoing to refine this growth technique, to create higher quality graphene films with higher electron mobilities, fewer defects and grain boundaries. Originally, growth on nickel was the standard, but the high solubility of carbon in nickel made it difficult to control the number of graphene layers during the growth. Copper has largely replaced nickel, since the lower solubility of carbon in copper inhibits multi-layer growth.

Once the graphene is grown, it must be transferred onto a suitable substrate, in our case the perforated SiN windows. Graphene is typically removed from the copper substrate by coating the graphene with an adhesive layer, and then etching away the copper. The graphene can be transferred to an arbitrary substrate by fixing the graphene coated adhesive to the substrate, and dissolving the adhesive [73, 74, 75]. Collaborators at the Naval Research Laboratory (NRL) in Washington, DC have suspended graphene sheets on our SiN windows using this technique.

The transfer is carried out by first removing the graphene from the bottom side of the copper foil. This is done, because graphene grows on both sides of the copper foil, and must be removed on one side, otherwise bi-layer graphene will be transferred in spots. With one side clean, the graphene side is coated with a polymer typically used in photolithography, PMMA. This is the adhesive layer used to stick to the graphene. The copper is then

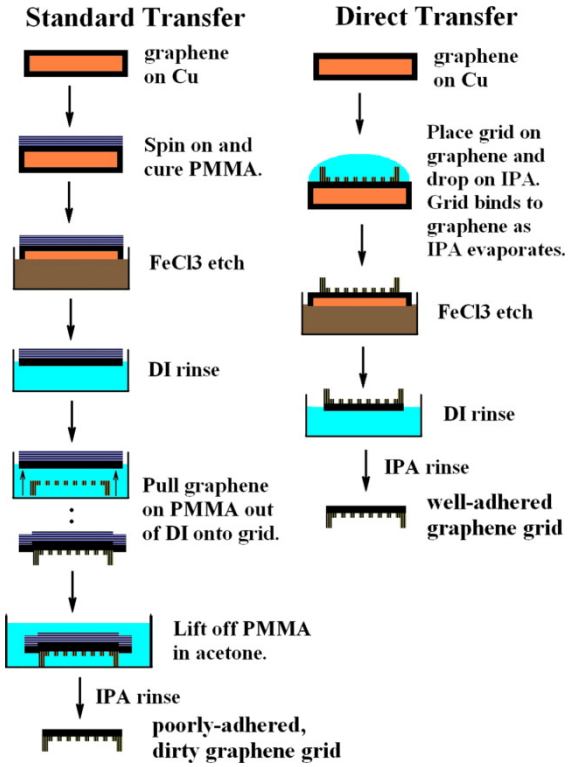

Figure 5.2: Transfer of graphene with and without an adhesive, reprinted with permission from [77].

dissolved in $FeCl_3$, leaving what is essentially a sticker coated in graphene. This sticker is then applied to the metal-coated SiN window, and the PMMA is dissolved away in acetone. What remains is a perforated window where a large percentage of the holes are covered with suspended graphene, like an array of graphene drumheads.

The primary concern with this transfer technique is contamination. In LEEPS, large bands of contamination are seen criss-crossing the sample. These are thought the be left-over PMMA, copper or solvent which adhere to the sample. Moreover, the sample must be heated rather severely to obtain clean graphene, a topic that will be further discussed in Section 5.7. In order to avoid contaminating the graphene with PMMA, transfer techniques must be investigated where the substrate is fixed directly to the graphene coated copper, as shown in Figure 5.2. The graphene coated copper is then placed in the $FeCl_3$ solution, which removes the copper, leaving the graphene attached to the substrate [77].

Both the direct transfer method, and the transfer using an adhesive have been attempted in our lab by graduate student Peter Legg. So far, transfer has been a success, but only in small islands. Large, continuous graphene films have been challenging to achieve and we continue to rely on our collaborators at the NRL for samples. These samples have been characterized in SEM, TEM, X-ray diffraction and Raman spectroscopy, as shown in Figure 5.3.

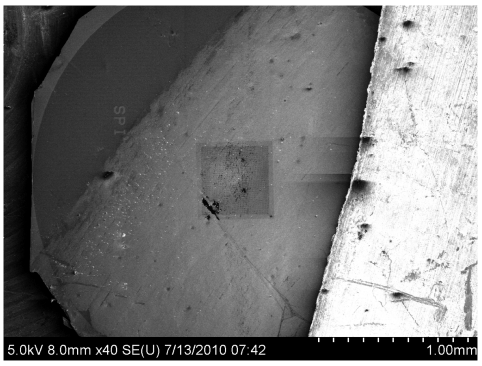

(a) A low magnification view of a graphene coated SiN window. The sheet-like object is the graphene.

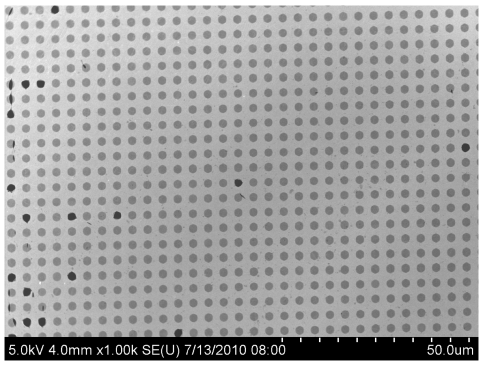

(b) A higher magnification imaged of the graphene coated array of holes.

(c) Electron diffraction image of a single suspended graphene grain, from NRL collaborators.

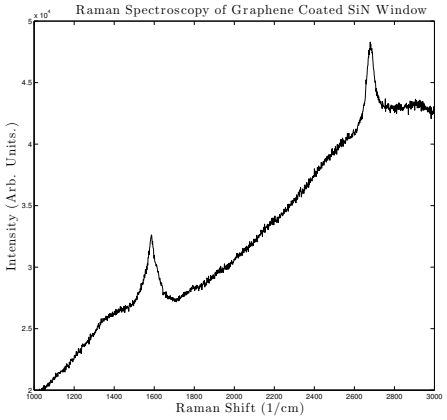

(d) Raman spectrum of the graphene coated window, showing single layer graphene

Figure 5.3: The characterization graphene-coated perforated SiN windows.

5.3 Loading and cleaning samples

Similarly to the nanotube work presented in Chapter 4, SiN windows were loaded into tantalum sample holders before being placed in the load-lock. Once brought into vacuum, the graphene samples were heated in UHV conditions at a variety of temperatures and for a variety of times, in order to study the effect of cleaning procedures on the apparent transparency of graphene, discussed further in Section 5.7. Samples were then loaded into the scanning head, and images were obtained using the method outlined in Section 3.3.

5.4 Domain structure of graphene and dark-field microscopy of graphene

When looking at clean, transparent graphene the most apparent feature are the diagonal lines criss-crossing the graphene, as seen in Figure 5.4 a and b. These lines are contaminants adhered to grain boundaries in the graphene film. The grain boundaries are more reactive than the graphene itself because the chemical bonds for each carbon at the grain boundary are not satisfied. As a result, when contamination is mobilized during the anneal, it mostly adheres to the gain boundaries. This is supported by complimentary studies using scanning-TEM and AFM [76].

The extent to which the graphene is polycrystalline can be visualized in the LEEPS microscope. By approaching the scanning head very near to the MCP (<4 cm) so that electrons scattering at larger angles can be seen, Bragg diffraction can be resolved on the detector. For low magnifications, when a large number of grid-holes are seen in the image, a correspondingly large number of diffraction spots can be seen on the detector, as shown in Figure 5.5. These spots are not peaks as in traditional electron diffraction, but are diffracted images of the graphene covered holes. These are also known as *dark-field* images of graphene.

The relative orientation of the graphene grain controls the orientation which the image is located. In this way, it is possible to obtain a map of the domain structure of the graphene sheets.

Dark-field microscopy gives a different contrast mechanism than the primary image in LEEPS and can be interpreted as a map of the deformation from planar of the graphene sheet. When zoomed in on a single hole (as shown in Figure 5.6), the diffracted spots reveal interesting contrast. Any deflection out of the plane of the carbon atoms in the graphene sheet will change the angle at which electrons are scattered from the sheet. As a result, distortions from the plane appear dark in the diffracted images. Moreover, the different diffracted spots have slightly different contrast, as the direction of the deformation, relative to the diffraction direction, changes the contrast.

Also, the lines of contamination and tears in the graphene sheet are oriented at angles of 60° and 120° relative to one another. This indicates that the crystallographic directions

in graphene dictate the growth and failure in the sheets.

5.5 Corrugation of graphene sheets

When magnified further, images of graphene sheets reveal fine corrugations, as shown in Figure 5.7a. The wavelength of the ripples was determined by computing the average radial distribution function (RDF) of the dark features. As a control, we compared this result to the RDF computed over vacuum. Using this method, the wavelength of the rippling was determined to be peaked around 26 nm. This is shown in Figure 5.7b. This is in agreement with published measurements from experiment [78, 79, 80] and analysis from theory [81, 82]. This corrugation has many possible origins, including: strain induced at the boundaries of the sheet [82, 83]; temperature induced motion [81]; and the adsorption of impurities (especially OH molecules), which may locally distort the carbon lattice [84].

The study of the origin of these ripples is an ongoing goal of this research. Changes in the scale of the corrugation will be probed by: dosing the graphene with different molecules, with varying dipole moments; imaging graphene at different temperatures; and by suspending graphene across gaps with different shapes and degrees of roughness at the edges.

5.6 Interaction thickness of graphene

LEEPS provides a direct measurement of the attenuation of the low-energy electron beam by the clean graphene sheet. The effective attenuation length l_{EAL} for a material includes the various mechanisms for elastic and inelastic scattering in the material that attenuate the intensity of the beam. Values for EAL for various materials are available from NIST databases [85]. These Figures were determined experimentally, using a variety of techniques including x-ray photoelectron spectroscopy.

Graphene is a very thin carbon film, and for such films the l_{EAL} is roughly 5 Å for energies ranging from 100 to 200 eV. Extrapolating a continuum model to the single atomic layer thickness, the intensity of the electron beam that makes it through the graphene sheet varies according to the equation:

$$I(h) = I_o \exp\left(-h/l_{EAL}\right), \tag{5.1}$$

where I_o is the intensity of the incident beam and h is the thickness of the sheet.

From experiment, it is observed that the transparency of a single sheet of graphene is 74%. When a thickness h of 1.46 Å, corresponding to twice the covalent radius of sp^2-bonded carbon, is applied to equation 5.1, a value of 75% is obtained for the transparency. This is noteworthy when compared to the expected transparency when assuming the interaction thickness of graphene is equal to the graphite inter-layer distance of 3.35 Å. This distance leads to a transparency value of 51%, well below experimentally observed value.

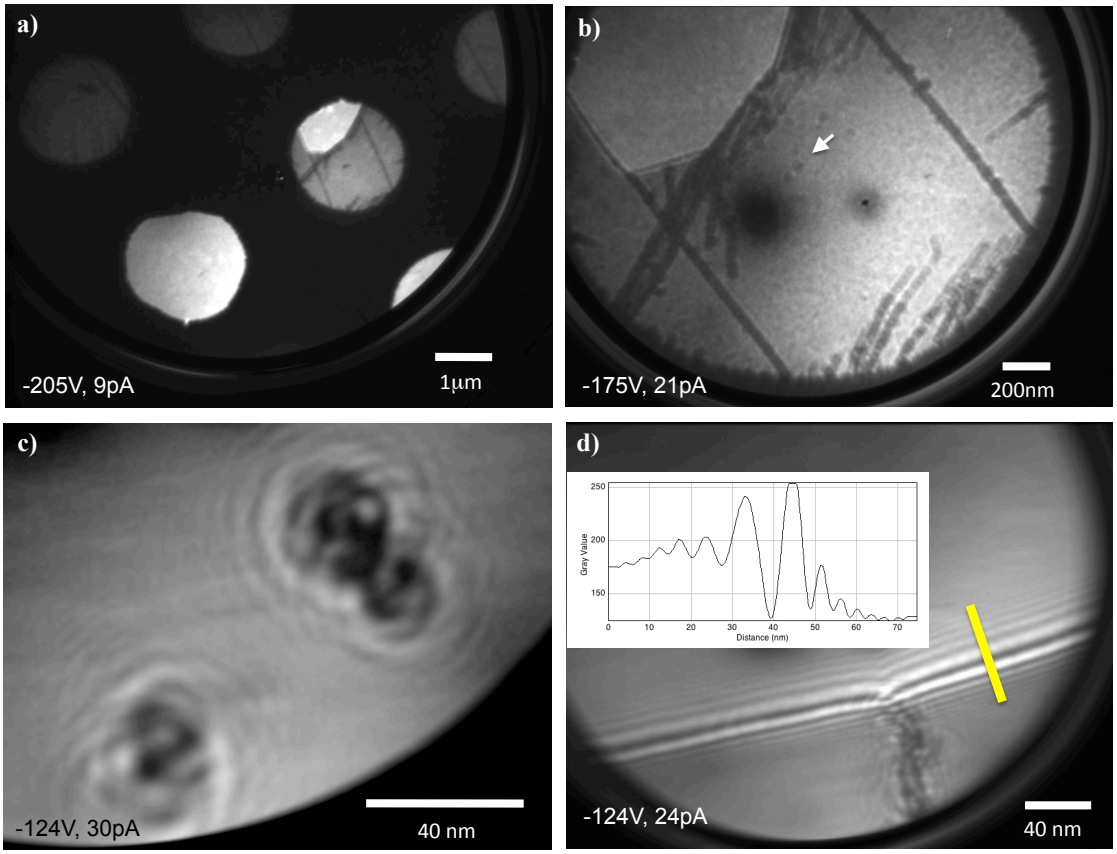

Figure 5.4: Reprinted with permission from [3] LEEPS "Images of graphene a) An image of a portion of the graphene-coated silicon nitride grid. The grid is perforated by 2 μm holes on a 4 μm pitch. The majority of the holes are covered entirely with graphene (as in the top left), some are partially covered with graphene (top right) and a few are totally uncovered (bottom middle). Note the straight lines crisscrossing the image, these are thought to be grain boundaries and/or wrinkles in the graphene. The lines are evidently decorated by leftover contaminants. b) A zoomed-in portion of the partially covered hole from (a). The lines are clearly visible. The uncovered portion is in the top left of the image. Note the diagonal lines and what are evidently folded back portions along the hole. Also of note is the faceted nature of the edges of the hole. c) A zoomed-in portion of the area indicated by the arrow in (b). These objects are small enough that they only partially scatter the electron beam. The interference pattern between the scattered and unscattered portion of the beam forms a hologram. d) Many highly visible fringes appear along the edge of the graphene sheet as we zoom in further. The inset is a profile along yellow line. Also, the interference due the diffraction around the contaminants along the lines becomes more visible. The voltage between the sample and the tip, along with the emission current is displayed in the bottom left corner of each image."

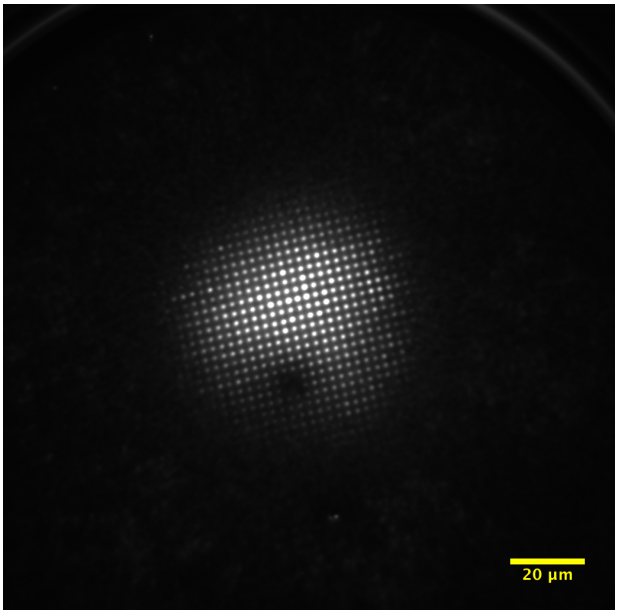

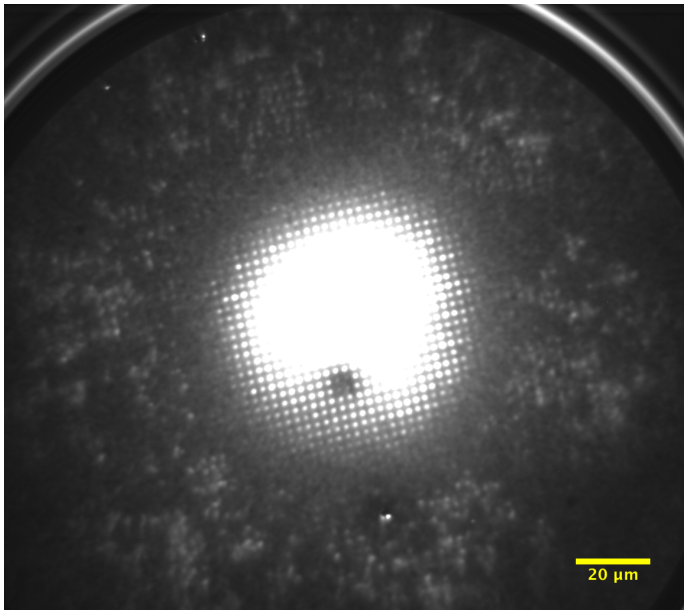

Figure 5.5: Bragg diffraction for low magnifications in LEEPS microscopy: Each bright spot corresponds to a graphene covered hole in the grid. When enough emission is collected, diffraction spots corresponding to each graphene domain covering the gridholes is visible along the periphery of the image. These spots are localized in 6 symmetric patterns, corresponding to diffraction from the hexagonal lattice of the graphene.

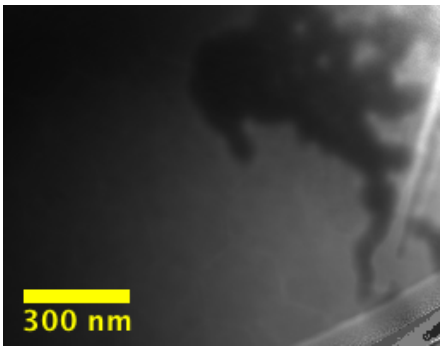

(a) A bright-field image of a graphene coated hole.

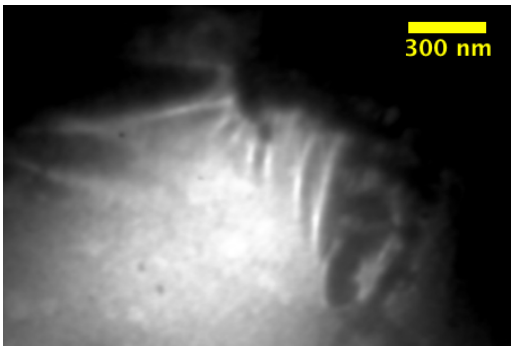

(b) An image of a single dark-field spot.

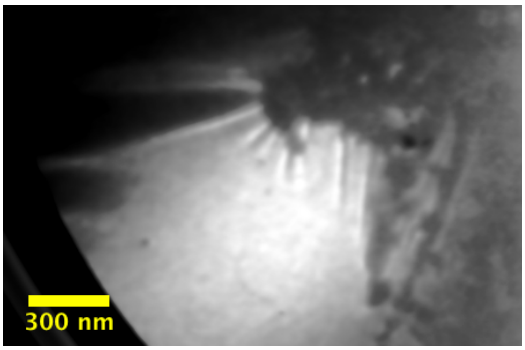

(c) An image of a different single dark-field spot.

Figure 5.6: Comparison of bright-field and dark-field images of the same graphene sheet.The strain on the graphene due to the contamination is clearly visible in the dark-field images. Also there are differences in contrast between the images obtained from different diffraction spots.

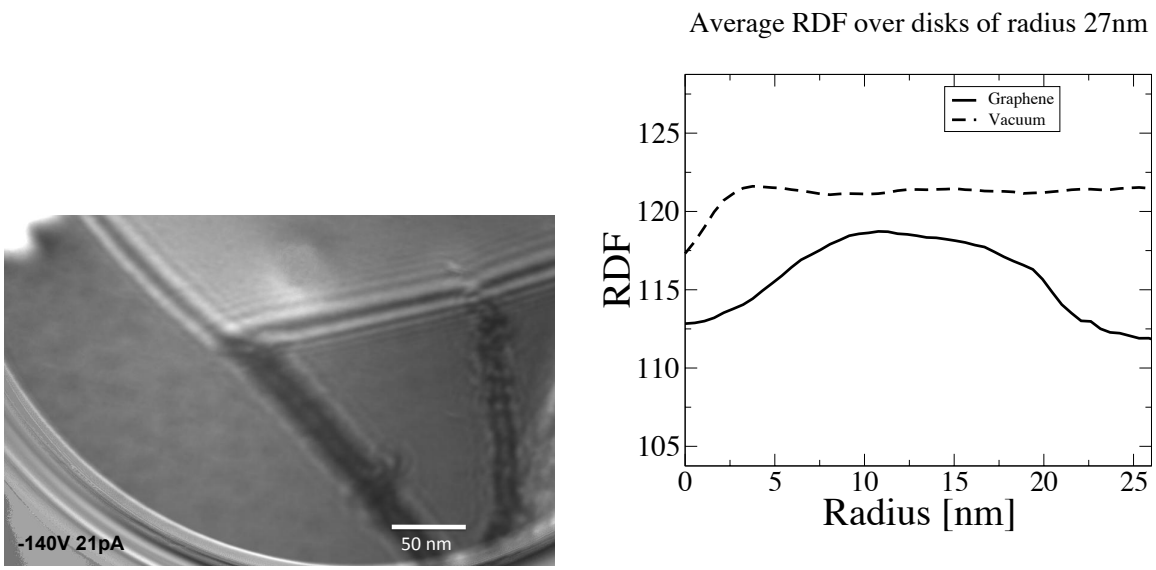

Figure 5.7: Reprinted with permission from [3] "A further zoomed-in portion of the partially covered hole. The graphene sheet appears to have cleaved along a grain boundary or fold, forming an angle of 120 degrees. Also evident is the fine structure of the contamination and the fringes visible from diffraction by contaminants. The graphene itself is rippled. To quantify the ripples, an average RDF of the graphene-covered area and vacuum area are plotted together. The RDF over the graphene is peaked around 13nm, while the RDF over vacuum shows no such structure."

5.7 Contamination of graphene sheets

Due to the low electron energies involved, LEEPS is particularly sensitive to the contamination present on graphene sheets. Several different anneal schedules were performed on graphene samples with varying success. The results are summarized in Figure 5.8. Briefly, anneals at temperatures above 400°C were insufficient to obtain pristine graphene unless for periods of time greater than 8 h. Moreover, attempts use UV/ozone to clean [86] the graphene, in conjunction with the anneal, rendered the graphene totally opaque. The UV/ozone treatment has no effect on the Raman spectrum of graphene, which indicates that the graphene is structurally unchanged by the treatment.

In studies with SEM and TEM, there was no noticeable difference in transparency or quality of the graphene samples, regardless of the anneal schedule. In addition, examining graphene with SEM or TEM causes beam-induced contamination over timescales near the amount of time required to acquire an exposure. This is shown in Figure 5.9. No such contamination, or any morphological changes for that matter, were ever noticed to be induced during imaging with LEEPS.

5.8 STM of suspended graphene

By using LEEPS in conjunction with STM, it was hoped that complimentary images of features on the same graphene sheet could be obtained. The tip was approached over a suspended graphene sheet using LEEPS. The tip was then brought into tunnelling using a typical STM approach. However, STM imaging of suspended graphene proved difficult. As the tip approached the sample, the tunnelling current would suddenly jump form the baseline reading to a value saturating the current amplifier.

By approaching slowly at a relatively high voltage (+4 V), a controllable tunnelling current between tip and sample was achieved. Once in tunnelling distance, the current and voltage were slowly tuned to the desired parameters without crashing the tip.

While STM images (shown in Figure 5.10) approach nanometre resolution, it was impossible to resolve the graphene lattice. This is most likely due to thermo-mechanical motion of the suspended graphene sheet itself. The amplitude of the motion is estimated to be on the order of an Angstrom [87]. This motion is sufficient to wash out any atomic-scale detail in the images.

It impossible to be totally certain that the tip landed on the suspended sheet, and not the frame of the grid. Areas larger than the size of the an individual hole in the SiN membrane were scanned, in the hopes of resolving the edge of the hole, but no such definition was found. The 100 nm thick Au/Cr coated SiN membrane itself may not be rigid enough for good STM scanning.

The lack of rigidity of the graphene substrate is also a concern for LEEPS. If the graphene is constantly oscillating with an amplitude on the order to 1 Å, then the resolution of holo-

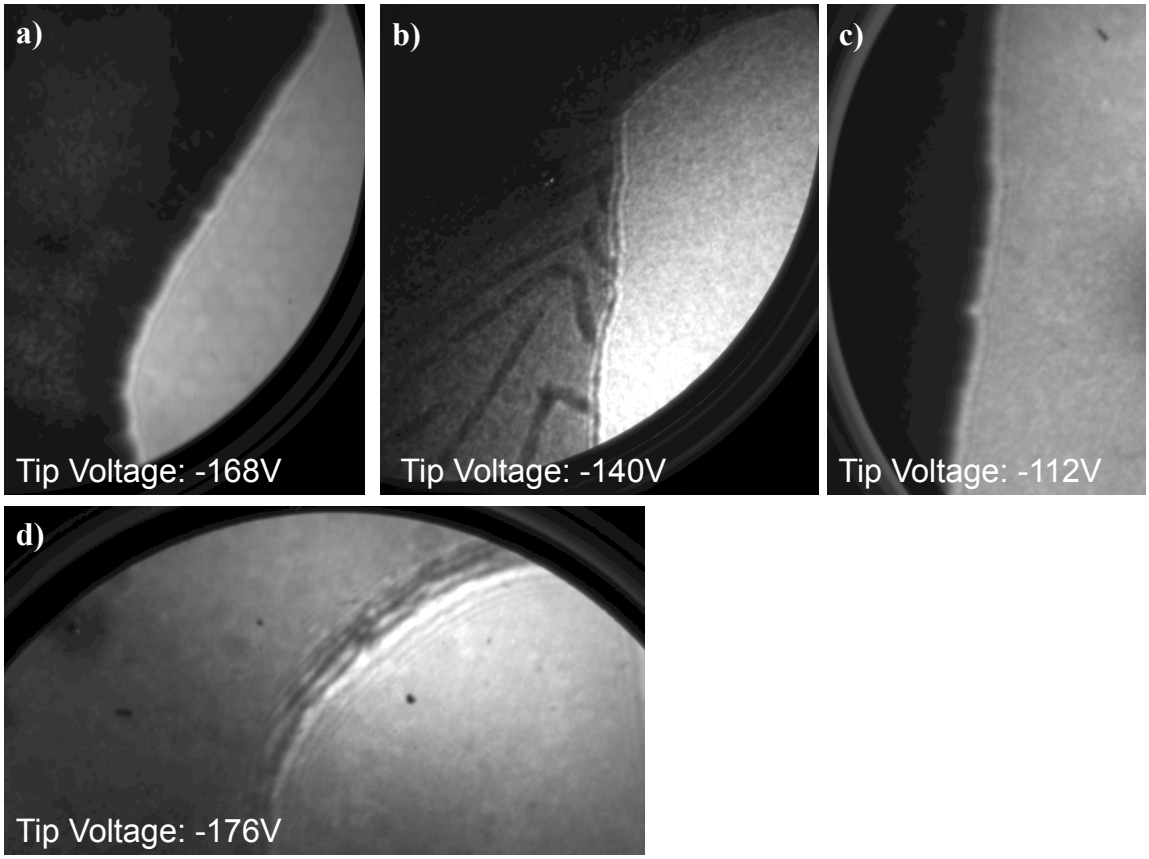

Figure 5.8: Reprinted with permission from[3]: "The effects of contamination on PPM of graphene. The intensity of the electron beam through the graphene sheet is very sensitive to the cleaning process. In each image the graphene is on the left and vacuum region is on the right. The graphene was prepared by annealing in UHV at a) 300^{o}C for 40 minutes (the hexagonal pattern is the structure of the detector) b) 420^{o}C for 40 minutes c) 300^{o}C for 90 minutes and d) slightly above 400^{o}C for 8 hours. The sample in c) first underwent UV/Ozone treatment."

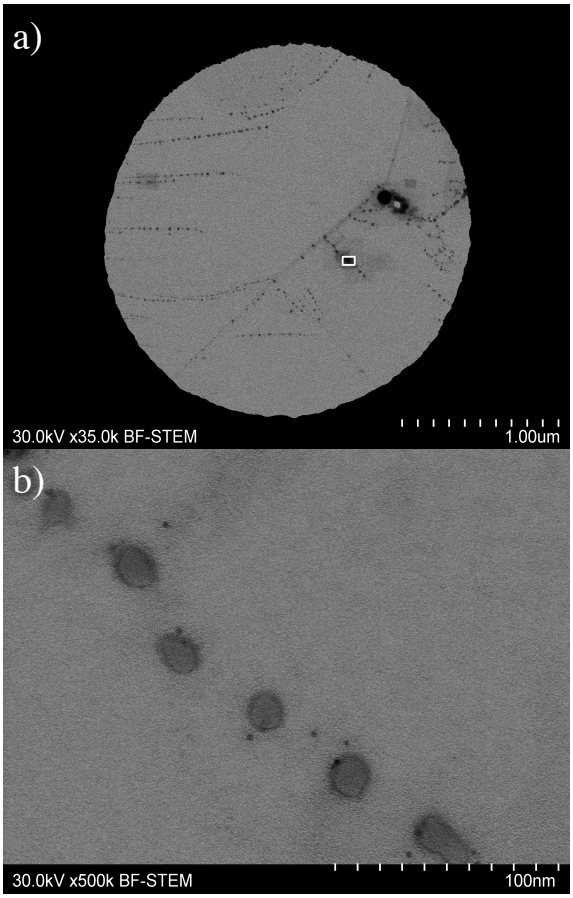

Figure 5.9: Reprinted with permission from[3]: "STEM images of graphene. a) A typical graphene-covered hole in the SiN membrane. The same lines seen in PPM are visible here. The contamination induced by the high energy electron beam creates the many dark squares scattered around the image. No such contamination is visible in PPM. b) A magnified image of the portion in the white square in a). A line of discrete particles (most likely leftover Cu nanoparticles) decorate what is likely a grain boundary."

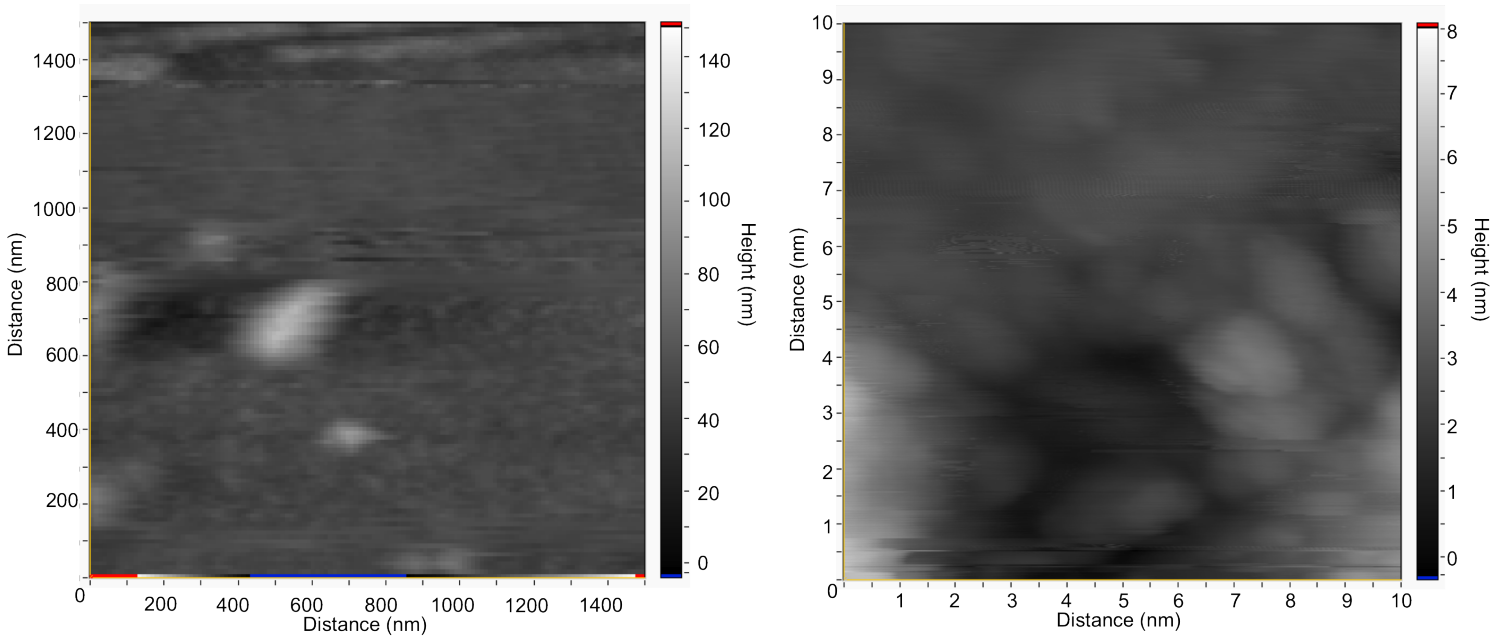

(a) -1.85V, 1.1nA

(b) +1V, 100pA

Figure 5.10: STM images of suspended graphene. The sample bias and current setpoint are listed below the respective figures. Nanometer features of contaminants are resolved but the lattice of the graphene sheet is not discernable.

grams of objects suspended on graphene, or graphene itself, will be limited by this motion. In the future, more rigid substrates with narrower gaps for suspending graphene should be used in order to have a chance at STM imaging approaching atomic resolution. Atomic resolution STM will provide an excellent comparison for reconstructions in holography and is an indispensable tool for future studies.

5.9 Scattering off graphene edge

The edge of a graphene sheet makes an interesting sample for many of the reasons discussed in Section 3.5. As the tip is approached, many fringes become visible as seen in Figures 5.11 and 5.12. In this dataset, the image in Figure 5.11a is taken at one tip sample distance, the tip was then moved 250 nm closer to the sample, and each subsequent image was taken at that tip-sample separation. Each of the subsequent images is taken with a different lateral displacement, along a different part of the edge.

The model described in Section 3.5 does not fit the fringe patterns as well as the opaque edge. Good agreement is found for a tip-sample separation of 340 nm in image 5.11a. In subsequent images the tip is known to be 250 nm closer to the sample from the voltage applied to the tube scanner. In these images, the agreement fails for more than a few fringes.

Moreover, the fit yields displacements between 167 nm to 189 nm relative to the first

image, instead of the measured value of 250 nm. Divergence from the model described in Section 3.5 is not unexpected, since that model describes only the interference between the source and the edge. For an opaque edge, this is a good approximation. For a graphene edge, this is a poor approximation, since the semi-transparent sheet of graphene itself will scatter electrons over its entire width, acting as an extended source.

The visibility of the fringe patterns acquired from the graphene edge is far greater than the visibility of the fringes due to the SWNT bundle. This makes intuitive sense, since the thin graphene sheet is more electron-transparent than the SWNT bundle. The dependence of the visibility of the pattern on the calculated tip-sample distances are shown for both the graphene edge and the SWNT bundle is shown in Figure 5.13.

Once again, the width of the pattern and the number of fringes can be used to deduce coherence properties of the tip. Using the fringe pattern shown in Figure 5.14, the coherence angle of the pattern is measured to be $11.5\pm0.5^\circ$. This leads to a numerical aperture of 3.5 ± 0.6 Å and a virtual source size of 2.2 ± 0.6 Å. The tip used in this experiment was the same as that used for the opaque edge in Section 3.5. The coherence angle is greater for the graphene edge than the opaque edge. This makes intuitive sense, because the opaque edge blocks a great deal of the electron wave, leaving less signal to interfere, limiting the width of the interference pattern.

Also, there are 46 fringes visible in this pattern which leads to a ΔE of 1.7 eV, a value in between the SWNT bundle and the opaque edge.

In conclusion, LEEPS studies in graphene demonstrate different imaging contrast than those found in contemporary EM techniques. This contrast enables direct measurements of several properties of graphene that are not directly measurable in other EM techniques, including the corrugation of graphene and the degree of contamination present. Also, no contamination or morphological changes are induced by the beam in LEEPS. In contrast, such deformation and contamination are well documented in SEM and TEM [88, 4]. Graphene also serves as an ideal substrate for LEEPS, removing many of the problems of the interpretation and reconstruction of holograms due to the potential gradient due to discrete nanoscale objects. However, more rigid substrates for mounting the graphene must be explored, in order to limit thermo-mechanical motion. Lastly, the interference pattern due to the edge of a graphene sheet provides a good measurement of the coherence properties of the electron beam, resulting in more well-defined fringes than from a carbon nanotube bundle or an opaque edge [3].

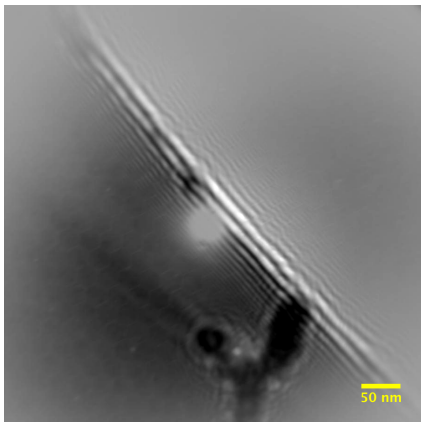

(a) 94 eV, 1.26 Å, 0.05 nA

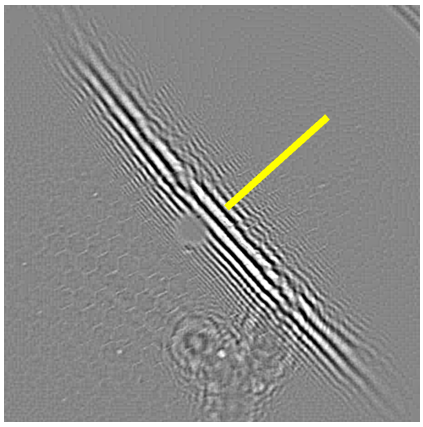

(b) High-pass filtered

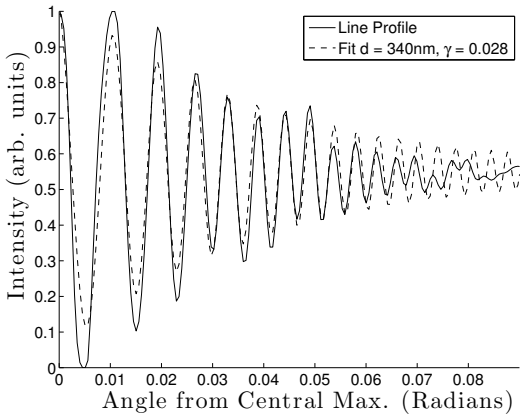

(c)

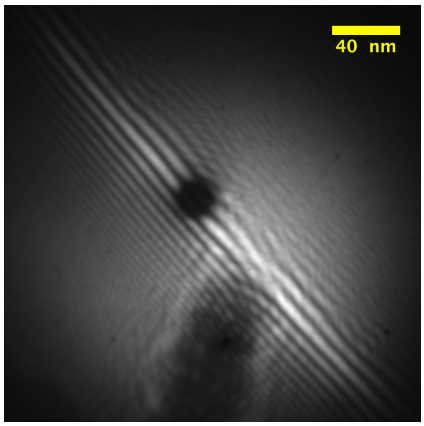

(d) 85 eV, 1.33 Å, 0.12 nA

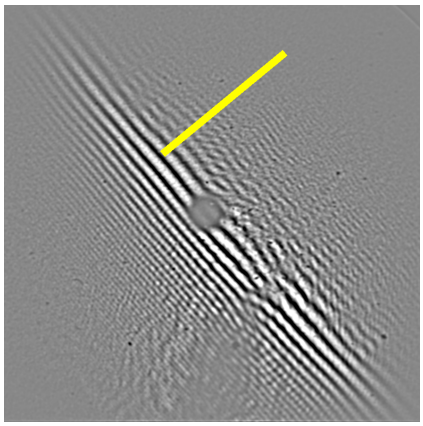

(e) High-pass filtered

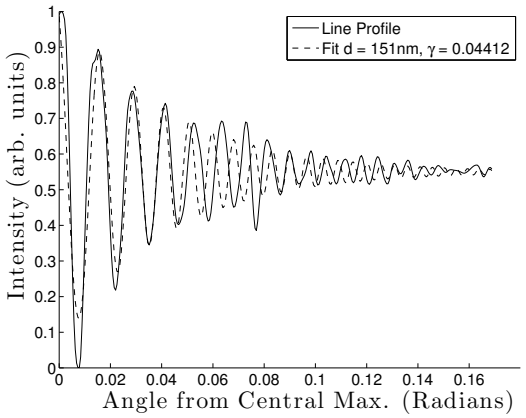

(f)

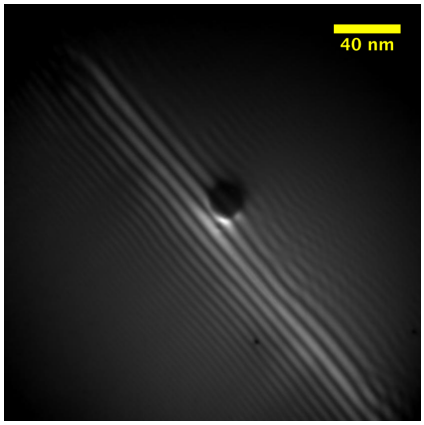

(g) 80 eV, 1.37 Å, 0.23 nA

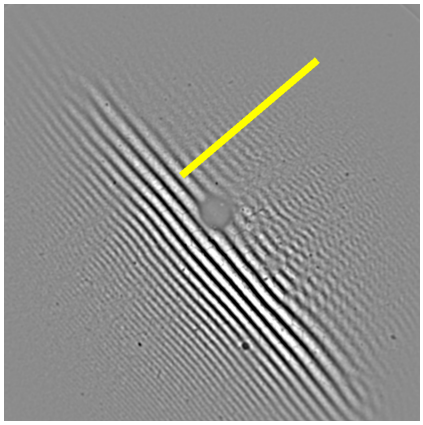

(h) High-pass filtered

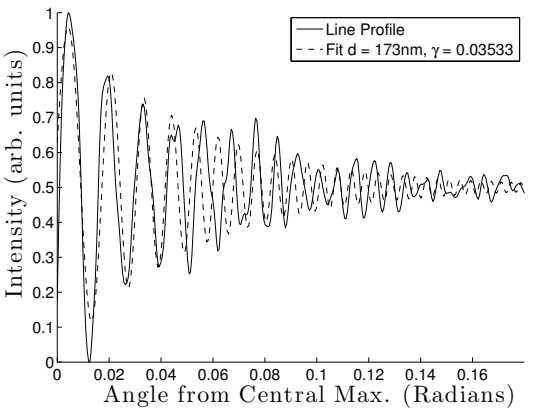

(i)

Figure 5.11: Graphene edge images. Listed below each image are the electron energy, DeBroglie wavelength and emission current. The agreement in (a) with the model described in Section 3.5 is good and yields a tip-sample displacement of 340 nm. In all subsequent images, the tip is known to be 250 nm closer, from the piezo voltages, but the tip-sample distance from the fit does not agree well with this value.

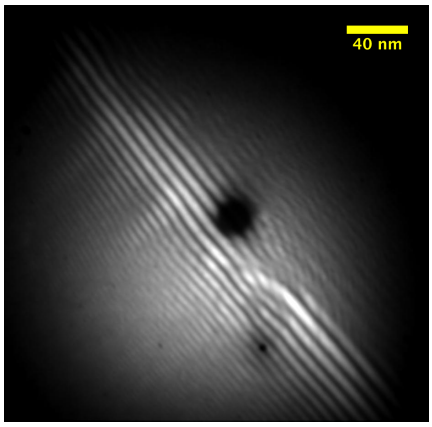

(a) 80 eV, 1.37 Å, 0.19 nA

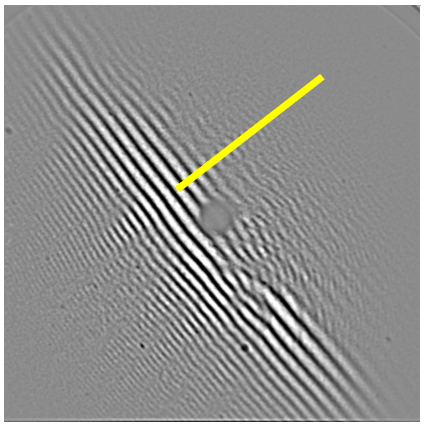

(b) High-pass filtered

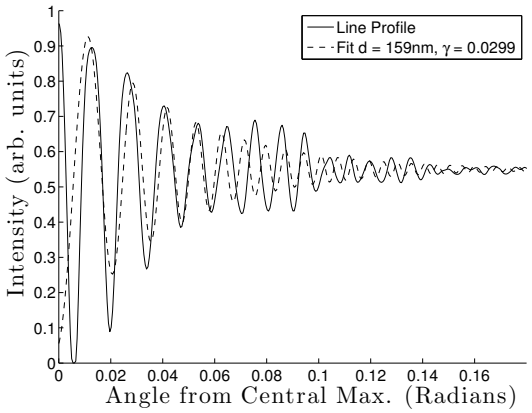

(c)

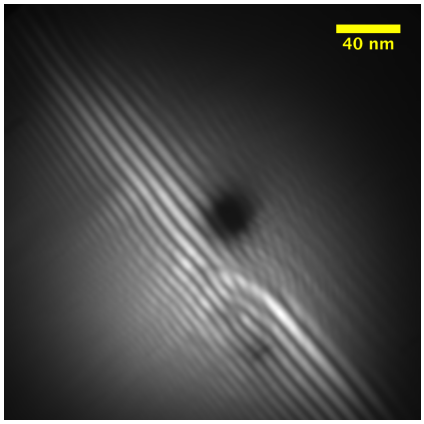

(d) 78 eV, 1.39 Å, 0.23 nA

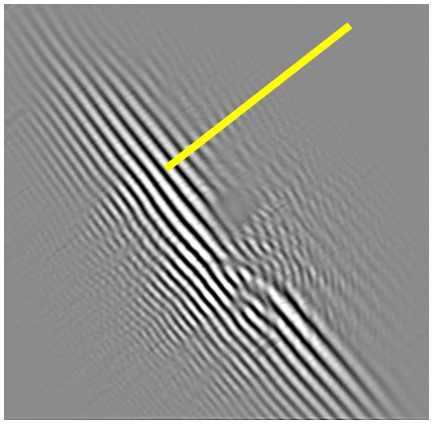

(e) High-pass filtered

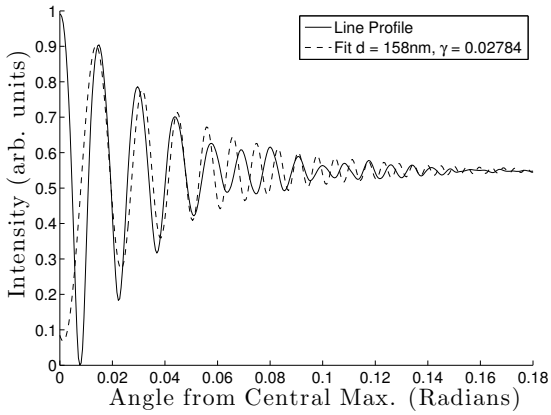

(f)

Figure 5.12: Graphene edge images continued. Listed below each image are the electron energy, DeBroglie wavelength and emission current. These two subsequent images are taken at the sample tip-sample distance as Figures 5.11d and g. Again, neither agree with the model described in Section 3.5 as well as the opaque edge. These images are known to be 250 nm closer than 5.11a but the results of the fit do not agree with this value. Since the graphene edge is transparent, scattering off the portion of the sheet illuminated by the beam contributes to the pattern. In the case of the opaque edge, scattering is isolated to the edge itself.

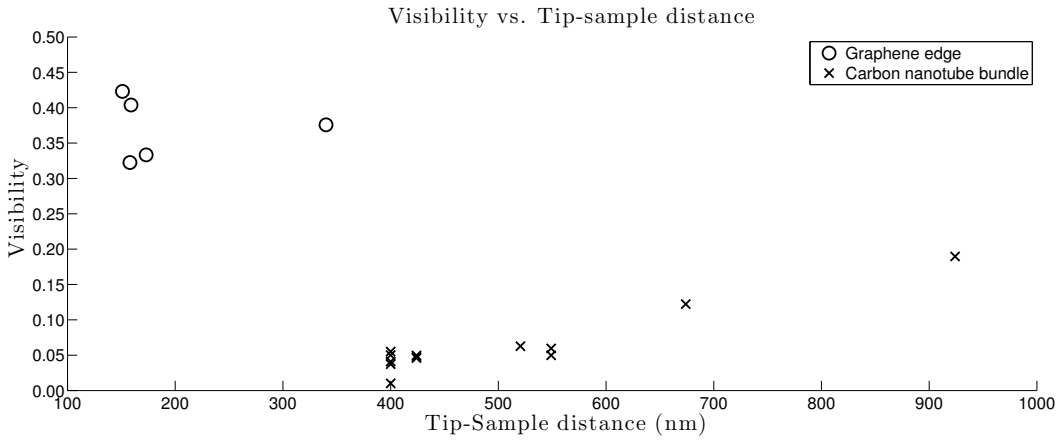

Figure 5.13: Comparison of visibility of graphene edge and carbon nanotube bundle. The visibility of the fringe pattern due to scattering off the graphene edge are much greater than the visibility of the fringe pattern due to scattering off the SWNT bundle. This is thought to be due to the fact that the SWNT bundle is much thicker than the graphene sheet.

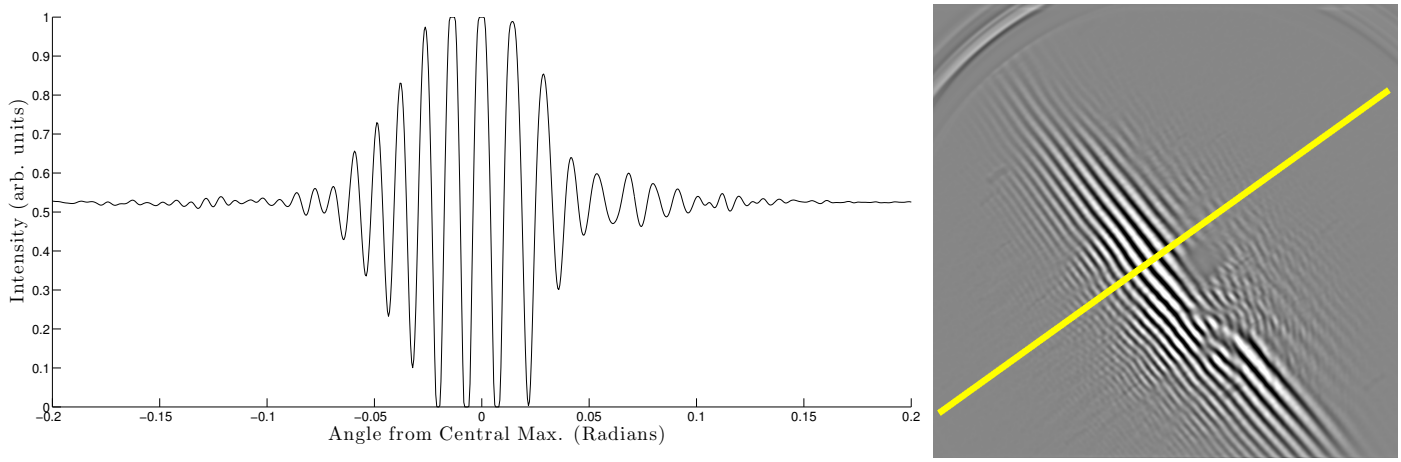

(a) Line profile of fringe pattern from 5.12d.

(b) Region of line profile for (a).

Figure 5.14: By taking a line profile shown in (a), the width of the fringe pattern can be seen. This angular width and electron wavelength are used to calculate the expected resolution.

Chapter 6

Image acquisition and processing

In addition to designing the microscope itself, a suite of purpose-built software also had to be designed. Most importantly, both specific software for acquiring images of the interference patterns, and also software routines for processing the data had to be programmed. In addition to this, software for synchronizing the various applications and organizing the data in a simple fashion had to be designed.

The most important aspect of the LEEPS experiment is the quality of the image. In a hologram, the fine structural information is stored in the intricate fringe pattern. To recover this structural information, the hologram has to be recorded with the highest fidelity possible. In the early days of optical holography, bright, coherent light sources simply didn't exist. Experimenters had to make do with spectral lines from gas-discharge lamps. Early holograms were recorded by exposing a thin object to this radiation, and recording the interference pattern on photographic plates. The low intensity of the beams meant long exposure times were necessary to record a sufficiently accurate hologram. These long exposure times meant that the entire apparatus for recording the hologram had to be exceptionally stable [7]. Any thermal drift or mechanical vibration would wash out the fringe pattern, severely limiting its resolution. Even after the advent of the laser, mechanical stability remained an important concern. An iconic, early three-dimensional hologram of a toy train was only possible by filling the train with epoxy, to stiffen it, and then by gluing it to the track [7].

The LEEPS microscope possesses many of the same challenges of these early holographic apparatus. An image with sufficient signal-to-noise can take minutes to acquire. Drift and instability of the tip and sample can wash out the fringe pattern, obscuring the detail. Fortunately, images are recorded on a CCD camera, not with a photographic emulsion. This allows for some simple correction and post-processing to recover the detailed holographic fringes.

The optical system consists of the tip and the sample, mounted in the scanning head which project a magnified electron image on the chamber mounted MCP. The image is captured by a CCD camera focused on the phosphor of the MCP. This setup is illustrated

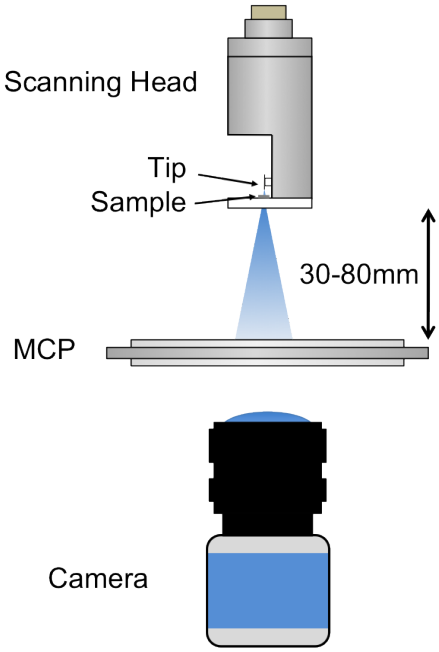

Figure 6.1: A schematic of the optical system of the LEEPS microscope. Tip and sample are held in the scanning head. Electrons are projected from the tip, thought the sample. A magnified image of the sample is projected on the MCP. This image is acquired with the CCD camera.

in Figure 6.1. The most critical portion of the optical system is the tip and sample, because any error in the tip and sample positions will be magnified accordingly.

As mentioned in Chapter 2, great pains have been taken to eliminate any motion between tip and sample. The stability of the tip relative to the sample has been measured to be stable within 0.1 Å in STM. Even still, motion due to drift and creep in the piezo-electric tube scanner is present in the system. Fortunately, if the timescale of the motion is slower than the exposure time of the camera, this can be corrected.

To understand the algorithms for correcting these data it is first necessary to understand the software for acquiring data from the CCD camera. The CCD camera itself is a greyscale camera with 12-bits of dynamic range [89] and a resolution of 1392x1024 pixels. Software, created by Research Associate Dr. Radovan Urban, was heavily modified for use in the LEEPS microscope.

The software (shown in Figure 6.2) was designed in LabVIEW to acquire images from the camera and control parameters such as the exposure time, camera gain and pixel binning for each image. Each individual exposure is not long enough to contain the pattern with sufficient signal-to-noise. Because of this, the software was designed to acquire several images in a running accumulation buffer and display that buffer. This cleans up the image substantially, but any creep in the tube scanner will blur this accumulated image.

Creep is a phenomenon specific to piezo-electric elements that causes them to continue to deform after they have been positioned with an applied voltage. The rate and amount of

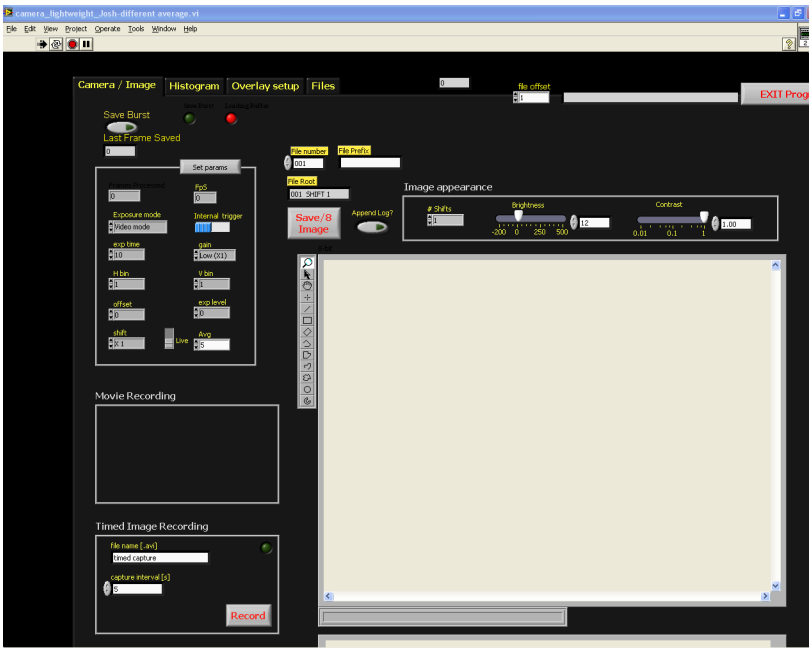

Figure 6.2: A screenshot of the application for controlling the camera and acquiring images.

creep is proportional to the recent history of voltage changes on the element. The greater the changes, the more creep. Using a high gain, that is a large voltage range applied to piezo-electric tube scanner, gives a great deal of deflection range to the tip, but also introduces more creep into the system. This causes the image to drift more over time at a rate of several nm/s. As a result, the tube scanner in the microscope is used over a very low voltage range, between -10 V and +10 V on all axes. This greatly reduces creep. The effect of the voltage range is illustrated in Figure 6.3.

Even still, some deflection of the image always occurs. To acquire an image with sufficient signal to noise to reveal the high order fringes, a great deal of averaging is necessary. Typically 400 exposures are needed to obtain an image of sufficient quality when using an emission current of 0.25 nA. Each exposure takes slightly less than 1 second to process, giving an exposure time of around 5 minutes for the fringe patterns presented in this work. The camera application saves images in two modes: an accumulation of all the images in a buffer of user specified length (by pressing **SAVE IMAGE/8**) and by saving a series of exposures (by pressing **Save burst**), in order to later correct for the drift in the image.

The operation of the camera control application is outlined in Figure 6.4. The application controls the recording parameters of the camera and grabs each exposure and places it into a buffer of user-specified length. The software records each exposure as a 16-bit image (a .tif file) to ensure all 12-bits of dynamic range are recorded without clipping. Each individual exposure does not have enough signal to noise for a truly insightful image, so several exposures are recorded in an accumulation buffer. The software then adds each image in the accumulation buffer to an image for a buffer preview. Once the accumulation buffer is

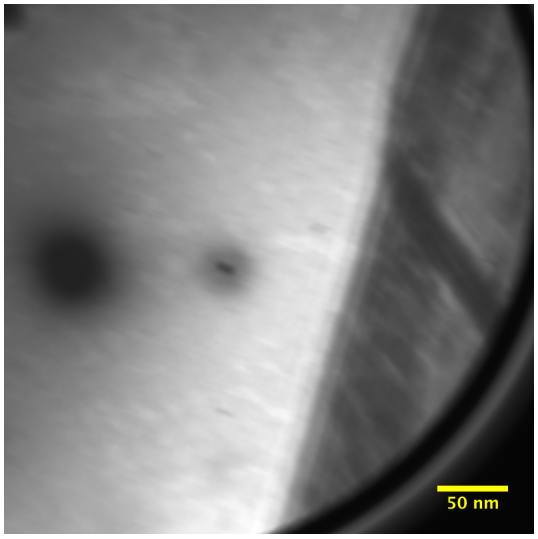

(a) An image made up of 400 exposures averaged and not corrected for drift using *high gain* on the tube scanner.

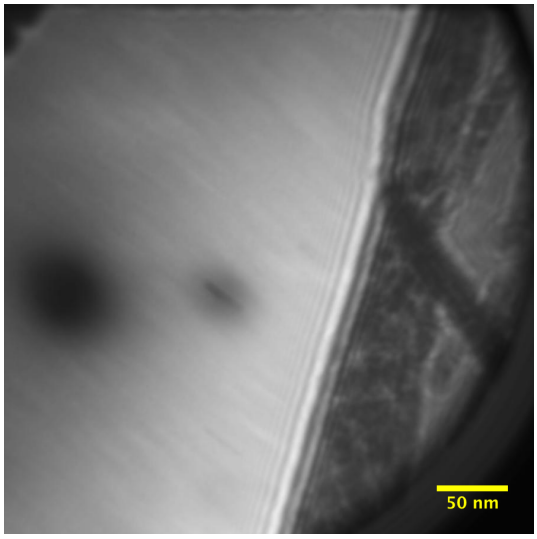

(b) The same image averaged and corrected for drift.

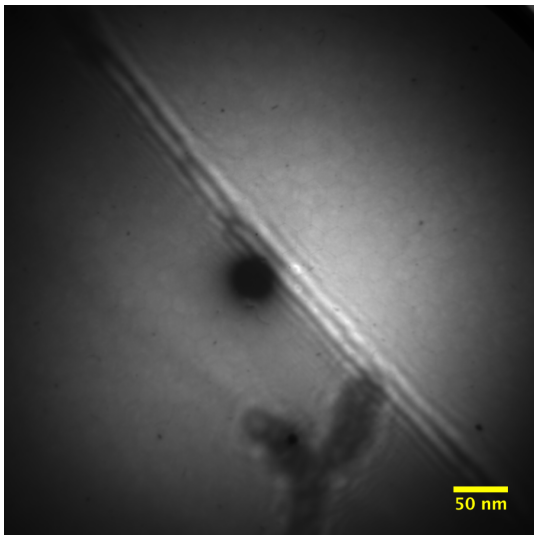

(c) An image made up for 400 exposures averaged and not corrected for drift using *low gain* on the tube scanner.

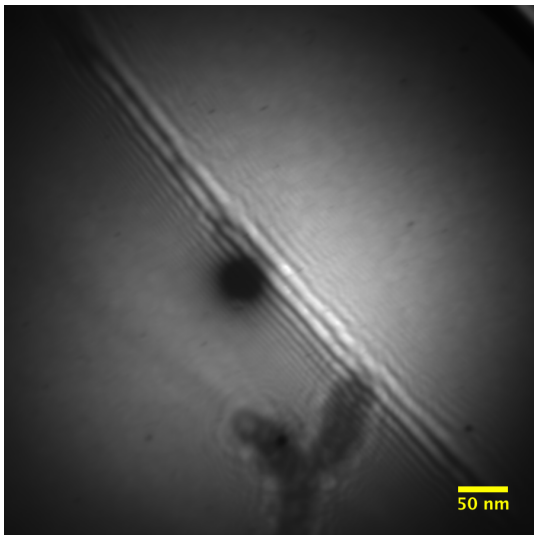

(d) The same image averaged and corrected for drift.

Figure 6.3: The effect voltage gain on the amount of drift present in images.

full, the oldest exposure in the buffer is subtracted from the preview image and the most recent exposure is added on. This preview is a running accumulation. This is the image saved by pressing **SAVE IMAGE/8**.

The application has a window which can be toggled to display either the live preview, which is the latest exposure grabbed from the camera, or the running accumulation. When navigating the tip around the sample it is best to use the live preview mode to locate the area of interest on the camera.

The running accumulation has a unanticipated, but beneficial feature when the preview image becomes saturated. If enough images are added to this accumulation, each pixel will be saturated at the maximum value for a 16-bit greyscale image (65 535). Once the buffer is full, the earliest images are subtracted from this preview image. What results is an image of what features have changed in the time over which the accumulation has been running. This has the benefit of highlighting slow dynamics in the image (drift). This quasi differential mode of imaging reveals fine fringe patterns which would be smeared out in a straight up accumulation. A comparison of an image obtained by accumulation and by this differential mode are shown in Figure 6.5.

Each exposure is stored in memory individually, the contents of the buffer can be written as a series of individual files. This is so each exposure can be used for later post-processing as the accumulated image is blurred due to creep. This is accomplished by pressing **Save burst**.

To facilitate later processing and to keep the data as organized as possible, the software automatically increments the filename of each subsequent image saved. The images are stored in a directory labelled by date. Additionally, there is a field for applying a user defined filename describing the experiment. The software can be used to save either the accumulated image or the individual exposures. When an accumulated image is saved it is saved as:

020 FIM.tif

which indicates that this is the 20th file of the dataset, made of up FIM images. When the buffer is saved, each file is written to a file with the additional description *burst* followed by the exposure number of the accumulation buffer. For example, the burst for the 5th image in a set of images of a carbon nanotube (labelled SWNT) sample with a buffer 8 images long would be saved as:

005 SWNT burst 001.tif
005 SWNT burst 002.tif
005 SWNT burst 003.tif
005 SWNT burst 004.tif
005 SWNT burst 005.tif
005 SWNT burst 006.tif
005 SWNT burst 007.tif
005 SWNT burst 008.tif

This is to keep the data not only organized, but the filenames are used by the software

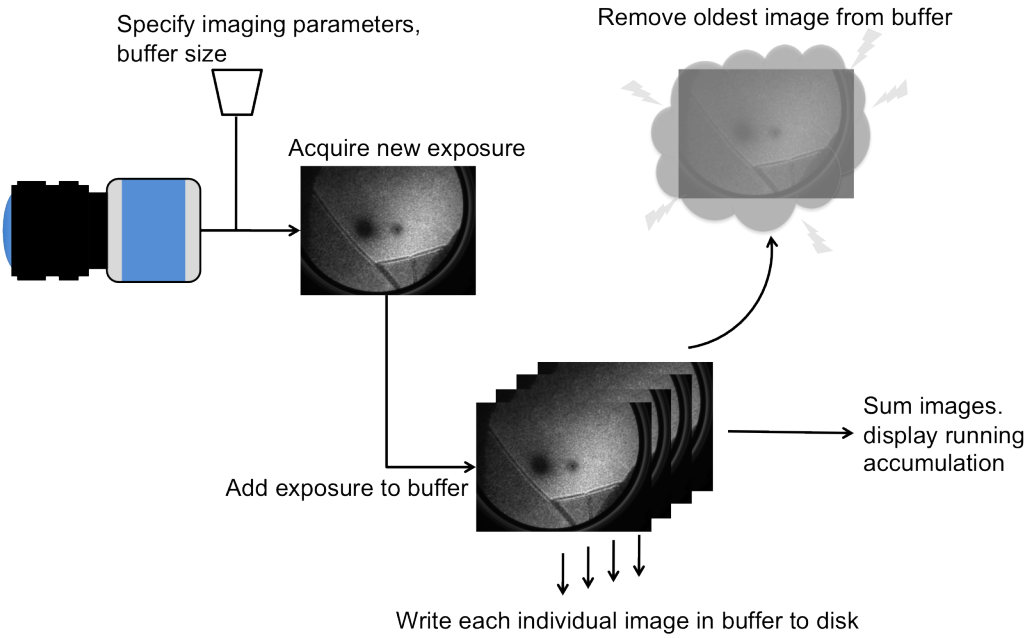

Figure 6.4: A flowchart of the image acquisition software.

for later post-processing.

During a LEEPS experiment the camera software also automatically saves a file with the data saved in the following columns:

image# | *z-piezo* | *y-piezo* | *x-piezo* | *emission-current* | *tip-voltage* | *timestamp*

where the *piezo* columns are the tube scanner displacements as measured by the applied voltage. This file is always saved as *properties.log* and appears in the date-labelled directory. The camera application acquires these parameters from the Nanonis software (which is commercial software for controlling the placement of the tip) and the application for controlling the voltage on the tip, entitled *237controller*. As a result, these programs must be running, and the option *Append log?* must be checked, for the log file to be written.

6.1 Alignment and averaging software

As previously mentioned, the individual exposures containing the fringe pattern need to be added together to obtain an image with sufficient signal to noise. Creep in the scanner will cause the image to drift over the amount of time necessary to acquire enough exposures to gain sufficient signal to noise. To solve this problem an application was designed, again in LabVIEW, to correct for this drift to **align and average** the images to obtain a pattern with much higher signal to noise. A screenshot of this program is shown in Figure 6.6.

The program operates in three modes, *recognize, manual* and *read file*. In recognize-mode, the software automatically checks for a feature in each exposure and aligns the images according to that feature. In manual-mode, the user specifies a value in the x and

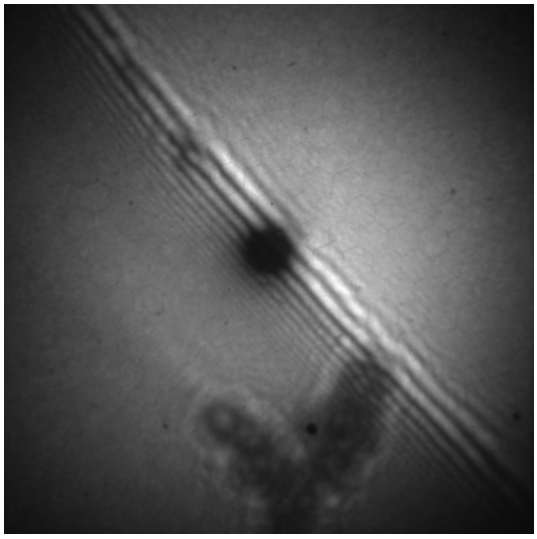

(a) An image obtained by adding together exposures in the accumulation buffer.

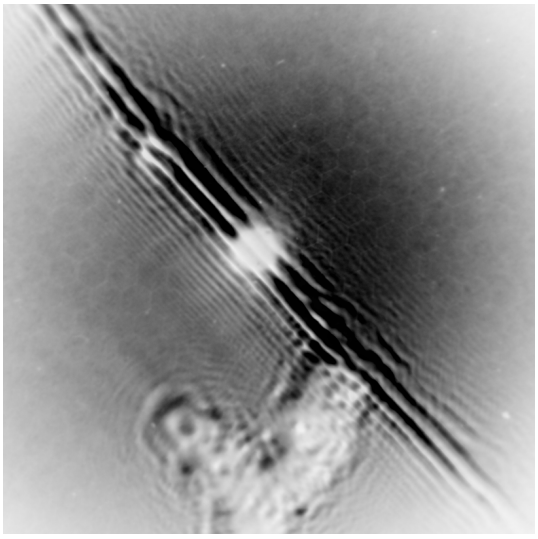

(b) A 'differential' image obtained by subtracting images off the saturated accumulation buffer.

Figure 6.5: A comparison of the normal accumulation imaging mode and the differential mode.

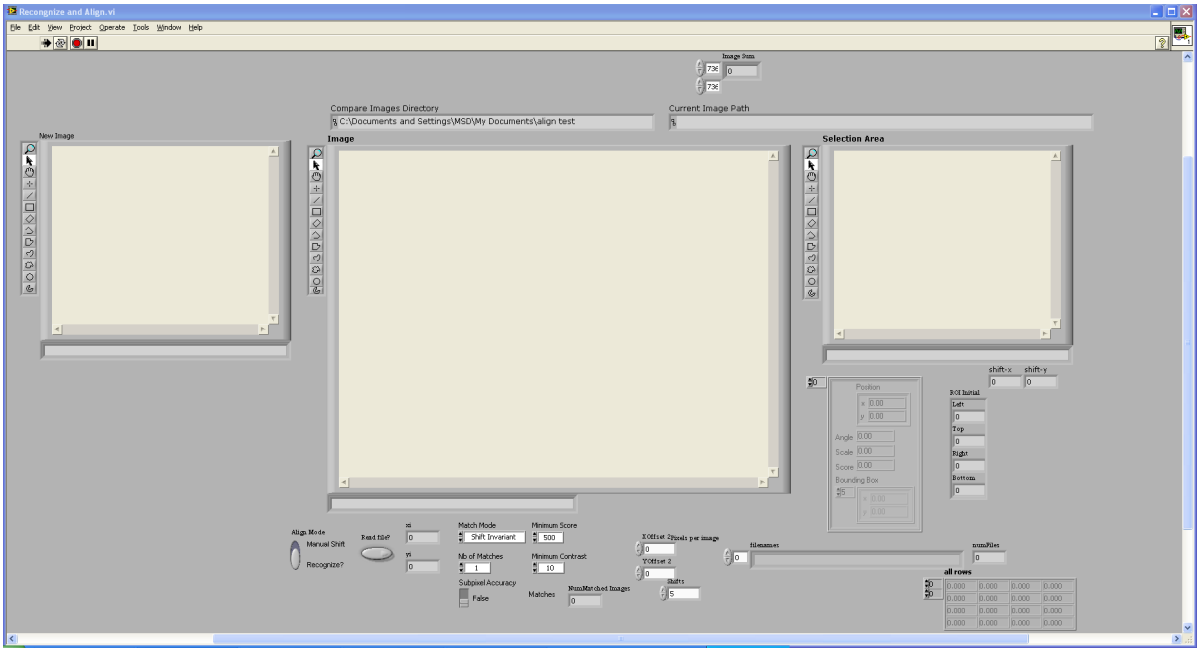

Figure 6.6: A screenshot of the application for aligning and averaging data.

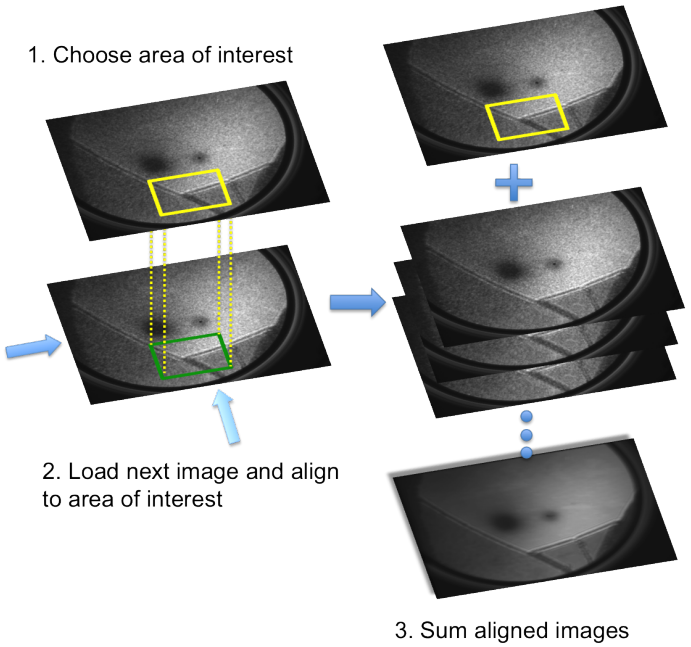

Figure 6.7: A flowchart of the imaging alignment and averaging software.

y directions, in pixels, that each subsequent exposure is shifted by, before being averaged together. In read file-mode, the software shifts each image by a co-ordinate specified in a text-file before averaging the images.

To operate the program in recognize-mode, the series of exposures must be placed in its own directory. The software loads the first image in the series and the user is prompted to highlight an area of interest. Once the area of interest is identified on the original image, the image is converted in to an array, where each entry on the array corresponds to the greyscale value at each pixel. Each subsequent image in the directory is then checked for this area of interest and aligned so that the areas are overlaid. The user can specify a "score" between 0 and 1000 for as a threshold for finding a match, where 1000 is a perfect match. For the software to work correctly, the area of interest must be of high contrast, and not be similar to another feature in the image. If not, the image recognition package will not find the appropriate area in subsequent exposures, or worse will falsely identify and align to different features. A flowchart of this process is illustrated in Figure 6.7.

Once the area of interest has been identified, the program loads the next image, if it finds a region sufficiently similar to the area of interest in the new image, it calculates the amount the area of interest as shifted between the two images. The new image is then shifted by this amount and is similarly converted to an array which is added to the previous array. The program writes the amount the image is shifted by in the x and y direction in a file named *shift.log*. The program does this for each image in the directory, each subsequent match being added to the original array. Once this routine has been done for each image in the directory, the array is divided by the number of images matched and converted again

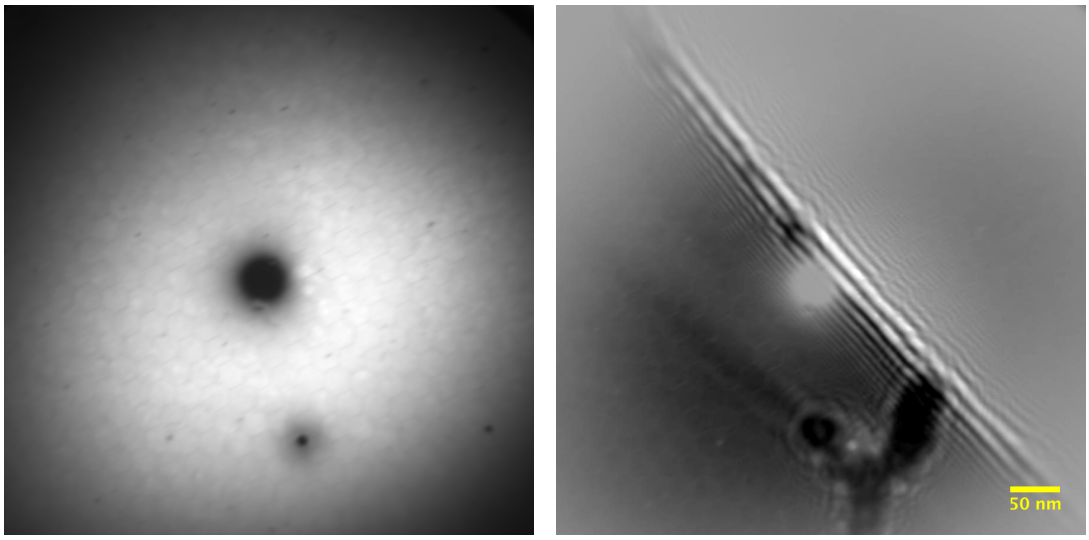

(a) The aligned background image for the image in 6.3d.

(b) Image 6.3d with the background subtracted.

Figure 6.8: The effect of background subtraction on the image.

into an image.

Unfortunately, the LabVIEW routines for image recognition do not work on the 16-bit greyscale images that are saved from the camera. As a result, each image must be converted to an 8-bit image before performing the above processing. However, by reading the shift.log file the program can be re-run in read file-mode to cycle through each image again and align each 16-bit image to obtain an aligned average without losing any dynamic range from the camera.

6.1.1 Block averaging

In some instances, the signal to noise of the individual exposures is not high enough for the software to recognize the area of interest and the align and averaging software fails. To get around this problem another subroutine exists for averaging small blocks of exposures. Although there is drift in the present in the data, it is often not significant over a few exposures. Averaging in unaligned blocks of 5 or 10 exposures will produce images that have sufficient signal-to-noise to be later processed by automatic recognition. Of course there is a balance between the blurring introduced by increasing the length of the block over which un-aligned exposures are averaged and the quality of the aligned average, and the same pattern must be processed with several different parameters to find the correct balance.

The result of the aligned averaging is striking, revealing many higher order fringes that are imperceptible in the non-aligned averages.

6.1.2 Background division

In addition to averaging, the signal can be improved up by removing the non-uniformities in the detector. To do this, a *reference image* of the electron emission without an intervening sample is taken for each dataset. Care must be taken to ensure that the imaging conditions for the reference image are the same as those of the pattern. This means that the MCP voltages, the emission current and the beam alignment must all be the same for the reference image as the pattern. A typical reference image is shown in Figure 6.8a.

There are a few additional challenges associated with this background division, first the intensities of the reference image and the data must be very similar. This is mostly accomplished by taking the reference image at the same imaging conditions, however instabilities in the beam current for either the data or the reference can introduce a variation in the intensity. This can usually be corrected for by equalizing the histogram of both data and reference images.

Another challenge has to do with the alignment and averaging routine used to process the data. While each exposure in the dataset is shifted to align features in the image, defects in the detector are also shifted. If the averaged image were simply divided by the background, the features on the detector that were shifted in the aligned average would not line up with the features on the reference image and not be divided out appropriately. To fix this, the reference image is also taken as a series of many exposures, and aligned according to the *shift.log* file for the corresponding pattern. This "smears" the features on the detector in the exact same manner in both the reference and pattern. The reference image can also be block averaged in the same manner as the data so that both reference and data reflect the same non-uniformities.

The result of background division cleans up the data noticeably, however data with larger lower-intensity regions still have the non-uniformities of the detector in the lower-intensity regions. This is due to the fact that the intensity of the reference image is normalized to the brighter regions. This is evident in the honeycomb pattern still visible in the lower lefthand region of background-divided image in Figure 6.8b.

Chapter 7

Conclusions and future work

The chief motivating drive behind this project was to explore the application of new electron sources to the technique of electron holography. This led to the design of a totally new instrument which also improved upon previous apparatus with greater mechanical stability and magnetic field isolation. But how does this microscope fare against previous instruments designed to perform electron holography?

There are two related, critical measures of resolution for a point-projection microscope such as this one, virtual source size and numerical aperture. Both arguments centre around the principle that the when radiation scatters off an object, the finest structural information about that object is stored in the highest angular components of that scattered wave. In order to obtain a hologram with sufficient resolution, the interference pattern must contain these high-angle portions of the wave. The pattern must possess the highest order fringes possible. To generate such a hologram, the electron beam must be as wide as possible.

The widest coherence angle reported in the literature to date is 3° [29, 90]. The largest coherence angle measured in this work is over 14°. These results are compared in Figure 7.1. Theoretical estimates given by the virtual source size and numerical aperture indicate the expected resolution of electron holography for the first time to **Angstrom** size scales.

Table 7.1 is a summary of the most compelling results in LEEPS microscopy. Where a virtual source size is reported, it is listed. Otherwise, the best estimate for the resolution of the instrument is reported. The work present in this thesis exceeds reported work by every measure: coherence angle, number and fidelity of fringes. Moreover, to the knowledge of the author there are no previous LEEPS studies that have reported on the mechanical stability of their instruments, much less reported stability on the order of 0.1 Å.

7.1 Exploring experimental parameters

7.1.1 Scanner geometry

The most promising results of the fringe patterns presented in this work are not limited by coherence of beam, or the stability of the instrument, but the width of the pattern on

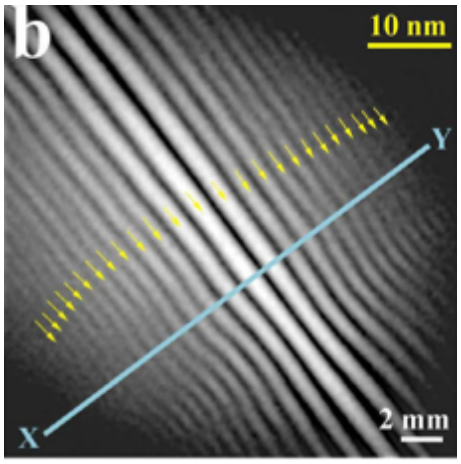

(a) The fringe pattern due to a fully coherent beam reported in [29].

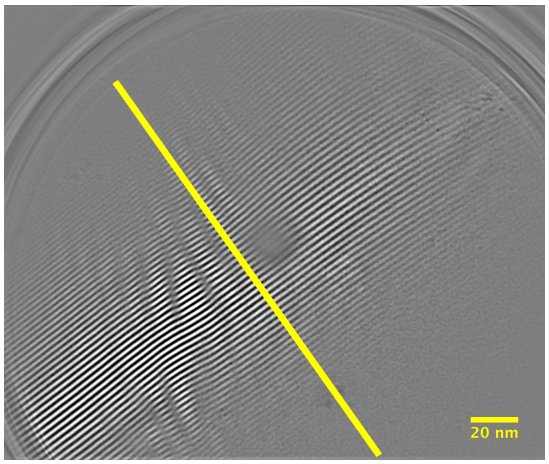

(b) Figure 4.6d high pass filtered to reveal the fringes.

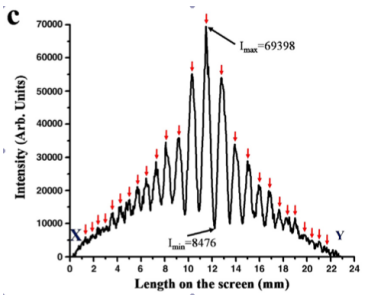

(c) A section of the fringe pattern from [29]. The tip-screen distance in this work is 17 cm, which corresponds to a coherence angle of 3°.

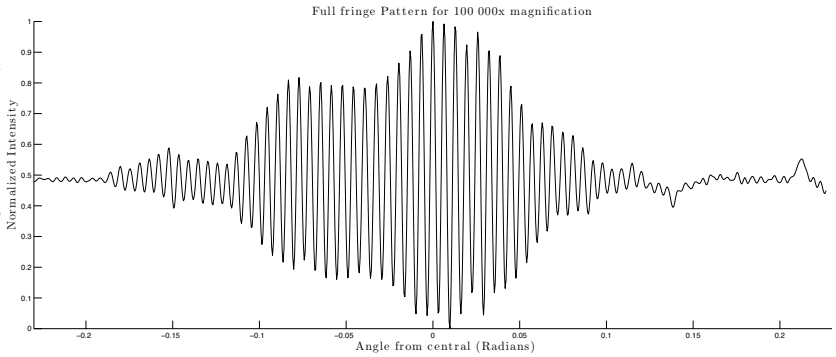

(d) The angular width of the fringe pattern in Figure 4.6d.

Figure 7.1: Fringe pattern presented in this work have a wider coherence angle and a greater number of overall fringes than previous work.

Tip	**Sample**	**Opening angle**	**Virtual source size/Resolution**	**Reference**
N_2-etch, W(100), few-atom tip	*SiN grid edge*	8°	3±0.6Å	*Chapter 3*
N_2-etch, W(100), single-atom tip	*SWNT Bundle*	14°	1.6±0.6Å	*Chapter 4*
N_2-etch, W(100), few-atom tip	*Graphene edge*	11.5°	2.2±0.6Å	*Chapter 5*
Cs coated W-tip FIM voltage pulsing	Tobacco Mosaic Virus	4-6°	<10nm	[14]
50nm W-tip at 78K	carbon nanotube	4°	4-7Å	[31]
Noble metal coated W single-atom tip	carbon nanotube	3°	3.9Å	[29]
W-tip sputtered, annealed	biomolecules	<7°	>1nm	[91]
W-tip field assisted melting	Lacey carbon	4°	>1nm	[34]

Table 7.1: Comparing experimental results for LEEPS microscopes.

the detector. Only part of the electron wave is incident on the detector, as illustrated in Figure 7.2a. Fortunately, there is some latitude for moving the scanning head relative to the detector. To maximize the resolution, the opening angle of the beam should be as wide as possible. As seen in Figure 7.2b, to achieve atomic resolution an opening greater than 30° must be recorded on the detector.

The beam-angle incident on the detector is limited by the width of the detector and controlled by the position of the scanning head. The scanning head can be placed so that the sample is anywhere from 0.5 cm away from the detector to nearly a metre.

In order to maximize the opening angle of the beam on the detector, there are several other concerns besides simply placing the scanning head as close as possible to the MCP. Namely, is the resulting pattern large enough to be recorded by the detector and resolved by the camera? This can be determined by simple geometric arguments. The resolution of the instrument depends on the opening angle of the beam incident on the scanning head and is related to the tip-detector distance D by:

$$\text{Virtual Source Size: } R = \frac{\lambda}{\pi \tan^{-1}(l/D)} \tag{7.1}$$

$$\text{Numerical Aperture: } R = \frac{\lambda(D^2 + l^2)}{2l^2} \tag{7.2}$$

where λ is the wavelength of electrons and l is the radius of the detector, 13.5 mm. Considering this, the effect of tip-screen distance D on the resolution is shown in Figure 7.3a.

The closer the scanning head is to the MCP, the lower the magnification for a given tip-sample distance. Remembering formula 1.1: $M = D/d$, where d is the tip-sample distance. In order to achieve higher magnifications, the tip will have to be closer to the sample, than if the scanning head were farther from the MCP. Also, the resolution of the MCP begins to become a factor as the magnified image becomes smaller on the screen. Enough resolution is required to make out the fringes in the hologram. To resolve 1 Å easily on the detector, it should make up a distance of 0.1 - 0.2 mm on the detector. This calls for a magnification factor, M on the order of 10^6.

As described in chapter 3.5, the angular pitch, α_p, of a fringe pattern for a source scattering off a generic object at a distance d is on the order of λ/d. The distance of this pitch P, of the pattern on the detector is related to the angular pitch α_p simply by $\tan(\alpha_p) = P/D$. For a constant magnification M, d can be eliminated, yielding an expression relating the pitch to D and λ:

$$P = D \tan\left(\frac{\lambda M}{D}\right) \tag{7.3}$$

To observe an emission angle of 30°, the scanner must be less than 2.5 cm from the detector, which leads to a tip-sample distance of 25 nm. In order to probe size scales on the order of 1 Å wavelength, 100 eV electrons must be used. The pitch of the fringe pattern

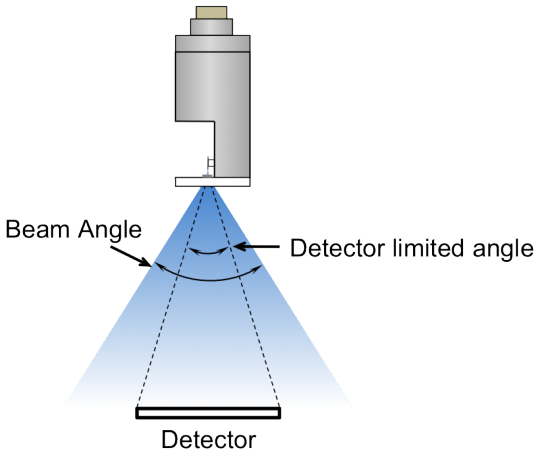

(a) The angle beam incident on the detector limits the resolution.

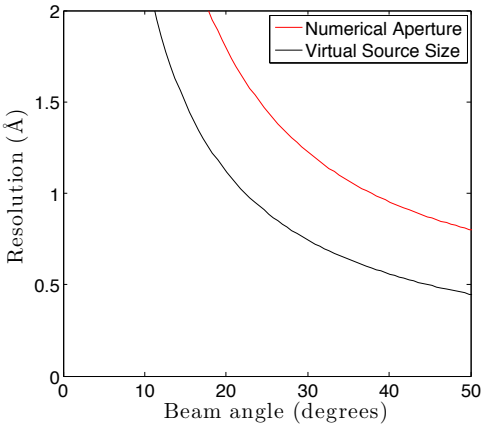

(b) The relationship between the resolution and beam angle.

Figure 7.2: The interplay between the position of the scanning head and the width of the pattern on the detector limits the resolution by limiting the angle of the pattern recorded by the detector.

generated by using a geometry sufficient to obtain atomic resolution is calculated in Figure 7.3b and is easily visible on the camera at around 120 μm. Since the pixel size on the MCP is around 40 μm and features on the order of 100 μm are routinely resolved in experiment.

7.1.2 Tip shape and emission current

While LEEPS is technically a lens-less technique, the tip serves as a lens in a very practical sense. As illustrated in Figure 7.4, the shape of the tip defines the numerical aperture of the instrument as well as the spatial and energetic coherence of the beam. Designing and building the appropriate tip is just as important as crafting the perfect lens in a conventional microscope. The geometry of the system, detector and scanning head, alone is flexible enough to obtain Angstrom resolution. However, there are some additional complications with obtaining the desired resolution, related to the fact that the sample serves as the anode. The higher the magnification, the closer the tip and the more intense the field around the tip, for a given voltage. As a result, the structure of a tip which provides a coherent beam at a desired voltage for the appropriate tip-sample separation must be designed.

The 25 nm distance necessary to achieve Angstrom resolution is an order of magnitude closer than experiments carried out in this work. Since the current emitted from the tip increases exponentially with field [92], the current drawn by the tip at 25 nm may be a few orders of magnitude higher than the current drawn at 250 nm. This raises important questions about the source. Will the beam remain coherent at currents greater than a few nA? How will the coherence angle depend on the local nanoscale shape of the apex of the tip?

Experiments in this work have demonstrated a high coherence angle at emission currents

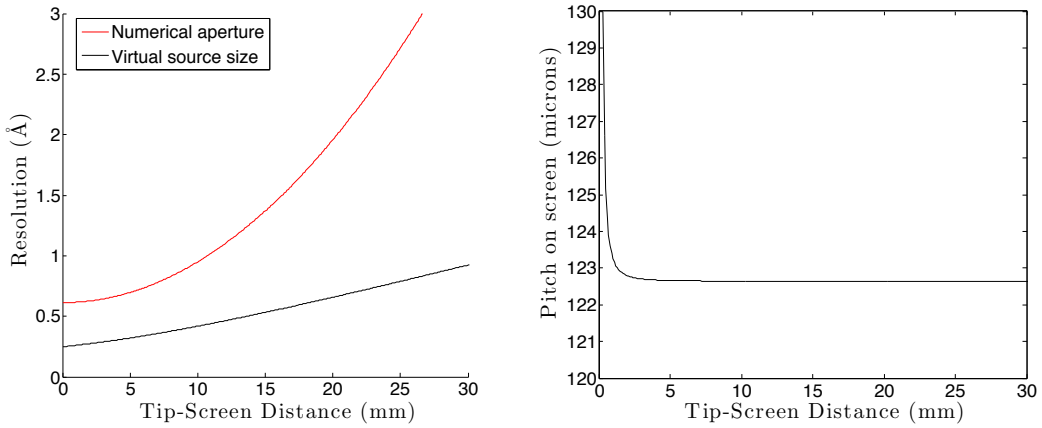

(a) The relationship between resolution and the tip-screen distance.

(b) The relationship between fringe width and tip-screen distance.

Figure 7.3: The dependence of resolution and the effect on the fringe pattern of changing tip-screen distance.

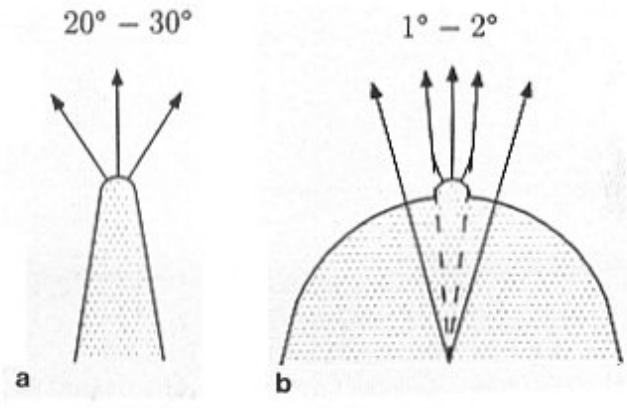

Figure 7.4: Effect of the shape of the apex of a tip on emission angle, reproduced from [51]. A single-atom tip built on a blunt apex will be forward focused compared to a tip with a higher aspect-ratio.

up to 1.2 nA. Other groups have reported stable field emission from tungsten nanotips at 20 nA of emission current [93], but the coherence of such a high-current beam has not been reported. It is likely that at such high currents, sources emit from a larger cluster of atoms than at low currents. This might increase the emission area and limit the coherence of the beam.

Research discussed in this work indicates that tips with a very low FIM onset voltage have a higher coherence angle than sources reported in the literature, which are nanotips built-up on a blunt shoulder. This implies that a tip with a high aspect-ratio will have a larger emission angle than a blunt tip. This makes intuitive sense, since the trajectories normal to the equipotential surface of the tip will diverge more for a sharp tip than a blunt one, as illustrated in Figure 7.4. However, for a given voltage and tip-sample separation, the field around a blunt tip is lower than for a sharp tip. By tailoring the aspect ratio of the tip by etching at a higher voltage, a broader tip can be manufactured, as described in Chapter 3.1. The relationship of etching voltage and hence aspect-ratio, to the coherence angle is a matter for further investigation. Experiments are planned to prepare a number of tips in a controlled manner to probe this relationship. Hopefully, there exists a 'sweet spot', where the aspect-ratio of the tip is sharp enough for a wide-enough coherence angle, but blunt enough so as to maintain a lower field for small tip-sample distances and hence a lower emission current.

Also, imaging in this apparatus has been done solely with sources using the (100) orientation of tungsten. A great deal of research indicates that the (111) orientation of tungsten presents a more controllable substrate for etching and produces a more stable tip with greater repeatibility [39, 42, 43, 44].

There are a few experimental challenges associated with using (111)-oriented wire. The wire itself is only available as a single crystal wire, which is incredibly soft and impossible to load in the HV-holder or scanning head, without drastically bending the wire. Efforts are underway to spot-weld a short section of W(111) wire to the robust, polycrystalline W(100) wire more commonly used in the microscope. These hybrid tips will combine the mechanical rigidity of the polycrystalline wire with the benefits of the soft and expensive W(111). This opens up an avenue for exploration of the relationship between etching parameters and coherence angle for W(111) in addition to W(100), widening the parameter space even further.

7.2 Nanoscale samples deposited on graphene

Holographic reconstructions remain a challenge. The main reason is the nature of the samples themselves; because nano-scale edges and filaments distort the electric field around them so much, the electron wave near the object is similarly distorted. The hologram ends up as a convolution of the local electric field near the object and the structure of the object itself, rendering reconstruction very difficult. Preliminary reconstructions are shown

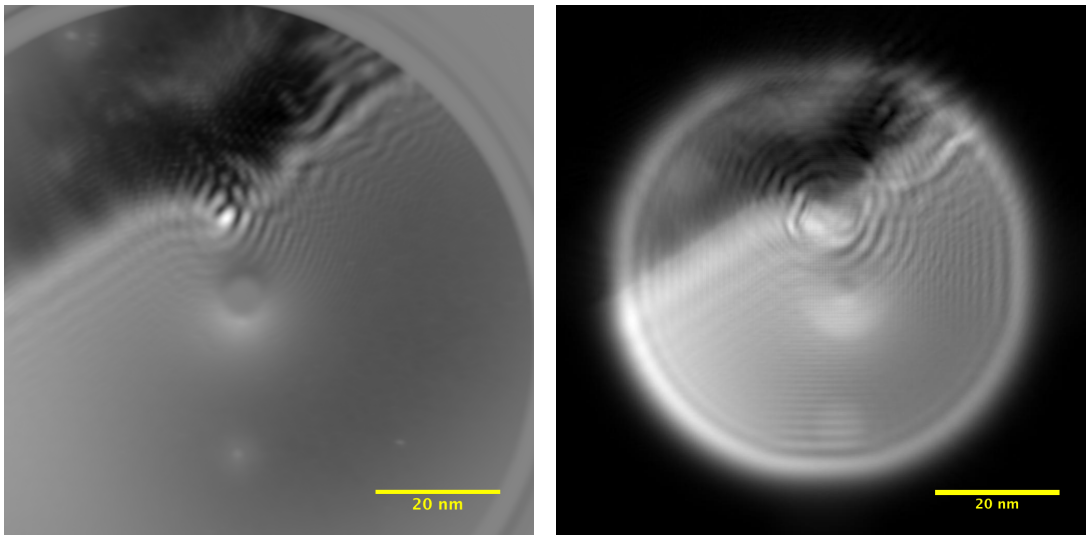

(a) A LEEPS hologram of an edge.

(b) The reconstructed image.

Figure 7.5: A preliminary holographic reconstruction of the edge, using software designed by Dr. Lucian Livadaru [62, 11]. There are features that are sharper in the reconstruction, but there are concentric rings confined to the centre of the image, thought to be due to the high field around a sharp feature in the edge.

in Figures 7.5 and 7.6.

There are two avenues for addressing this challenge. The first is to simulate the field around the object and use this as a parameter in the reconstruction algorithms. This technique has been used successfully in the past by Morin and colleagues [55, 56, 57, 58]

Experimentally, the effect of this field can be removed by mounting the samples on graphene, which serves as a grounded plane, straightening out equipotential surfaces near the sample and removing the distortion of the electron trajectories. Suspending a sample on graphene while avoiding contamination has been difficult. The graphene itself is contaminated with polymers and solvent from the growth and transfer. The samples themselves are similarly contaminated by surfactants or capping ligands. A cleaning procedure rigorous enough to remove contamination, while gentle enough to preserve the samples must be explored.

7.3 Helium-ion holography

Instead of using electron to generate the hologram it is possible to use helium ions, without any modification to the microscope itself. This experiment would be very close to that of FIM. With the tip brought very close to the sample, a high *positive* bias would be applied relative to the grounded sample while a background pressure of helium is leaked into the main chamber. The high-field near the tip would cause helium atoms to be ionized and accelerated through the sample, towards the MCP. Higher fields would be required to ionize helium ions, than to field-emit electrons from the tip. This would allow for closer tip-sample

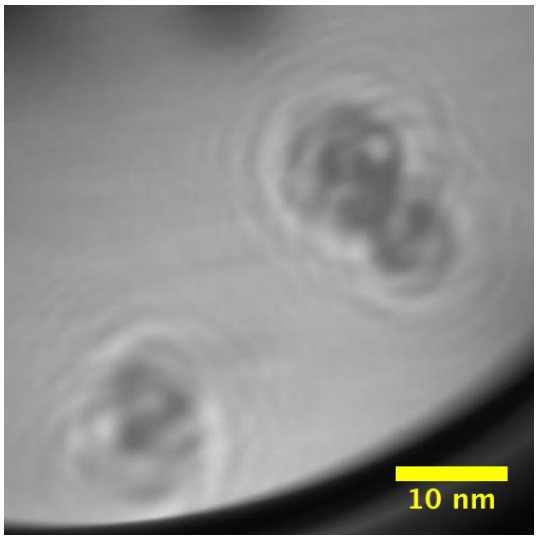

(a) A LEEPS hologram of defects in a graphene sheet.

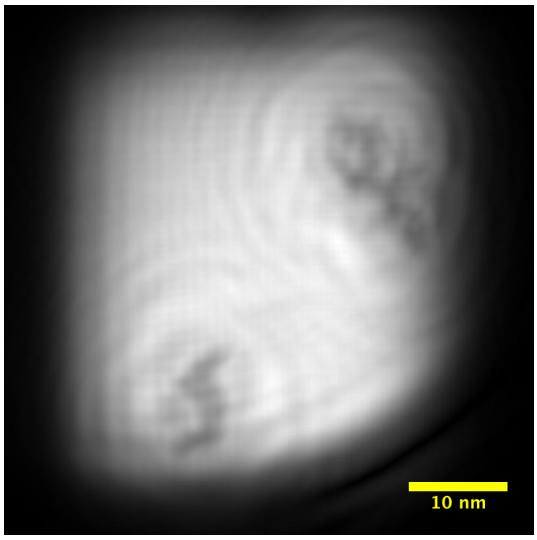

(b) The reconstructed image. The features are sharper than the hologram.

Figure 7.6: A preliminary holographic reconstruction of defects in a graphene sheet, using software designed by Dr. Lucian Livadaru [62, 11]. Image taken at 124 eV, 200 nm tip-sample distance.

distances and higher voltages than in LEEPS. Also, since the mass of a helium ion is some 7300 times greater than the mass of an electron. The de Broglie wavelength (equation 1.8) scales inversely with the square root of the particle mass. This means the wavelength of a helium ions would be nearly two orders of magnitude shorter. This would have a drastic impact on the resolution of the instrument.

A great deal of effort has been directed towards etching the tungsten tip as a source of helium ions, and a wealth of information is known on the impact of etching parameters on emission angle and stability of such tips [39, 42, 43, 44]. However, some experimental difficulties remain: single-atom tips are only stable as ion sources at LN_2 temperatures and there is no facility for cooling tips in the scanning head as is. But, the experiment can be attempted at room temperature with a larger radius of curvature tip. The gains in resolution afforded by having a wavelength two orders of magnitude smaller than with electrons may easily offset any thermal instabilities in the tip.

7.4 Outlook

Science has always been driven in part by the development of new microscopes. Despite the variety of techniques for studying matter at the nano-scale, there is always room for a simple and elegant approach. The birth of microbiology was driven, not by the most complex or technologically advanced compound microscopes of the day, but by the simplest single-lens microscope made by van Leeuwenhoek. In the case of modern electron microscopy, the field is crowded with high-energy techniques and sophisticated aberration correction

schemes. While these techniques have been refined over decades to achieve atomic resolution and many modes of imaging contrast, they still have many of the drawbacks they had in the 1930s: electron lenses still induce aberrations limiting the information contained in micrographs [94] and beam energies are so high they limit the samples that can be investigated.

This is the reason for revisiting LEEPS holography. Although the field has been well trod over during the intervening decades and the greatest advances in holography have been outside the realm of electron microscopy. There remain promising reasons to explore LEEPS at the nanoscale. Because all the phase information of the electron wave is preserved, a wealth of data about structure and local electromagnetic fields is available in LEEPS; most of this information is lost in competing techniques.

Using several measures extrapolated from the properties of interference patterns, this work has shown that after more than 60 years, LEEPS holography can be improved and taken to sub-nanometre resolutions. A new microscope has been built using new techniques to craft field emission sources with ideal properties and by carefully isolating the microscope. The microscope described in this work has been benchmarked to show unparalleled mechanical stability for such an instrument. Ultimately, by several crucial figures of merit, accepted by the microscopy community, the microscope far exceeds any previous apparatus.

Continued refinements in source and sample preparation are necessary. Also, as more holograms are produced, experience will lead to reconstructions with sub-nanometer resolution. Improvements in the geometry and source structure has the potential to push the technique to the atom-scale.

Over the last 60 years, the field of holography has been alternately filled with promise and disappointment. The road is littered with the derelict hulks of false starts and tantalizing visions. Now, by carefully tuning each parameter, by bleeding away mechanical vibration, by quieting the electromagnetic noise around the system and by crafting the source at the atom scale, the future looks very bright for this elusive, but elegant technique.

Bibliography

[1] W.J. Croft. *Under the microscope: a brief history of microscopy*, volume 5. World Scientific Pub Co Inc, 2006.

[2] J. Repp, G. Meyer, S.M. Stojković, A. Gourdon, and C. Joachim. Molecules on insulating films: Scanning-tunneling microscopy imaging of individual molecular orbitals. *Physical Review Letters*, 94(2):26803, 2005.

[3] JY Mutus, L. Livadaru, JT Robinson, R. Urban, MH Salomons, M. Cloutier, and RA Wolkow. Low-energy electron point projection microscopy of suspended graphene, the ultimate'microscope slide'. *New Journal of Physics*, 13:063011, 2011.

[4] RF Egerton, P. Li, and M. Malac. Radiation damage in the TEM and SEM. *Micron*, 35(6):399–409, 2004.

[5] W. Jiang, M. L. Baker, J. Jakana, P.R. Weigele, J. King, and W. Chiu. Backbone structure of the infections e15 virus capsid revealed by electron cryomicroscopy. *Nature*, 451:1130–1134, 2008.

[6] M. Pfeifer, G.J. Williams, I.A. Vartanyants, R. Harder, and I.K. Robinson. Three-dimensional mapping of a deformation field inside a nanocrystal. *Nature*, 442:63–66, 2006.

[7] S. Johnston. *Holographic visions: A history of new science*. Oxford University Press, USA, 2006.

[8] D. Gabor. A new microscopic principle. *Nature*, 161(4098):777–778, 1948.

[9] L. Livadaru, J. Mutus, and R.A. Wolkow. In-line holographic electron microscopy in the presence of external magnetic fields. *Ultramicroscopy*, 108(5):472–480, 2008.

[10] L. Livadaru, J. Mutus, and R.A. Wolkow. Limits of elemental contrast by low energy electron point source holography. *Journal of Applied Physics*, 110:094305, 2011.

[11] L. Livadaru, J. Mutus, and R.A. Wolkow. Point-source holographic imaging of nanostructures and interfaces with low energy electrons. In *Journal of Physics: Conference Series*, volume 126, page 012017. IOP Publishing, 2008.

[12] ME Haine and T. Mulvey. The formation of the diffraction image with electrons in the gabor diffraction microscope. *JOSA*, 42(10):763–769, 1952.

[13] A. Gölzhäuser, B. Völkel, M. Grunze, and HJ Kreuzer. Optimization of the low energy electron point source microscope: imaging of macromolecules. *Micron*, 33(3):241–255, 2002.

[14] U. Weierstall, JCH Spence, M. Stevens, and KH Downing. Point-projection electron imaging of tobacco mosaic virus at 40 ev electron energy. *Micron*, 30(4):335–338, 1999.

[15] GB Stevens. Resolving power of lens-less low energy electron point source microscopy. *Journal of Microscopy*, 235(1):9–24, 2009.

[16] JCH Spence, W. Qian, and MP Silverman. Electron source brightness and degeneracy from Fresnel fringes in field emission point projection microscopy. *Journal of Vacuum Science & Technology A: Vacuum, Surfaces, and Films*, 12(2):542–547, 1994.

[17] A. Tonomura. Applications of electron holography. *Reviews of modern physics*, 59(3):639, 1987.

[18] Gamma Vacuum. Titan 800LX.

[19] Agilent Technologies. Turbo-V 551 Navigator.

[20] Attocube Systems AG. ANPx101, ANPz101.

[21] S. Park and CF Quate. Theories of the feedback and vibration isolation systems for the scanning tunneling microscope. *Review of scientific instruments*, 58(11):2004–2009, 1987.

[22] E.I. Rivin. *Passive vibration isolation*. Amer Society of Mechanical, 2003.

[23] Q. Sun, R.A. Wolkow, and M. Salomons. Low frequency vibration isolation through an active-on-active approach: Coupling effects. *Journal of Vibration and Acoustics*, 131:061010, 2009.

[24] S.B. Chikkamaranahalli, R.R. Vallance, B.N. Damazo, and R.M. Silver. Damping mechanisms for precision applications in uhv environment.

[25] Technical Manufacturing Corporation. STACIS 2100.

[26] Dr. Peter G. Nelson. Supporting active electro-pneumatic vibration isolation systems on platforms supported by stacis hard-mount piezoelectric isolation systems. *Technical Manufacturing Applications notes*, 2002.

[27] JA Miwa, JM MacLeod, A. Moffat, and AB McLean. Rattling modes and the intrinsic vibrational spectrum of beetle-type scanning tunneling microscopes. *Ultramicroscopy*, 98(1):43–49, 2003.

[28] C.E.D. Chidsey, D.N. Loiacono, T. Sleator, and S. Nakahara. Stm study of the surface morphology of gold on mica. *Surface Science*, 200(1):45–66, 1988.

[29] C.C. Chang, H.S. Kuo, I.S. Hwang, and T.T. Tsong. A fully coherent electron beam from a noble-metal covered W (111) single-atom emitter. *Nanotechnology*, 20:115401, 2009.

[30] Spence J.C.H. and Cowley J.M. *Electron Holography at Low Energy, in Introduction to Electron Holography, Völkl, E. and Allard, L.F. and Joy, D.C., Eds.* Plenum Pub Corp, 1999.

[31] B. Cho, T. Ichimura, R. Shimizu, and C. Oshima. Quantitative evaluation of spatial coherence of the electron beam from low temperature field emitters. *Physical Review Letters*, 92(24):246103, 2004.

[32] H.W. Fink. Point source for ions and electrons. *Physica Scripta*, 38:260, 1988.

[33] H.W. Fink. Mono-atomic tips for scanning tunneling microscopy. *IBM journal of research and development*, 30(5):460–465, 1986.

[34] V.T. Binh and N. Garcia. On the electron and metallic ion emission from nanotips fabricated by field-surface-melting technique: experiments on w and au tips. *Ultramicroscopy*, 42:80–90, 1992.

[35] E. Rokuta, T. Itagaki, T. Ishikawa, B.L. Cho, H.S. Kuo, TT Tsong, and C. Oshima. Single-atom coherent field electron emitters for practical application to electron microscopy: Buildup controllability, self-repairing function and demountable characteristic. *Applied surface science*, 252(10):3686–3691, 2006.

[36] T.Y. Fu, L.C. Cheng, C.H. Nien, and T.T. Tsong. Method of creating a pd-covered single-atom sharp w pyramidal tip: Mechanism and energetics of its formation. *Physical Review B*, 64(11):113401, 2001.

[37] H.S. Kuo, I.S. Hwang, T.Y. Fu, J.Y. Wu, C.C. Chang, and T.T. Tsong. Preparation and characterization of single-atom tips. *nano letters*, 4(12):2379–2382, 2004.

[38] M. Rezeq, J. Pitters, and R. Wolkow. Tungsten nanotip fabrication by spatially controlled field-assisted reaction with nitrogen. *The Journal of chemical physics*, 124:204716, 2006.

[39] R Urban, J Pitters, and R.A. Wolkow. Tip apex shaping of gas field ion sources. Effect of overall tip shape on the operating tip voltage and possible forward focusing, 2011.

[40] E.W. Müller. Das feldionenmikroskop. *Zeitschrift für Physik A Hadrons and Nuclei*, 131(1):136–142, 1951.

[41] E.W. Müller and K. Bahadur. Field ionization of gases at a metal surface and the resolution of the field ion microscope. *Physical Review*, 102(3):624, 1956.

[42] R Urban, J Pitters, and R.A. Wolkow. Ion current stability of trimer and a single atom w(111) tips. A study of He and Ne imaging of trimer-capped and single atom tips, 2011.

[43] R Urban, J Pitters, and R.A. Wolkow. Single atom gas field ions source creation and recovery using w(111). On the repeatability of single atom tip fabrication, failure and recovery, 2011.

[44] R Urban, J Pitters, and R.A. Wolkow. Tungsten tip shape evaluation using ne imaging gas. Discusses tip shape and etching mechanism using Ne imaging gas., 2011.

[45] JP Ibe, PP Bey, SL Brandow, RA Brizzolara, NA Burnham, DP DiLella, KP Lee, CRK Marrian, and RJ Colton. On the electrochemical etching of tips for scanning tunneling microscopy. *Journal of Vacuum Science & Technology A: Vacuum, Surfaces, and Films*, 8(4):3570–3575, 1990.

[46] Structure Probes Inc. P/N 4108PSN-BA.

[47] V.T. Binh, V. Semet, and N. Garcia. Nanometric observations at low energy by fresnel projection microscopy: carbon and polymer fibres. *Ultramicroscopy*, 58(3-4):307–317, 1995.

[48] R McLeod. Fresneldiff.m. MATLAB simulation of fresnel diffraction pattern, 2011.

[49] Q. Sun and R.A. Wolkow. Three-dimensional displacement analysis of a piezoelectric tube scanner through finite element simulations of a tube assembly. *Review of scientific instruments*, 77:113701, 2006.

[50] MR Scheinfein, W. Qian, and JCH Spence. Aberrations of emission cathodes: Nanometer diameter field-emission electron sources. *Journal of applied physics*, 73(5):2057–2068, 1993.

[51] F. Hasselbach. Selected topics in charged particle interferometry. *Scanning Microscopy*, 11:345–366, 1997.

[52] ST Purcell, V.T. Binh, and N. Garcia. 64 mev measured energy dispersion from cold field emission nanotips. *Applied physics letters*, 67:436, 1995.

[53] S. Iijima. Helical microtubules of graphitic carbon. *Nature*, 354(6348):56–58, 1991.

[54] M.C. Hersam. Progress towards monodisperse single-walled carbon nanotubes. *Nature Nanotechnology*, 3(7):387–394, 2008.

[55] M. Prigent and P. Morin. Charge effect in point projection images of Ni nanowires and I collagen fibres. *Journal of Physics D: Applied Physics*, 34:1167, 2001.

[56] M. Prigent and P. Morin. Charge effect in point projection images of carbon fibres. *Journal of microscopy*, 199(3):197–207, 2000.

[57] V. Georges, J. Bardon, A. Degiovanni, and R. Morin. Imaging charged objects using low-energy-electron coherent beams. *Ultramicroscopy*, 90(1):33–38, 2001.

[58] P. Morin, M. Pitaval, and E. Vicario. Low energy off-axis holography in electron microscopy. *Physical Review Letters*, 76(21):3979–3982, 1996.

[59] H. Lichte. Gottfried möllenstedt and his electron biprism: four decades of challenging and exciting electron physics. *Journal of electron microscopy*, 47(5):387, 1998.

[60] H. Lichte and M. Lehmann. Electron holographybasics and applications. *Reports on Progress in Physics*, 71:016102, 2008.

[61] F. Hasselbach. Progress in electron-and ion-interferometry. *Reports on Progress in Physics*, 73:016101, 2010.

[62] J Y Mutus, L Livadaru, and Wolkow R A. High coherence angle of tips produced by field assisted etch. Work relating to the aspect ratio of tip and coherence width of the pattern, 2012.

[63] H. Liebl. *Applied charged particle optics*. Springer Verlag, 2007.

[64] R.F. Egerton. *Physical principles of electron microscopy: an introduction to TEM, SEM, and AEM*. Springer, 2005.

[65] PR Wallace. The band theory of graphite. *Physical Review*, 71(9):622, 1947.

[66] A.K. Geim and K.S. Novoselov. The rise of graphene. *Nature materials*, 6(3):183–191, 2007.

[67] KS Novoselov, AK Geim, SV Morozov, D. Jiang, Y. Zhang, SV Dubonos, IV Grigorieva, and AA Firsov. Electric field effect in atomically thin carbon films. *Science*, 306(5696):666, 2004.

[68] Z. Lee, K.J. Jeon, A. Dato, R. Erni, T.J. Richardson, M. Frenklach, and V. Radmilovic. Direct Imaging of Soft- Hard Interfaces Enabled by Graphene. *Nano letters*, 9(9):3365–3369, 2009.

[69] W.H. Dobelle and M. Beer. Chemically cleaved graphite support films for electron microscopy. *The Journal of Cell Biology*, 39(3):733, 1968.

[70] S. Iijima. Observation of single and clusters of atoms in bright field electron microscopy. *Optik*, 48(2):193–214, 1977.

[71] Y.M. Lin, K.A. Jenkins, A. Valdes-Garcia, J.P. Small, D.B. Farmer, and P. Avouris. Operation of graphene transistors at gigahertz frequencies. *Nano Letters*, 9(1):422–426, 2008.

[72] F. Xia, T. Mueller, R. Golizadeh-Mojarad, M. Freitag, Y. Lin, J. Tsang, V. Perebeinos, and P. Avouris. Photocurrent imaging and efficient photon detection in a graphene transistor. *Nano letters*, 9(3):1039–1044, 2009.

[73] Xuesong Li, Weiwei Cai, Jinho An, Seyoung Kim, Junghyo Nah, Dongxing Yang, Richard Piner, Aruna Velamakanni, Inhwa Jung, Emanuel Tutuc, Sanjay K. Banerjee, Luigi Colombo, and Rodney S. Ruoff. Large-Area Synthesis of High-Quality and Uniform Graphene Films on Copper Foils. *Science*, 324(5932):1312–1314, 2009.

[74] Xuesong Li, Yanwu Zhu, Weiwei Cai, Mark Borysiak, Boyang Han, David Chen, Richard D. Piner, Luigi Colombo, and Rodney S. Ruoff. Transfer of large-area graphene films for high-performance transparent conductive electrodes. *Nano Letters*, 9(12):4359–4363, 2009. PMID: 19845330.

[75] K.S. Kim, Y. Zhao, H. Jang, S.Y. Lee, J.M. Kim, K.S. Kim, J.H. Ahn, P. Kim, J.Y. Choi, and B.H. Hong. Large-scale pattern growth of graphene films for stretchable transparent electrodes. *Nature*, 457(7230):706–710, 2009.

[76] P.Y. Huang, C.S. Ruiz-Vargas, A.M. van der Zande, W.S. Whitney, M.P. Levendorf, J.W. Kevek, S. Garg, J.S. Alden, C.J. Hustedt, Y. Zhu, et al. Grains and grain boundaries in single-layer graphene atomic patchwork quilts. *Nature*, 2011.

[77] W. Regan, N. Alem, B. Aleman, B. Geng, C. Girit, L. Maserati, F. Wang, M. Crommie, and A. Zettl. A direct transfer of layer-area graphene. *Applied Physics Letters*, 96(11):113102–113102, 2010.

[78] JC Meyer, AK Geim, MI Katsnelson, KS Novoselov, D. Obergfell, S. Roth, C. Girit, and A. Zettl. On the roughness of single-and bi-layer graphene membranes. *Solid State Communications*, 143(1-2):101–109, 2007.

[79] J.C. Meyer, AK Geim, MI Katsnelson, KS Novoselov, TJ Booth, and S. Roth. The structure of suspended graphene sheets. *Nature*, 446(7131):60–63, 2007.

[80] U. Bangert, MH Gass, AL Bleloch, RR Nair, and AK Geim. Manifestation of ripples in free-standing graphene in lattice images obtained in an aberration-corrected scanning transmission electron microscope. *physica status solidi (a)*, 206(6):1117–1122, 2009.

[81] A. Fasolino, JH Los, and MI Katsnelson. Intrinsic ripples in graphene. *Nature Materials*, 6(11):858–861, 2007.

[82] VB Shenoy, CD Reddy, A. Ramasubramaniam, and YW Zhang. Edge-stress-induced warping of graphene sheets and nanoribbons. *Physical Review Letters*, 101(24):245501, 2008.

[83] W. Bao, F. Miao, Z. Chen, H. Zhang, W. Jang, C. Dames, and C.N. Lau. Controlled ripple texturing of suspended graphene and ultrathin graphite membranes. *Nature Nanotechnology*, 4(9):562–566, 2009.

[84] R.C. Thompson-Flagg, M.J.B. Moura, and M. Marder. Rippling of graphene. *EPL (Europhysics Letters)*, 85:46002, 2009.

[85] A. Jablonski, F. Salvat, and CJ Powell. NIST Electron Elastic-Scattering Cross-Section Database–Version 3.1. *National Institute of Standards and Technology, Gaithersburg MD). http://www. nist. gov/srd/nist64. htm*, 2003.

[86] John R. Vig. Uv/ozone cleaning of surfaces. *Journal of Vacuum Science Technology A: Vacuum, Surfaces, and Films*, 3(3):1027 –1034, May 1985.

[87] R.A. Barton, B. Ilic, A.M. Van Der Zande, W.S. Whitney, P.L. McEuen, J.M. Parpia, and H.G. Craighead. High, size-dependent quality factor in an array of graphene mechanical resonators. *Nano letters*, 2011.

[88] C.O. Girit, J.C. Meyer, R. Erni, M.D. Rossell, C. Kisielowski, L. Yang, C.H. Park, MF Crommie, M.L. Cohen, S.G. Louie, et al. Graphene at the Edge: Stability and Dynamics. *Science*, 323(5922):1705, 2009.

[89] PCO AG. Pixelfly.

[90] I.S. Hwang, H.S. Kuo, C.C. Chang, and T.T. Tsong. Noble-metal covered w (111) single-atom electron sources. *Journal of the Electrochemical Society*, 157:P7, 2010.

[91] A. Gölzhäuser, B. Völkel, B. Jäger, M. Zharnikov, HJ Kreuzer, and M. Grunze. Holographic imaging of macromolecules. *Journal of Vacuum Science & Technology A: Vacuum, Surfaces, and Films*, 16:3025, 1998.

[92] R.H. Fowler and LW Nordheim. Electron emission in intense electric fields. *Proceedings of the Royal Society of London. Series A, Containing Papers of a Mathematical and Physical Character*, 119(781):173–181, 1928.

[93] T. Ishikawa, T. Urata, B. Cho, E. Rokuta, C. Oshima, Y. Terui, H. Saito, A. Yonezawa, and T.T. Tsong. Highly efficient electron gun with a single-atom electron source. *Applied physics letters*, 90:143120, 2007.

[94] D. Geiger, H. Lichte, M. Linck, and M. Lehmann. Electron holography with a cs-corrected transmission electron microscope. *Microscopy and Microanalysis*, 14(01):68–81, 2008.